

Green Fluorescent Protein as a Mechanical Sensor

by

Taro M. Muso

Sc.B. Engineering
Brown University

SUBMITTED TO THE DIVISION OF HEALTH SCIENCES AND TECHNOLOGY IN
PARTIAL FULFILLMENT OF THE REQUIREMENTS FOR THE DEGREE OF

MASTER OF SCIENCE IN HEALTH SCIENCES AND TECHNOLOGY
AT THE
MASSACHUSETTS INSTITUTE OF TECHNOLOGY

FEBRUARY 2007

[June 2007]

©2007 Taro M. Muso. All rights reserved.

The author hereby grants to Harvard University and MIT permission to reproduce
and to distribute publicly paper and electronic copies of this thesis document
in whole or in part in any medium now known or hereafter created.

Signature of Author: _____

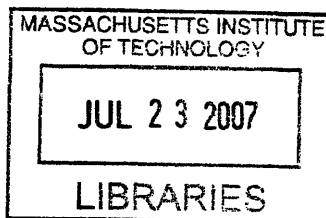
Harvard-MIT Division of Health Sciences and Technology
February 5, 2007

Certified by: _____

Paul Matsudaira, Ph.D.
Professor of Biology and Biological Engineering
Member, Whitehead Institute for Biomedical Research
Thesis Supervisor

Accepted by: _____

Martha L. Gray, Ph.D.
Edward Hood Taplin Professor of Medical and Electrical Engineering
Director, Harvard-MIT Division of Health Sciences and Technology



ARCHIVES

Green Fluorescent Protein as a Mechanical Sensor

by

Taro M. Muso

Submitted to the Harvard-MIT Division of Health Sciences and Technology on February 5, 2007 in Partial Fulfillment of the Requirements for the Degree of Master of Science in Health Sciences and Technology

ABSTRACT

Inquiry into intracellular and cytoskeletal mechanics requires an intracellular mechanical sensor to verify models of sub-cellular structure dynamics. To this end, the green fluorescent protein (GFP) is considered as a mechanical sensor candidate with many desirable characteristics. Implicit solvent molecular dynamics CHARMM simulations demonstrated details inaccessible by AFM and OT methods, such as the linkage dependency of fluorophore environment changes and the energy exchanges between protein components during protein unfolding. Theoretical considerations and *in vitro* experiments explored the parameters important to GFP conjugation by *N*-hydroxysuccinimide (NHS) ester chemistry, and the complexities associated with a polymer approach to a controlled distribution of force across fluorescent proteins in a polyacrylamide (PAM) gel.

Thesis Supervisor: Paul Matsudaira

Title: Professor of Biology and Biological Engineering; Member, Whitehead Institute for Biomedical Research

Acknowledgements

I'd like to thank Paul Matsudaira for his financial support and the meetings where I learned from his ideas and wisdom. I would like to thank the members of the lab for their support. Yelena Freyzon helped me with GFP synthesis and purification. Kazuyoshi Murata and Sangjin Ryu were two colleagues with whom I had the privilege of having numerous conversations. Muhammad Zaman introduced me to the power of molecular dynamics simulations.

Eric Spooner, a member of the Ploegh lab, gave me access to his group's mass spectrometer. His technical expertise enabled me to access reliable data at a fraction of the time I would have otherwise spent. However, it is probably his congeniality, and his willingness to help me where he could, that make him stand out in my memories.

The infrastructure at the Whitehead Institute is by far the best of any research facility that I've worked in so far (n=5). The security staff were professional and personable. The safety staff managed to maintain a high degree of compliance in spite of the research staff (myself included). Any mysterious odors, alarms, or water leaks were addressed rapidly by the facilities staff. The cafeteria staff made delicious meals.

Of course, none of this would have been possible without financial support from the Whitehead family, the parties whose names appear on the wall of donors, and the American taxpayer. They, especially the ones whose itemized deductions nullified the tax-deducting effect of their donations, are the unsung heroes of this unfolding story of biomedical research.

Finally, I deeply appreciate the caring and support of family, friends, colleagues, and professors. Guang William Wong, Graham Ruby, Ramya Rajagopalan, Maya Barley, and Eric Spooner were some of the people who helped me even when this entailed having discussions with me that were outside of their job descriptions. I had memorable lunches with Catherine McLellan, Lori Schoenfeld, Harvey Lodish, Naomi, Stephanie, and Mike Xiang.

Thank you.

Table of Contents

GREEN FLUORESCENT PROTEIN AS A MECHANICAL SENSOR.....	1
ABSTRACT	3
ACKNOWLEDGEMENTS.....	5
TABLE OF CONTENTS.....	6
LIST OF FIGURES	8
LIST OF TABLES	12
LIST OF EQUATIONS	14
CHAPTER 1. INTRODUCTION	15
MECHANOTRANSDUCTION	15
MEASUREMENT OF INTRACELLULAR MECHANICS.....	21
GREEN FLUORESCENT PROTEIN	23
GFP PHOTOPHYSICS	24
CONFIGURING GFP	28
EXPLORING CONFIGURATIONAL BENEFITS.....	33
SUMMARY	43
CHAPTER 2. DYNAMIC STABILITY, FORCE AND ENERGY.....	45
THERMAL ENERGY AND FORCE ADJUSTED KINETICS.....	45
RELIABILITY THEORY	47
VELOCITY-CLAMP METHOD.....	50
FORCE-CLAMP METHOD.....	54
DETAILS OF GFP THAT AFFECT MECHANICAL AND OPTICAL RESPONSE.....	56
COMPUTATIONAL CHEMISTRY	60

RESULTS AND DISCUSSION.....	69
SUMMARY	79
METHODS.....	80
CHAPTER 3. THE APPLICATION OF SHEAR FORCES ON GFP.....	81
BACKGROUND.....	81
EXPERIMENT OBJECTIVES	104
RESULTS.....	104
DISCUSSION.....	111
SUMMARY	124
METHODS.....	125
CHAPTER 4. CONCLUSION	129
REFERENCES.....	133

List of Figures

Figure 1. Mediators of Mechanotransduction. Many parts in the mammalian cell are involved in mechanosensation (Ingber, 2006). The cell-ECM area contains focal adhesions, within which integrins play a key role in binding to RGD peptide sequences in the extracellular matrix (ECM). The ECM, which is often the basement membrane, contains proteoglycans, collagen, and fibronectin. Fibronectin has cryptic sites that allegedly become accessible upon stretch. These stretches also affect cell-cell adhesions, such as cadherins and gap junctions on the lateral surface of the membrane. On the apical membrane surface are surface processes, such as primary cilium and stereocilia, that dwarf the surface receptors, the transmembrane ion channels, and the caveolae on the cytoplasmic side. Within the cytoplasm cytoskeletal elements, such as microfilaments, microtubules, and intermediate filaments, can convey mechanical effects from the surface to interior structures. One major structure is the nucleus, which has its own ion channels in the nuclear lamina. Finally, inside the nucleus genetic material uncoils into chromatin during gene expression; this unwinding process itself has mechanical considerations unexplained by chemical means alone.

Figure 2. Force transmission in skin. Adapted from (Silver et al., 2003b) Mechanical distribution occurs in terms of all levels. At the tissue level, the basement membrane and collagen fibrils are transporting messages. At the molecular level, fibroblasts respond to continual change in force through the $\alpha5\beta1$ integrins (Silver et al., 2003b). Incidentally, the vertebrate hair cell mechanotransduction apparatus has striking similarities with that of *Drosophila*; mechanosensory systems are conserved from vertebrates to invertebrates (Gillespie and Walker, 2001).

Figure 3. GFP Fluorescence spectra. Adapted from (Kummer et al., 1998)

Figure 4. GFP state pathways. This diagram is the combined result of papers referenced above.

Figure 5. Estimation of contributions of each GFP state to the overall absorbance spectrum. Adapted from (Wiehler et al., 2003)

Figure 6. Photoconversion. Ultraviolet irradiation can induce GFP to undergo photoconversion, in which a carbon dioxide molecule is removed from *glu222*.

Figure 7. GFP relaxation mechanisms. (a) The GFP fluorophore's radiative relaxation pathways must compete with the alternative, non-radiative mechanisms. (b) A key non-radiative relaxation mechanism is the hula twist method.

Figure 8. Viable positions on the GFP for engineering a fusion protein.

Figure 9. Schematic of linking elements. (a) Non-specific binding will link glass surface and antibody. (b) The anti-hemagglutinin antibody will attach to the HA moiety fused into a loop of the GFP. (c) The linking reagent SATP will be used to make a sulfhydryl group on the N-terminal amine on GFP, followed by deprotection and linkage with the 5'-thiol on the DNA tether. SATP must not be allowed to modify the antibody's N-termini, nor any of the lysine amino groups. Because of this complexity, the S-S bond formation may need to be made first. (d) 5'-biotin on the other end of the DNA tether will link to a streptavidin-coated bead.

Figure 10. Scaled schematic of configuration. C, S, and g are points: g, position of GFP; s, position where tether and sphere attach together; c, center of bead. The variables f, t1, t2, and r are lengths: f, radius of measured fluorescence volume; r, radius of bead; t1, length of DNA tether; t2, length of tether 2 (which is essentially the antibody). Theta (θ) is the angle between the glass and taut tether construct.

Figure 11. Testing the DNA tether. Following a deprotection step, an oxidative environment that dimerizes the DNA tethers by means of disulfide bond formation should readily show its effect on a standard 1.5% agarose electrophoresis. Dimerization should give a major band at 3kbp and a minor band at 1.5kbp, while the untreated control should give one major band at 1.5kbp.

Figure 12. Two configurations for force sensing. (a) The structure on the left will completely unfold if one pulls the structure at the RGD peptide sequence. (b) The structure on the right is expected to unfold only part way, because the RGD peptide under tension would merely straighten the curves out of an already somewhat straight beta strand.

- Figure 13 Schematic for an intracellular force sensor. (a) The structure on the left represents a GFP with two binding domains. (b) The structure on the right represents a GFP with cys residues in place of the binding domains, for extracellular calibration of the sensor.
- Figure 14. Lennard-Jones potential function under applied load. The original, force-free potential (thin line) and the force-adjusted potential (thick line) become further and further apart. Incidentally, this implies that when a binding potential has multiple energy minima (as in a noncovalent, protein-protein bond), outer energy pockets are affected greater than inner energy pockets.
- Figure 15. Typical “sawtooth” profile from a velocity-clamp mechanical unfolding experiment. Each peak can be considered to correspond to an unfolding of a single domain. However, the upward movement of the force is due to the resistance of the entire chain. Hence the Worm-Like Chain model can be used to interpolate the behavior of the protein up to the rupture force, at which point the model breaks down for a set of parameters.
- Figure 16. Schematic of velocity-clamp experiment data: occurrence vs. force. For a given ramping rate, the rupture force measurements result in a distribution (Li et al., 2006). The fraction of molecules folded is determined by integrating over force. The average rupture force is the corresponding force for the folded fraction. Repeating this over a number of ramping rates would give a plot with which one can solve for $X \neq f \rightarrow u$ and $Af \rightarrow u$. (Li et al., 2006)
- Figure 17. The dynamic strength of mostly covalent and ionic bonds: peak rupture force [pN] vs. ramping rate [pN/s]. From the top, C-O; C-N(green) and C-C(black); Si-O; Si-N; Si-C; Si-Si; S-Au(one data point); DOPA; His6 Ni-NTA pH 7.2 (inside the box). The box represents approximate area covered in the noncovalent bond strength figure. Lines were derived from data of the following references: His6 Ni-NTA pH 7.2, (Kienberger et al., 2000); Si-C, S-Au, (Grandbois et al., 1999); C-C, C-N, C-O, Si-C, Si-N, Si-O, Si-Si (DFT), (Beyer, 2000); 3,4-dihydroxy-L-phenylalanine (dopa) (Lee et al., 2006).
- Figure 18. The dynamic strength of noncovalent bonds: peak rupture force [pN] vs. ramping rate [pN/s]. At a ramping rate of 10000 pN/s, histidine tags complexed with Ni-NTA prove to be strongest. Green, green-yellow, and orange represent the His tags at different pH values. In order of decreasing strength at 5E4 pN/s, they are: His6 Ni-NTA pH 7.5 (green), His6 Ni-NTA pH 7.2 (green-yellow), and His6 Ni-NTA pH 6.0 (orange). Red line indicates biotin-streptavidin (pH 7.2), activated $\alpha 5\beta 1$ integrin with plasma fibronectin is indicated by the kinked light blue line. The dark blue represents P-selectin. Non-NTA His tag bonds were weaker than those with NTA. The grey represents His6 Ni pH 7.5, and lowest line (gold) represents His6 Au pH 7.5. The purple dot represents CsA-CsA, a dimerization of the bacterial glycoprotein, contact site A. The noncovalent bonds are located within the previous figure within the area estimated by a box. Lines were derived from data of the following references: His6 Au pH 7.5, His6 Ni pH 7.5, His6 Ni-NTA pH 6.0, His6 Ni-NTA pH 7.5, (Schmidt et al., 2002); His6 Ni-NTA pH 7.2, (Kienberger et al., 2000); biotin-streptavidin pH 7.2, (Merkel et al., 1999); activated $\alpha 5\beta 1$ integrin with plasma fibronectin (Li et al., 2003); CsA-CsA (Benoit et al., 2000); P-selectin (Fritz et al., 1998).
- Figure 19. Extension-time curve from a force-clamp experiment.
- Figure 20. Simplified Jablonski diagram. Fluorescence is an excitation of a cold body by one photon, followed by an emission of another photon but at a longer wavelength. It is characterized by extinction coefficient, quantum yield, and fluorescence lifetime.
- Figure 21. GFP fluorophore model compound p-hydroxy benzilidene 1,2 dimethyl imidizolinone (HBDI). In GFP, most of the covalent structure would be from tyr66. The bottom left hydroxy group would form a hydrogen bond bridge to his148 via a single water molecule inside the beta-can. Indicated are the dihedral angles τ (N1-C1-C2-C3) and ϕ (C1-C2-C3-C4). Rotations about the τ and ϕ angles result in four different nonradiative relaxation paths: τ one-bond-flip; ϕ one-bond-flip; positively correlated hula-twist (+HT), where both angles rotate as shown above in the “same” direction; and negatively correlated hula-twist (-HT) where there is simultaneous rotations in opposing directions. Adapted from (Maddalo and Zimmer, 2005).
- Figure 22. Hinge and shear motions in protein mechanics. Adapted from (Gerstein et al., 1994).
- Figure 23. Schematic of force sensor. Mutagenesis and applied load trajectory affect the local hydrogen bond network of the fluorophore. Subtle changes in this noncovalent network alters absorption and emission properties. Nonradiative relaxation can involve solvent quenching and “hula twist” mechanisms.
- Figure 25. GFP structure schematic. An equilibrated conformation was positioned according to the major axes of the molecule. The xy-schematic (a) shows a view with the z-axis point out from the page. The

- xz-schematic shows a view with the y-axis pointing into the page. Gridlines were preserved at 5 Å intervals, since there is no concern for data interpretation bias.
- Figure 24. GFP hydrogen bond network schematic near Y66 and H148. This snapshot indicates the arrangement of three hydrogen bonds (yellow), which occur as a result of a bridging water molecule. Such networks are believed to stabilize the fluorophore against the non-radiative, “hula-twist” relaxation that decreases the quantum yield. The cylinder at the side indicates the orientation of the molecule.
- Figure 26. Comparison of force and solvent-accessible surface area for velocity-clamp simulations. Force and SASA were normalized against their respective maximum values within each simulation. (a) 10 Å/ps; (b) 1 Å/ps; (c) 0.1 Å/ps.
- Figure 27 Abrupt SASA changes for individual amino acids, SASA[A2] vs. extension [0.1Å]. The dummy atom was moved at a constant velocity of 10 Å/ps (50% gray) or 0.1 Å/ps (black): (a) asp133 is part of a flexible, 15-residue loop; (b) ala1, whose alpha carbon was connected to the constant-velocity pulling dummy “atom” in a harmonic potential, lost a hydrogen bond at about 15 Å of extension in the slow unfolding case; (c) val150, part of the beta-sheet structure, abruptly acquired solvation ~24 Å of extension.
- Figure 28. Hydrogen bond network dimensions as a function of unfolding extension. Unfolding extension was the distance between A001 and T230 [Å]. All distances were measured from the Y66 hydroxy oxygen. (N146) Distance to N146 carbonyl carbon. (H148) Distance to H148 backbone amine. (S205) Distance to S205 hydroxy oxygen.
- Figure 29. Total number of hydrogen bonds vs. A001-T230 extension length [Å].
- Figure 30. Percentage of preserved inter-beta strand hydrogen bond relationships vs. A001-T230 extension length [Å].
- Figure 31. Shear stress ($\sigma=F/A$) and shear strain ($\epsilon=\Delta x/\Delta y$). The block is deformed by force F , for every area A . The shear stress is $\sigma:=F/A$. The shear strain is $\epsilon:=\Delta x/\Delta y$.
- Figure 32. Schematic of $G(t)$ for a monodisperse linear polymer melt. The stress relaxation modulus $G(t)$ reaches a plateau modulus, which is independent of degree of polymerization. However, chain length *does* influence the termination time: $\tau T \sim N^{3.4}$.
- Figure 33. Reptation of a polymer chain. Entanglements along a chain restricts its motion along a virtual tube.
- Figure 34. Cayley tree of $z=3$. If the innermost circle’s node is considered the first generation, then the second generation is the set of nodes between the smallest and medium circles. Adjunct mathematical details may be helpful. Each node (except the first generation node) can give rise to $z-1$ branches. If bn is the number of branches (or nodes) in the n th generation, then $bn+1$ will have $bn(z-1)$ branches. In other words, $b1(z-1)n-1 = bn$. The total number of nodes to the n th generation is $Sn = b1 \sum_{i=1}^n (z-1)^{i-1}$. If f is the fraction of reacted bonds (each bond formation being independent of the others), then the total number of branches up to the n th generation is $Bn = b1 \sum_{i=1}^n [f(z-1)]^{i-1}$. If $f(z-1) \geq 1$, this geometric series will diverge, i.e. create an “infinite” cluster.
- Figure 35. Gel fraction as a function of reactivity and functionality. The functionality numbers $z = 3, 4, 6,$ and 50 are the potential number of bonds a node could make. The gel fraction P/f is the fraction of bonds that are connected to the infinite network.
- Figure 36. Node participation as a function of reactivity and functionality. The functionality numbers $z = 3, 4, 6,$ and 50 are the potential number of bonds a node could make. The fraction P is the probability that a given particle is part of the infinite network.
- Figure 37. Radical polymerization of acrylamide, chain reaction. The lone electron (\bullet) on the chain combines with an electron from the monomer to form a single bond between the two entities.
- Figure 38. EDC conjugation steps. A carboxylate-containing molecule (e.g. GFP) reacts with EDC to form an
- Figure 39. NHS-ester conjugation mechanism. The primary amines of lysines in GFP reacts with the imidoester to produce an amidine linkage.
- Figure 40. Schematic of the syringe experiment.
- Figure 41. Comparison of noise to signal average on the inverted microscope. Rising signal also increases the standard deviation.
- Figure 42. Comparison of CV% to signal average on the inverted microscope. The noise is consistent with the magnitude of the signal average.

Figure 43. Normalized fluorescence activity over time. Blue marks indicate GFP-acrylate-incorporated hydrogel, where RFU was expected to decrease. Red marks indicate GFP-incorporated hydrogel, where RFU was not expected to decrease. Substantial deterioration however, seems to occur.

Figure 44. Effects of polymerization time on fluorescence. Vertical orange lines indicate time of TEMED addition. Well sample's marker shape (e.g. triangle) corresponds to the orange marker at which point TEMED was added (e.g. orange triangle).

Figure 45. Effects of syringe-shearing on fluorescence.

Figure 46. Effects of linker chemistry on fluorescence activity.

Figure 47. Expected force-fluorescence curve. Black curve indicate initial expected average signal, dependent on the magnitude of constant force application. Gray and light gray curves represent experiments with varying degrees of photobleaching. The sensitivity of equilibrium to force near $K_{eq} = 1$ means that molecular force measurement requires sophistication beyond ideas of simple threshold values.

List of Tables

- Table 1. Protein domains considered for fusion with GFP. Domain abbreviations: ADF, Actin Depolymerizing Factor; APC, Adenomatous Polyposis Coli; CH, Calponin Homology; CTD, C-Terminal Domain; FH, Formin Homology; LIM, Lin-11 Isl-1 Mec-3; TBC, Tubulin Binding Cofactor; VHP, Villin Head Piece; WAS, Wiskott-Aldrich Syndrome; WASP, WAS Protein; WH, WASP Homology. Partner abbreviations: a, actin; fa, F-actin; fa(barbed), barbed end of microfilament; fa(end), the end of microfilament; ga, G-actin; mt+, microtubule plus end; t, tubulin; zn, zinc.
- Table 2. Hydrogen bonding partner-candidates for the fluorophore.
- Table 3. Characteristic distances within a fluorophore hydrogen bond network.
- Table 4. Beta strand details.
- Table 5. Experimental techniques for studying mechanical interactions with living cells.
- Table 6. Proteolytic enzymes for mass spectrometry. These enzymes are used in digests of proteins, to make pieces that the MS machine can handle with sufficient resolution.
- Table 7. Solvent accessibility of potential conjugation sites.
- Table 8. Signal data on an inverted fluorescence microscope.
- Table 9. Asp-N digest product candidates for AA-GFP. Mass spectrometer measurements of molecular weight (MH+) and expected digest mechanisms for Asp-N protease catalysis provided the following list of possible sequences. The sequence provides the peptide fragment location (PFL), the percent of macromolecular mass(%Mass), and the percent of GFP amino acid sequence (%GAA).
- Table 10. Trypsin cleavage product candidates for AA-GFP. Mass spectrometer measurements of molecular weight (MH+) and expected digest mechanisms for trypsin protease catalysis provided the following list of possible sequences. The sequence provides the peptide fragment location (PFL), the percent of macromolecular mass(%Mass), and the percent of GFP amino acid sequence (%GAA).
- Table 11. Chymotrypsin cleavage products for AA-GFP. Mass spectrometer measurements of molecular weight (MH+) and expected digest mechanisms for chymotrypsin protease catalysis provided the following list of possible sequences. The sequence provides the peptide fragment location (PFL), the percent of macromolecular mass(%Mass), and the percent of GFP amino acid sequence (%GAA).
- Table 12. Fluorescence activity in buffer solution removed from GFP-encapsulated hydrogels. Units are in Reference Fluorescence Units.
- Table 13. Raw RFU values for wells vs. time. Shearing by Hamilton syringe was done after t3 and before t4. TEMED introduction for column 3 (wells A3, B3, D3, E3) happened before shearing or measurement began. TEMED introduction for column 4 (wells A4, B4, D4, E4) occurred between t3 and t4.
- Table 14. Analysis of signal measurements from inverted microscope. Gray parts were included to match this table to its counterpart in the Results section. The CV% was calculated.
- Table 15. Polymerization time and fluorescence activity. Each pair of wells that are listed have the same conditions, except for the time at which TEMED was added to the well.
- Table 16. Shearing and fluorescence activity. Each pair of wells have the same conditions, except for the fact that the first of the pair had been subjected to shearing by a Hamilton syringe.
- Table 17. Acrylic acid linkage and fluorescence activity. Each pair of wells share the same conditions, except that only one of the two wells have GFP that were subjected to vinyl group additions by NHS chemistry.
- Table 18. Well compositions for the syring-shearing experiments. Asterisks indicate that pH was subsequently adjusted. For the column titled #17, a GFP solution of 9.6 μ L and an acrylic acid NHS ester solution of 287 μ L were mixed together in a prior preparatory step. #17b is essentially the experimental group. For the column marked #18, a GFP solution of 9.6 μ L was mixed with a 10X PBS solution of 287 μ L in a preparatory step. The acrylic acid NHS ester solution was made at 21 mg/mL in 10X PBS, where the pH was adjusted back to the range of 7.5-8 after solvation. #18b doesn't have

acrylic acid NHS ester, and #19b1/2 are just polyacrylamides. #19b1 and #19b2 have almost the same composition. The volumes are "per well" values. Actual batches were about 5 times the listed values.

Table 19. Schematic of wells and design of experiment. Rows A and B contained hydrogel with GFP-acrylate. Rows D and E contained hydrogel with GFP. Prior to the addition of TEMED, the pH was checked and adjusted for key wells (prior pH / μL 12M NaOH added / resulting pH). BL=10XPBS only. For explanation of times see figure associated with the syringe experiment.

List of Equations

- 1) Reaction rate constant and characteristic time constant.
- 2) Arrhenius model for characteristic time constant.
- 3) Time constant as a function of force.
- 4) Force-modified reaction rate constant.
- 5) Reaction rate constant modified with force and experimental setup conditions.
- 6) Bayes' theorem in terms of reliability.
- 7) General formula for reliability.
- 8) Reliability in constant failure rate.
- 9) Folding rate constant and average time of unfolded state.
- 10) Unfolding rate constant and average time of folded state.
- 11) $F(x)$, WLC model.
- 12) Two-state Markov model for unfolding.
- 13) Reaction rate constant.
- 14) Two-state Markov model for folding.
- 15) First-order reaction model with constant force.
- 16) Equilibrium under force.
- 17) Reaction path length.
- 18) Bond stretch potential.
- 19) Angle-bending potential.
- 20) Urey-Bradley term.
- 21) Dihedral angle potential.
- 22) Improper dihedral angle potential.
- 23) Electrostatic energy.
- 24) van der Waals energy.
- 25) Shear modulus.
- 26) Viscosity.
- 27) Complex and stress relaxation moduli.
- 28) Gel fraction.
- 29) Noise amplitude and photon count.

Chapter 1. Introduction

Mechanotransduction

The mammalian cell's mechanical interaction with its environment plays a critical role in a variety of biological phenomena, such as tumor growth (Huang and Ingber, 2005), apoptosis (Wernig and Xu, 2002), vasculature development (Orr et al., 2006), and vascular remodeling (Lehoux et al., 2006). These systems rely on a variety of cellular components such as stretch-activated channels and integrins (Ingber, 2006), as illustrated in Figure 1. Many of these mediators of mechanotransduction are only small parts of much larger frameworks. For example, when ligands of the extracellular matrix such as ICAMs and VCAMs bind to integrin receptors, mechanical cues are transferred to the intracellular cytoskeleton (Katsumi et al., 2004). Stretching the cytoskeletal network alters the thermodynamics of cytoplasmic protein-protein interactions in a manner independent of local ionic states (Sawada and Sheetz, 2002). The subsequent binding of cytoplasmic proteins to the cytoskeleton leads to the activation of signaling cascades through tyrosine phosphorylation (Tamada et al., 2004). This "integrin-cytoskeleton" pathway is but one example of phenomena where discrete structural elements inside the cell appear to respond to both tension and compression (Wang et al., 2001b). Such events, repeated numerous times, are thought to result in cell- and tissue-scale changes in the organism.

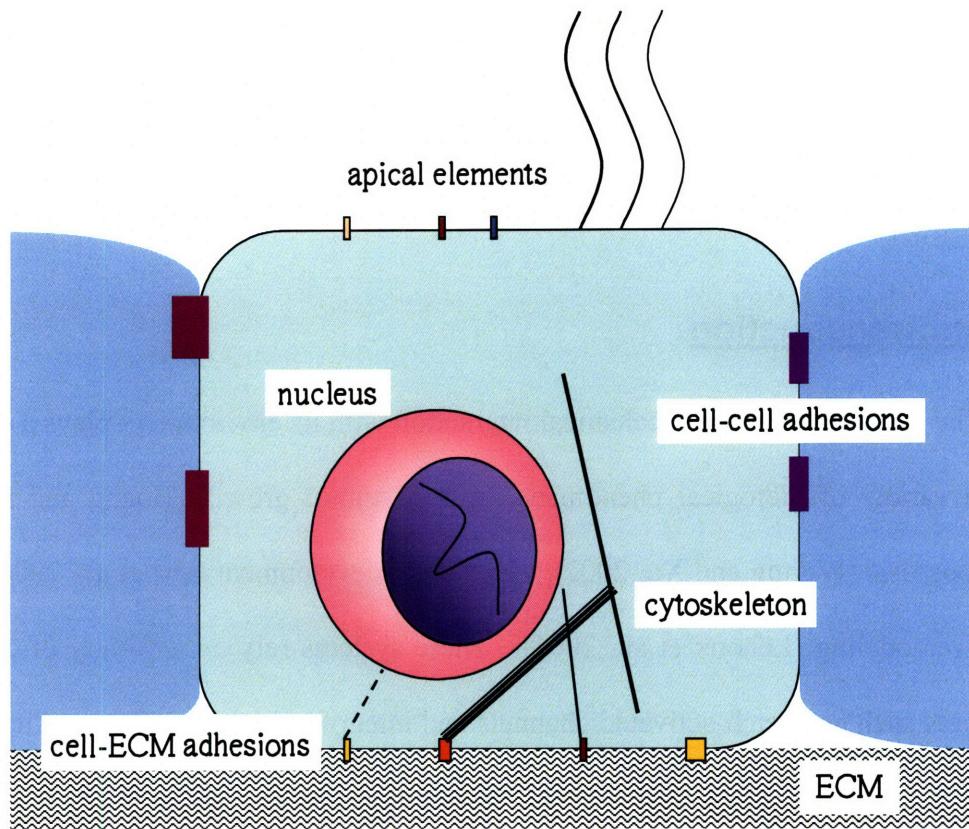


Figure 1. Mediators of Mechanotransduction. Many parts in the mammalian cell are involved in mechanosensation (Ingber, 2006). The cell-ECM area contains focal adhesions, within which integrins play a key role in binding to RGD peptide sequences in the extracellular matrix (ECM). The ECM, which is often the basement membrane, contains proteoglycans, collagen, and fibronectin. Fibronectin has cryptic sites that allegedly become accessible upon stretch. These stretches also affect cell-cell adhesions, such as cadherins and gap junctions on the lateral surface of the membrane. On the apical membrane surface are surface processes, such as primary cilium and stereocilia, that dwarf the surface receptors, the transmembrane ion channels, and the caveolae on the cytoplasmic side. Within the cytoplasm cytoskeletal elements, such as microfilaments, microtubules, and intermediate filaments, can convey mechanical effects from the surface to interior structures. One major structure is the nucleus, which has its own ion channels in the nuclear lamina. Finally, inside the nucleus genetic material uncoils into chromatin during gene expression; this unwinding process itself has mechanical considerations unexplained by chemical means alone.

At all levels of biological organization, life can respond to force. At the macroscopic level, dermal tissue will respond to compression and tension by distributing the mechanical stress and strain across its components (Silver et al., 2003b). In particular, tension in the epidermis will result in tension at the basement membrane of the basal epithelial cells. In this way, the epidermal basement membrane transports stretch

information to the basal epithelial cells. Below the epidermis, the collagen fibrils in the dermis will undergo stretch that affects nearby fibroblasts. Therefore, the collagen matrix itself is also a potential vehicle, transmitting information across the entire lengths of its fibrils. At the cellular level, the fibroblasts are attached to the fibrils and the basal epithelial cell junctions attach the members of an entire cell layer to each other. Mechanotransduction occurs inside cells and in extracellular cryptic sites, such as those found on fibronectin. Therefore, a macroscopic mechanical input will be distributed across tissues where individual cells sense and respond to force; this collectively makes a tissue-scale effect.

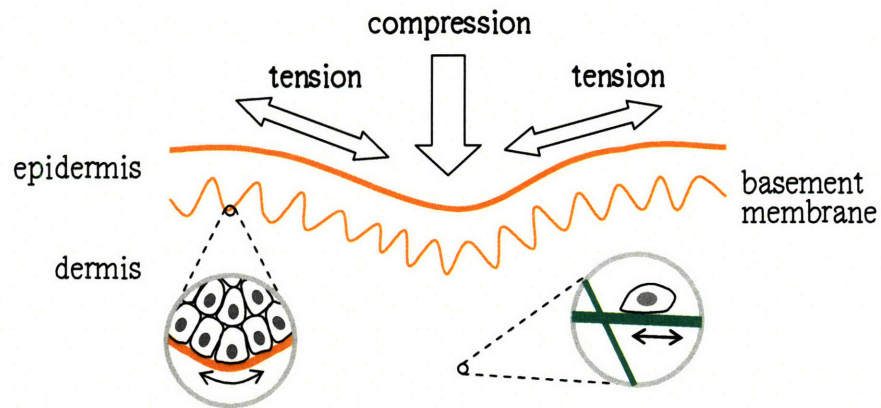


Figure 2. Force transmission in skin. Adapted from (Silver et al., 2003b) Mechanical distribution occurs in terms of all levels. At the tissue level, the basement membrane and collagen fibrils are transporting messages. At the molecular level, fibroblasts respond to continual change in force through the $\alpha_5\beta_1$ integrins (Silver et al., 2003b). Incidentally, the vertebrate hair cell mechanotransduction apparatus has striking similarities with that of *Drosophila*; mechanosensory systems are conserved from vertebrates to invertebrates (Gillespie and Walker, 2001).

These responses to changes in mechanical conditions are also time-dependent. For example, the persistence of blood pressure ensures that the blood vessel wall is always under vessel stretch. (The vessel wall also experiences fluid shear stress from the friction of blood against the endothelial cell layer.) Acute pressure changes result in vasodilation, release of vasoactive agonists, and myogenic tone adjustments (Lehoux and

Tedgui, 2003). However, chronic pressure results in permanent changes that may be deleterious to the distribution of blood.

Tissue-level mechanics information is distributed to cells that respond biochemically, but what are the details at the subcellular level? At the plasma membrane, mechanical signals appear to be transmitted across the membrane by specific receptors (Meyer et al., 2000). These cell surface receptors are likely to be part of protein complexes associated with the cytoskeleton, since mechanical cues to the cytoskeleton-related transmembrane proteins result in stronger response than cues to unrelated ones (Wang et al., 1993). The heterogeneity of receptor-cytoskeleton mechanical coupling are evident in measurements of cell stiffness, which depend on the choice of the cell membrane receptor.# Further examination of these transmembrane proteins revealed the following list of mechanically coupled proteins in order of decreasing biochemical responsiveness (Meyer et al., 2000):

integrin $\beta 1$ > PECAM > integrin $\alpha_v\beta_3$ > E-selectin >

integrins α_5 , α_2 , and α_v >>> acetyl-LDL receptor > HLA antigen.

Receptor-dependence is therefore observed in both chemical and mechanical responses. Such transmembrane effects appeared to travel inward as far as the nuclear envelope, presumably by means of cytoskeletal tethers (Chicurel et al., 1998). From these and similar experiments emerged a perspective of the mechanical cell. This perspective – the transmission of mechanical effects across the intracellular cytoskeletal structure – suggested the validity of the tensegrity theory of cellular mechanics (Ingber, 2003). Tensegrity theory proposed that the mechanical cell was like a tent, where internal “struts” and “tethers” are connected to the surroundings by transmembrane anchors. This tensegrity-driven mechanical cell model can be used as a framework onto which a

composite picture can be pieced together from the identification and characterization of individual protein-actors.

Of the many members of the cast, which proteins have a roles in mechanotransduction? If mechanical cues travel inwards, then who is receiving the message? One candidate is the protein zyxin, a regulator of actin filament assembly in the cell. Upon exposure of the cell to cyclic stretch, zyxin will dissociate from focal adhesions and accumulate in the nucleus (Cattaruzza et al., 2004).

If there *is* mechanical communication, then can it be demonstrated in a context where biochemical mimicry can be largely precluded? In one case, the transient elimination of cellular biochemistry was achieved by subjecting cells to the detergent triton (Sawada and Sheetz, 2002). The remaining triton-insoluble component – much of which was the cytoskeleton – demonstrated a change in affinity for paxillin, focal adhesion kinase, and p130Cas in a stretch-dependent manner (Sawada and Sheetz, 2002). The fact that triton-insoluble cytoskeleton can respond in a stretch-dependent manner demonstrates the existence of a mechanism that, during the stretch phase, is not dependent on thermodynamics observed in physiological models. Hence, biochemistry cannot be an alternative explanation for the apparently mechanically stimulated response of these cytoskeletal structures.

Even if a few proteins experience altered binding thermodynamics by stretch, does stretch itself really make that much of a difference to the overall cell behavior? This question was addressed by Tamada et al, who demonstrated the activation of a signaling cascade by stretching of a triton-insoluble cytoskeleton similar to the Sawada-Sheetz version (Sawada and Sheetz, 2002; Tamada et al., 2004). Because signaling cascades are

mechanisms where a relatively small amount of initial signaling can release a geometrically magnified message downstream, cytoskeletal stretch does indeed have the potential for cell-wide response.

If mechanical signals do change into biochemical ones, then what are the proteins that undergo mechanotransduction? Mechanotransduction in this sense is the ability for a protein to have both mechanical and chemical interactions – which are related – with its surroundings. Defining mechanotransduction at the level of conformational changes and time-dependent effects would be an elucidating endeavor.

To begin addressing the question of molecular mechanotransduction, one might ask, "at the scale of macromolecules, how might mechanical changes manifest themselves into chemical outputs?" The cell could sense an alteration in the balance of forces through either the crossing of a threshold of a critical thermodynamic property, or a conformational change (Goldmann, 2002). For example, mechanical stress on the catalytic domain of the muscle protein titin results in domain unfolding and exposure of the active site of titin kinase (Grater et al., 2004). Similarly, fibronectin is also known to have cryptic sites that demonstrate binding ability once they gain exposure (Vogel, 2006). At least one of these sites are known to be exposed upon upregulation of cell contractility (Zhong et al., 1998).

The above discoveries on cellular and subcellular mechanotransduction were achieved by means of a variety of methods, such as bead manipulation by optical tweezers, atomic force microscopy (AFM), and magnetic microneedles (Bai et al., 2006; Matthews et al., 2004; Samori et al., 2005). These approaches have been used to make force measurements from outside the cell, but these instruments are too large to fit inside

the cell. Instead, key intracellular structures are adapted into probe-friendly, isolated systems outside of the cell and accessible to instruments. For example, the Ig domain I27 of the muscle protein titin was unfolded by AFM (Oberhauser et al., 2001). A polyprotein of 12 identical repeats of I27 was stretched at constant velocity (velocity-clamp mode); this resulted in a force-extension plot with a sawtooth pattern, where each tooth corresponded to one Ig domain. Under velocity-clamp conditions, the I27 modules unfolded at forces just above 200pN. In another example, a combination of optical tweezers and fluorescence microscopy was used to demonstrate that bare DNA was more vulnerable to stretching than DNA complexed with a fluorescent Rad51 recombinase (van Mameren et al., 2006). These well-defined systems generate quantitative data and demonstrate the value of single molecule experiments.

On the other hand, the role of individual molecules in the context of the complex interior of a cell is not yet well-studied (Ingber, 2006). To explore the cell structure in molecular mechanical detail, the first step is to take advantage of the accumulating quantitative data on isolated parts. When isolated components are characterized in quantitative terms, the relevant pieces – some of which may tend toward opposing phenomena – can be brought together to arrive at quantitative models. How well piece-wise studies can collectively approximate events inside cells must then be verified, if possible, by intracellular measurements.

Measurement of intracellular mechanics

What should be measured in the context of intracellular mechanics? These mechanical interactions occur in a fluid environment, whose analysis typically begins with the calculation of the Reynolds number. The Reynolds number, which estimates the

ratio of inertial to viscous forces, suggests that at the length scales of cellular components, viscous effects dominate inertial effects (Deen, 1998). Therefore, from a continuum fluid mechanics perspective, the analysis of cell-environment interactions will likely take advantage of the conservation of momentum transfer. The momentum transfer rate, or force, would be a useful first-approximation concept to pave the study of cellular mechanics.

Measurement of intracellular forces will require sensors whose sizes do not perturb components of signaling pathways and protein complexes. This need is not met by the instruments currently employed. An AFM cantilever is $\sim 100\mu\text{m}$ long (NanoScience, 2006), which is larger than most mammalian cells. In an optical trap, the diameter of the bead is $\sim 500\text{nm}$, which is still enough to displace major subcellular structures. The development of an intracellular mechanical sensor would be the first step in quantifying force inside a cell.

An intracellular sensor for the purpose of measuring force should be well-characterized, minimal in its perturbation of the system, inert to other interactions, and easy to place inside the cell. An easy placement inside the cell hints at an endogenous production of the sensor. A requirement for low perturbation suggests that a light-emitting sensor might have the least effect on the system during the readout process. A well-characterized sensor should be something that has been used commonly, preferably in the biological research community. These considerations point to the green fluorescent protein and its variants as prime candidates.

Green fluorescent protein

The *Aequoria victoria* green fluorescent protein (GFP) has become one of the most widely used, well-characterized tools in the biological research community. Unlike other fluorescent proteins, GFP matures into the fluorescent state without the need for a cofactor other than one molecule of ubiquitous oxygen. GFP can withstand temperatures up to 65°C, fluoresce in a broad pH range (5-11 for wildtype), and fold into native state in the vicinity of a variety of chimera partners (Tsien, 1998). Compared with simple organic dyes, fluorescent protein-based probes can be introduced into a wider variety of cell types, used with a lower risk of photodynamic toxicity, and respond to a greater variety of biological phenomena (Zhang et al., 2002). GFP has been used as a gene expression marker, subcellular protein location marker, pH sensor, calcium ion concentration sensor, and oxidation potential sensor. While there are other GFP-like proteins, which serve as contingency options, GFP and its derivatives seem to comprise the most characterized family of fluorescent proteins.

How is GFP synthesized? Wildtype GFP's fluorescence is established after a series of post-translational modifications that involve at least three residues: ser65, tyr66, and gly67. These residues undergo a cyclization, oxidation, and dehydration reaction. However, the exact details of the fluorophore synthesis remain open to debate. Different groups have proposed different pathways for the maturation of the fluorophore. While Barondeau et al propose the sequence cyclization-dehydration-oxidation (Barondeau et al., 2005), Rosenow et al favors cyclization-oxidation-dehydration (Rosenow et al., 2004). GFP fluorophore biosynthesis is important to understand, because synthesis-

critical nearby structures (which otherwise seem less critical) can be preserved in the desing of new GFP variants.

GFP photophysics

The absorption, excitation, and emission spectra are affected by numerous factors including pH, temperature, ionic state, GFP protein concentration, and local environment (i.e. residue substitutions) (Heim et al., 1994; Ward et al., 1982). Kummer et al measured wtGFP spectra at a protein concentration of $\Delta OD < 0.3$, pH 8.0, at room temperature (Kummer et al., 1998) (see Figure 3). The challenging goal to correlate GFP structure to the observed photophysics has interested a number of groups (Barondeau et al., 2005; Bell et al., 2003; Brejc et al., 1997; Chatteraj et al., 1996; Jung et al., 2005; Kummer et al., 1998; Striker et al., 1999; Weber et al., 1999; Wiehler et al., 2003). Although there is still some disagreement, it appears that a consensus is beginning to emerge.

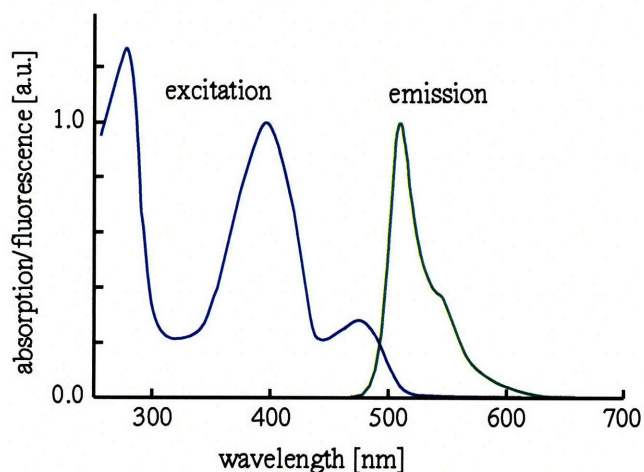


Figure 3. GFP Fluorescence spectra. Adapted from (Kummer et al., 1998)

In the wildtype, spectroscopic data implies three ground states that are in equilibrium with each other (Brejc et al., 1997): A, I, and B. The A form (also called RH) is the protonated species. The I and B forms are both deprotonated (i.e. R-) at tyr66. The difference between I and B is that I is an "unrelaxed" form of B. GFP in I (or Intermediate) form, which exists usually for brief moments, has a solvation environment that is closer to that of A rather than that of B. Weihler et al have estimated the free energy differences between the three forms (Wiehler et al., 2003). The I form is 7.6 kJ/mol above the A form, whereas the B form is 3.7 kJ/mol above the A form. All three ground states have corresponding excited states (marked with asterisks):

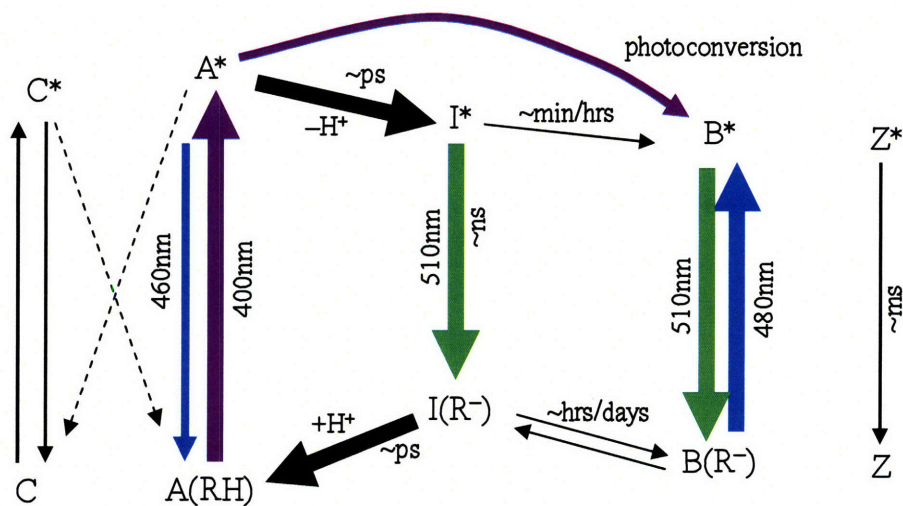


Figure 4. GFP state pathways. This diagram is the combined result of papers referenced above.

By means of residue substitutions, Weihler et al were able to isolate each GFP ground state and estimate individual contributions to the overall absorption spectra (Wiehler et al., 2003).

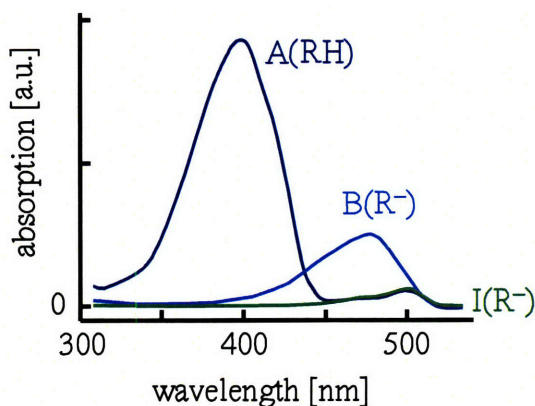


Figure 5. Estimation of contributions of each GFP state to the overall absorbance spectrum. Adapted from (Wiehler et al., 2003). The overall absorption spectrum depends on the relative distributions of the three major forms of GFP. This distribution can change with concentration, since dimerization will increase the free energy of the B form.

Thus, any conformation change that favors one over the other would result in a change in the overall absorption spectra.

Upon irradiation by UV light, forms A, I, B, and their excited states can also undergo a process called photoconversion, in which a carbon dioxide molecule is removed from glu222 (Bell et al., 2003).

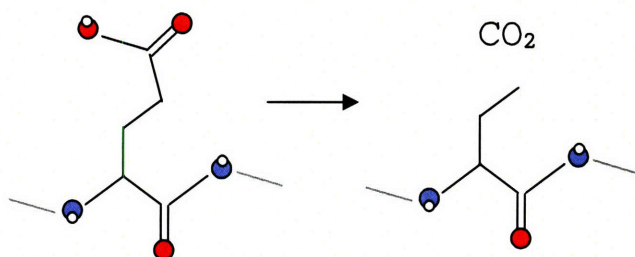


Figure 6. Photoconversion. Ultraviolet irradiation can induce GFP to undergo photoconversion, in which a carbon dioxide molecule is removed from glu222.

CO₂ is made from one δ carbon and two ϵ oxygens. This reaction at E222 results in the stabilization of the B form. Consequently, the relative intensities of absorption at 400 and 480 nm make a significant shift.

Residues like E222 are able to influence the photophysics of the fluorophore because of the potential for extensive hydrogen bonding between the fluorophore and its neighbors (Brejc et al., 1997). Photoconversion alters the local environment, and the emission path shifts away from the neutral to the anionic state. This effect can be

observed as a change in the ratio of the two major absorption peaks. Decrease of the B form back into the A form is a slow process, on the order of hours if not more.

Besides solvent quenching, the fluorophore itself can rotate about one or two bonds (i.e. ϕ , τ) to undergo nonfluorescent decay (i.e. dashed lines).

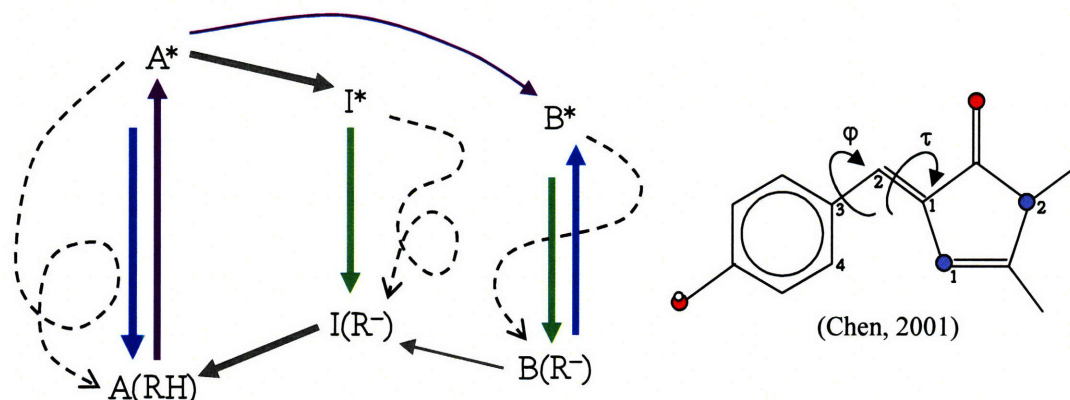


Figure 7. GFP relaxation mechanisms. (a) The GFP fluorophore's radiative relaxation pathways must compete with the alternative, non-radiative mechanisms. (b) A key non-radiative relaxation mechanism is the hula twist method.

Quenching by bond rotation depends on the degree of conformational freedom (or lack of steric hindrance by neighboring residues). Deformation by forced unfolding of the GFP molecule may allow enough conformational freedom before solvent quenching takes effect. Mutations can cause changes in relative rates of decay paths and alter the spectrum profiles, fluorescence lifetimes, and intensities.

How can GFP be used as a mechanical sensor? One way would be to allow the protein fluorophore to undergo solvent quenching as a result of mechanical inputs. A mechanically induced unfolding will expose the fluorophore to the aqueous solvent. In an implicit solvent model, simulations indicate that ~ 80 pN of tensile force is sufficient to expose the fluorophore's surface (calculated by van der Waals radii) within 25 ps. In an acidic (pH 2) or basic (pH 13) environment at room temperature, GFP underwent

chemical denaturation, and consequently the exposed fluorophore lost emission capacity (Ward and Bokman, 1982). The dilution of the denaturation buffer brought about a pH readjustment favoring the refolding of the protein. Protein renaturation was measured by the recovery of fluorescence, a sign that the fluorophore was once again insulated from the solvent. Solvent quenching can serve as the molecular basis of the mechanical sensor.

Configuring GFP

The protein sensor will then require linkers, which must be placed with care. This is because the mechanical response of a protein depends on the placement of the tensile force. For example, the load needed for destabilizing ubiquitin was shown to be linkage-dependent (Carrion-Vazquez et al., 2003). These configurational options were elucidated as a result of the wide use and many characterizations of GFP that are documented in the literature. The overall GFP structure is a cylinder often termed the “beta-can,” because it is a beta sheet wrapped into a cylinder with loops that cover the ends of the cylinder. In addition to the ends of the corresponding DNA sequence, basepair positions that correspond to peptides 157 and 172 are viable positions for insertions of other peptide moieties (Freyzon, personal communication). In fact, the GFP DNA sequence can undergo circular permutation and place the termini at the peptides positions that were originally 157 and 172 (Topell et al., 1999). In other words, one can redesign GFP so that the peptide sequence starts with wildtype amino acid 157, connects wt amino acid 230 with wt amino acid 001, and finally ends at wt amino acid 156. This presents an opportunity for a potential isometric force sensor later on.

In addition, photobleaching is an important issue, especially when the fluorophore is subjected to light from both the optical tweezers and excitation laser. Some of the

ways photobleaching has been addressed are the use of a bleaching correction equation (Kolin et al., 2006), mutagenesis (Chirico et al., 2005), and local oxygen removal (Bernas et al., 2004), and protocol adjustment.

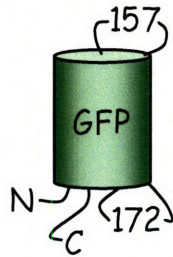


Figure 8. Viable positions on the GFP for engineering a fusion protein.

The use of GFP as an intracellular force sensor would require natural attachment sites connected to the fluorescent protein. One candidate is LIM, the cytoskeletal binding domain. As a first step, chimeras can be made to measure the efficiency of folding in the presence of a chimeric partner.

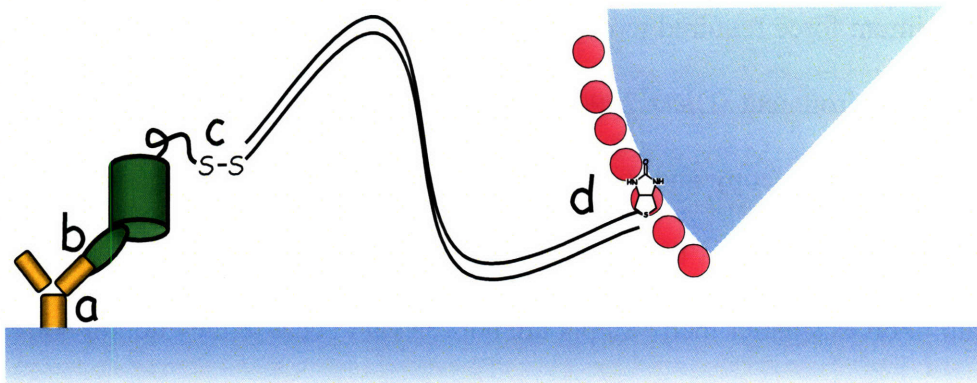


Figure 9. Schematic of linking elements. (a) Non-specific binding will link glass surface and antibody. (b) The anti-hemagglutinin antibody will attach to the HA moiety fused into a loop of the GFP. (c) The linking reagent SATP will be used to make a sulfhydryl group on the N-terminal amine on GFP, followed by deprotection and linkage with the 5'-thiol on the DNA tether. SATP must not be allowed to modify the antibody's N-termini, nor any of the lysine amino groups. Because of this complexity, the S-S bond formation may need to be made first. (d) 5'-biotin on the other end of the DNA tether will link to a streptavidin-coated bead.

The raw data derived from force-fluorescence experiments must be analyzed in light of a few factors. For example, GFP is known to have at least three different non-

bleached states. Most GFP variants have multiple states, though the relative abundance of each may be different. In addition, at the level of individual molecules, the concept of material strength takes on a dynamic dimension. Therefore, an analytical approach that accounts for dark states of the molecule as well as the dynamic nature of material strength would be desirable, but for the beginning a characterization of the fluorescent state would be useful.

How can one characterize the fluorescent state? Figure 9 shows one schematic for the calibration of GFP. The “pizza slice” at the upper right in the figure represents a bead that can be manipulated by an optical tweezer. This approach was considered a viable method to pull the GFP to a few reasons. First, the optical trap is an effective force application device from ~ 10 to ~ 100 pN. The maximum force of 100 pN is greater than the minimum force required to deform the GFP beta-can and significantly affect the fluorophore’s environment (Dietz 2004). In addition, the alternatives to the optical trap are atomic force microscopy and magnetically induced forces on magnetic beads; these instruments have force ranges that overlap and/or exceed the upper range of force of the optical trap. Forces smaller than ~ 10 pN are not relevant because they do not correspond to physiologically interesting phenomena in this context. Thus, the optical tweezer, the atomic force microscope, and magnetic field-inducing coils comprise the set of current options for pulling GFP.

Unraveling the fluorescent protein requires that other segments and connections can withstand the necessary force. This threshold force depends on numerous factors, such as the attachment configuration. The literature suggests a value of 35pN at which point the GFP becomes thermodynamically unstable (Dietz and Rief, 2004a). These

values are in the range of magnitudes beyond which antibodies start to unfold (Brau, personal communication). On the other hand, the goal here is to not completely unfold the protein, but to alter it just enough to be able to measure the change in fluorescence behavior.

Fluorophores change their emission spectra in response to changes in the local environment, and there are multiple mechanisms that can quench a fluorophore. Therefore, it would not be surprising to see changes in the emission spectra during the single molecule experiment with the relatively weak antibody link. While the current effort is focused on quenching by solvent collision, it may be possible to infer other mechanisms from qualitative observations by using a computer simulation. Comparison among GFP mutants show that the slight structural alterations conferred by residue changes can alter the energy relationships between the GFP conformations (Creemers et al., 2000a).

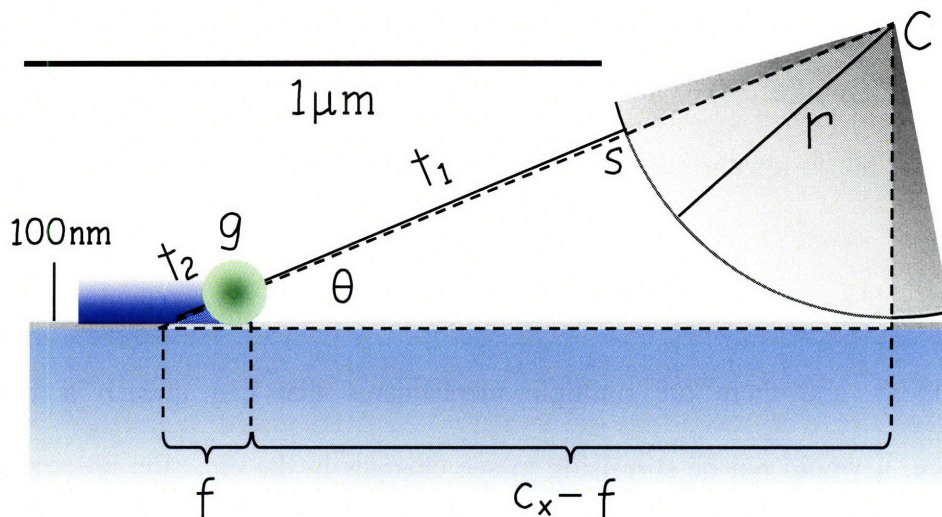
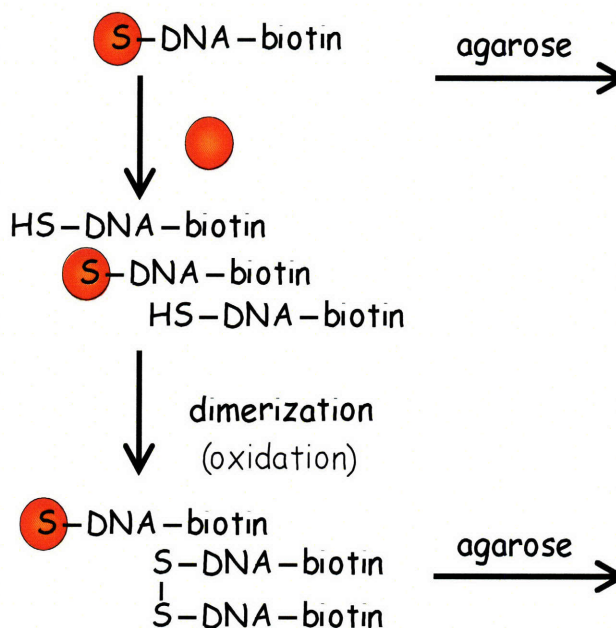


Figure 10. Scaled schematic of configuration. C, S, and g are points: g, position of GFP; s, position where tether and sphere attach together; c, center of bead. The variables f, t₁, t₂, and r are lengths: f, radius of measured fluorescence volume; r, radius of bead; t₁, length of DNA tether; t₂, length of tether 2 (which is essentially the antibody). Theta (θ) is the angle between the glass and taut tether construct.

Figure 11. Testing the DNA tether. Following a deprotection step, an oxidative environment that dimerizes the DNA tethers by means of disulfide bond formation should readily show its effect on a standard 1.5% agarose electrophoresis. Dimerization should give a major band at 3kbp and a minor band at 1.5kbp, while the untreated control should give one major band at 1.5kbp.



One way to link the protein to a bead is by means of a DNA tether. At the ends of this tether, two linking systems can be employed: a disulfide bond and a biotin-avidin linker. The biotin on the 5' position will link to an avidin-coated sphere. On the other

hand the disulfide bond formation will occur with the help of chemically attached sulfhydryl groups on GFP. The sulfhydryl functionality of the DNA tether can be tested by dimerizing a sample of DNA and running an agarose gel electrophoresis (see Figure 11).

Exploring configurational benefits

Fluorescence quenching by GFP unfolding implies the extension of a structure that contains the sensor. When the sensor perturbs the apparent stiffness of the structure of interest, the biological behavior may be affected. This concern is especially important when one requires tension without extension, or pre-stress. Pre-stress, or isometric tension, is a common phenomenon in biology (Ingber, 2006). For example, cell behavior is affected by the stiffness of the substrate (Engler et al., 2004), and a poorly configured GFP sensor might substantially diminish the apparent stiffness of the extracellular matrix. Because a sensor should not disturb phenomena with pre-stress, a GFP sensor that does not allow a lot of extension, or unfolding is desired.

Another problem that worsens with the extent of unfolding is GFP's incomplete recovery after unfolding. Ward and Bokman denatured wildtype GFP in an either acidic (pH 2) or basic (pH 13) condition (Ward and Bokman, 1982). Renaturation was measured (in terms of fluorescence intensity regained) as a function of dilution level of denaturing buffer and time in minutes. Even in the best case, maximum fluorescence recovered did not exceed 60%. In addition, circular dichroism data indicated that the conformation did not recover completely to the original state. A sensor that was perturbed to a smaller extent would probably recover more completely at a faster rate.

Therefore, both isometric force sensing and recoverable fluorescence are expected to be affected by the extent of protein unfolding. One way to address the above is to make a GFP configuration that allows minimal unfolding upon load application. In other words, the sensor should reach the stiffness of covalent bonds after only a small displacement.



Figure 12. Two configurations for force sensing. (a) The structure on the left will completely unfold if one pulls the structure at the RGD peptide sequence. (b) The structure on the right is expected to unfold only part way, because the RGD peptide under tension would merely straighten the curves out of an already somewhat straight beta strand.

In Figure 12, both GFP's will be anchored on a surface largely covered by polyacrylamide, or another substance usually inert to cells. Engineered into the GFP is the RGD sequence, which is the essential portion of fibronectin that binds to integrin. In the first configuration, RGD is attached to the C terminus of GFP. An attachment to the RGD that applies a tensile force perpendicular to the substrate, will continue to unravel the protein until a couple hundred amino acids form a linear chain many times longer than the native structure. On the other hand, the second configuration is expected to withstand sub-covalent bond-breaking forces after relatively little extension. Because the RGD sequence is engineered into a loop that is connected after a peptide of one beta strand to the substrate, an application of load would only affect one beta strand of the GFP. Such a relatively subtle change is presumed to be sufficient to affect fluorescence

intensities because mutagenesis experiments that made seemingly subtle changes to the beta-can residues are known to have had significant consequences on the fluorescence properties of GFP (Creemers et al., 2000a).

To use GFP as an intracellular isometric force sensor, a similar configuration as the extracellular one is possible, as shown in Figure 13. The isometric GFP sensor, if viable, can be configured with two binding domains so that native attachment behavior can be characterized for future force-sensing usage. In the event of misfolding, additional linkers for fusion proteins can be explored (Arai et al., 2001).

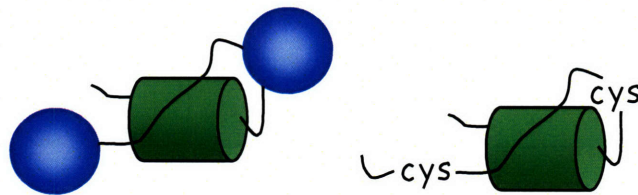


Figure 13 Schematic for an intracellular force sensor. (a) The structure on the left represents a GFP with two binding domains. **(b)** The structure on the right represents a GFP with cys residues in place of the binding domains, for extracellular calibration of the sensor.

Before making the above systems, it would be useful to understand the mechanical characteristics of the relatively weak components: the antibody, the antibody-antigen bond, and the biotin streptavidin bond. The above structures can be checked to see if they can withstand the force-loading requirements for perturbing the GFP structure. While individual parts have been tested by other groups, it is also true that alterations in configurations or changes in the environment (e.g. temperature) can affect the strength of various structures. To carry out strength tests under similar conditions in a relatively inexpensive manner, one can employ the molecular dynamic software CHARMM.

Candidate Domains for Possible Fusion with GFP

Measuring intracellular force depends on GFP's ability to interact with mechanically relevant structures in cells. Cellular behavior has been modeled as a tensegrity structure where the cytoskeleton is assumed to play the role of a pre-stressed, interconnected network (Sultan et al., 2004). This perspective was also consistent with microscopic analyses of mechanical behavior in living cells (Wang et al., 2001a). Therefore, intracellular mechanical interactions might best be studied if GFP were designed to interact with cytoskeletal proteins.

To retain the benefit of endogenous sensor production, GFP's DNA sequence can be ligated to sequences that code for protein interaction domains. This strategy – the combination of modular protein domains – enables nature to use relatively simple interactions between domains to form the foundations of complex intracellular communication (Pawson, 2004) .. In other words, GFP can be fused with cytoskeletal protein binding domains.

To identify binding domains relevant to cell mechanics is to filter through databases of protein-protein interactions. Binding to and associating with ubiquitous cytoskeletal elements is a domain characteristic that in a database query would serve as a useful filter. Another criterion would be the existence of a review of the protein domain, because only well-studied domains would merit a review article. Ideally, such papers will note both the effect of binding on partner elements, as well as the residue sequence. The sequence length is an important factor in fusion protein synthesis considerations. Downstream of protein synthesis is the question of whether the chimera and its partner can bind. Binding ability, often characterized in terms of the equilibrium dissociation

constant, would make another useful addition to the list of criteria. With the above considerations in mind, one can undergo an otherwise overwhelming survey of recent literature and protein domain databases. The European Bioinformatics Institute (EBI), part of the European Molecular Biology Laboratory (EMBL), presented a website linked to a few promising databases.

The EBI Gene Ontology database (GO) was accessed through the “QuickGO” GO browser (Consortium, 2000; Consortium, 2006). This interface allowed a query for actin, microtubules, tubulin, and intermediate filaments. This resulted in the categories “function – actin binding,” “function – tubulin binding,” and “function – intermediate filament binding.” The categories resulted in a list of protein, family, and domain names, which were filtered for “Type Domain.”

The EBI InterPro database webpage had a list of domain entries. All entries with the term “binding” were considered. Domains that had small-molecule binding partners (e.g. carbohydrates, metal ions) were filtered out because the target partners were major cytoskeletal structural components. Other binding domains had partners such as cellulose, DNA, RNA, and chitin. Cellulose and chitin are not products of mammalian cells, so the corresponding entries were skipped. DNA- and RNA-binding domains were skipped because there was not an apparent and efficient way to separate binding domains with a mechanical role from binding domains that had more to do with control of gene expression than with mechanics. All domains binding to one of the following partners were initially kept: actinin, tubulin, fibronectin, and collagen. Domains that bound to fibronectin were, in terms of InterPro accession numbers, IPR008616, IPR013552, and IPR000562. Domains that bound to collagen were IPR008456, IPR000562, and

IPR008970. However, they were not further examined because extracellular force sensing does not require a fusion protein solution.

Augmenting the database queries was a search done on Pubmed for review articles in English with titles or abstracts that contained terms similar to those used above.

The results of the searches were combined into one list. There were obvious redundancies, but this ensured a more comprehensive coverage. For example, the protein domain EB1 was missed in InterPro (because the entry did not have “binding” in its entry name) but was found under the QuickGO search. The literature search resulted in the addition of the LIM domain, which technically binds zinc ions, but this domain has been noted for its association with cytoskeletal elements. Finally, the initial lists of tubulin-binding domains did not seem to overlap at all.

Tubulins, the building blocks of microtubules, are assisted in its folding pathway by proteins that have domains called the tubulin binding cofactors A and C (TBCA and TBCC). TBCA has 99 amino acids whereas TBCC has 117 amino acids. (Cofactor D can allegedly form a complex with tubulin, but neither InterPro nor GO had an entry for it).

Polymerization can be promoted by a synergistic combination of the Adenomatous Polyposis Coli (APC) protein and the EB1 protein. The EB1 protein contains the EB1 domain, and this 49-residue, C-terminus module binds to microtubules in way that recruits the APC protein to the plus end of the microtubule. The APC protein itself binds to both cytoskeleton and EB1. This is accomplished by the EB1 binding domain at the APC protein’s C-terminus, and the microtubule-binding APC basic

domain, which is ~327 amino acids long. With this combination, polymerization commences. In contrast to the EB1-APC mechanism, proteins that contain the Tau protein domain (~31-residues long) have a role in preventing the depolymerization of microtubules. The proteins with Tau domains are common in neurons and known for their role in Alzheimer's Disease.

The above tubulin- and microtubule-binding domains present ramifications. First, the EB1 protein cannot induce polymerization by itself. Therefore, a non-polymerizing method of fusing GFP might be the use of the tubulin-binding EB1 module without components that bind to the APC protein. Incidentally, Pubmed lists two reviews for the EB1 protein. Second, the Tau protein domain is not commonly found outside neuronal tissue. This fact may present an opportunity if one can examine the 13 reviews on the Tau protein family. In contrast to EB1 and Tau, no reviews could be easily found for the APC protein and the cofactors in the context of binding to microtubules.

In addition to tubulin-associated domains, another set of promising candidates were the domains that had been identified as actin- or microfilament-binding modules. Actin-binding proteins were classified with a focus toward structure (rather than function), because module-derived functions were not of interest. In addition, binding-induced functions were assumed to be correlated with structures.

First, the Calponin Homology (CH) domain is known for its ability to bind F-actin. This crosslinking ability of proteins such as alpha-actinin and filamin seems to stem from having two tandem repeats (totaling 250 residues) at the N-terminus. Incidentally, calponin, having only one of these 110-residue modules at its N-terminus, seems to rely on other means to bind F-actin.

Second, the Formin Homology 2 (FH2) domains are 400-residue modules that bind to the barbed end of the actin filament (Higgs, 2005). FH1, often found to the N-terminal side of FH2, is known for binding the profilin protein as well as the SH3 and WW domains. In general, formin family proteins are implicated in actin filament assembly.

Third, the Villin Head Piece (VHP, also “gelsolin fold”) domain comprises ~76 amino acids at the C-terminus of over a 100 proteins, including the prototypical villin protein. Not all headpieces are motifs that intrinsically bind F-actin. Moreover, the VHP and VHP-like motifs that do bind do so with low affinity. Therefore, a careful sequence selection that is based on its binding ability is especially important here.

Another domain in the protein villin is the GEL domain, which is also found in gelsolin and supervillin. These domains enable gelsolin to bind, sever, and cap the actin filaments.

Another domain associated with the disassembly of microfilaments is the Actin Depolymerizing Factor (ADF) domain is 130-170 amino acids long. It is involved in severing F-actin and sequestering G-actin from polymerization. This function appears to resemble that of the GEL domain, but this is not surprising given that there appears to be a structural similarity with the GEL domain (Lappalainen et al., 1998). ..

Profilin binds to actin monomers in a one-to-one ratio. This protein appears to play a role in both polymerization as well as depolymerization... The well-conserved region at the N-terminus is thought to bind actin, but the rest of the protein is more variable. For example, whereas yeast profilin is 125 residues long, bovine profilin is

made of 140 amino acids. No domain name was readily available. Nevertheless, keeping track of studies on the binding of profilin and the cytoskeleton may be fruitful.

The I/LWEQ domain at the C-terminus enables talin to couple integrin proteins to the actin cytoskeleton (Critchley, 2000; Critchley, 2004; Critchley, 2005). Because talin is ~240kDa, a GFP-containing chimera protein should be able to fit into the focal adhesion complex where integrins and F-actins come together. Therefore, the I/LWEQ domain may be a good candidate for studying cell motility in fibroblasts.

The CTD (C Terminal Domain), comprises the C-terminus of the 4.1 protein family in humans and frogs, but not in flies (Scott et al., 2001). The 4.1 proteins are known for their role in maintaining plasma membrane integrity in erythrocytes. While the N-terminal FERM domain links to the plasma membrane via glycophorin C and guanylate kinase (p55), the CTD plays a role in linking spectrin and actin together. The exploitation of this domain might be useful in characterizing the mechanical effects of capillary blood flow on the erythrocyte. Such studies of red blood cells may shed light on the structural fragility of red blood cells in sickle cell anemia.

The diminutive WASP-Homology 2 (WH2) domain is the essential module of the Wiskott-Aldrich Syndrome protein for the regulation of the cytoskeleton. Because the WH2 domain is only 18 residues long, the “peptide” is an ideal candidate from a protein synthesis perspective. _

Finally, LIM is a cysteine rich, tandem zinc-finger structure that plays multiple roles in intracellular structure. Natural fusion partners include SH3, LD and PDZ (. IPR001781)(Kadmas and Beckerle, 2004). There are 25 conserved residues, and 20-34 spacer residues. Some example proteins are: EPLIN, epithelial protein lost in neoplasm

(has two actin binding domains); ABLIM, actin-binding LIM protein; ALP, alpha-actinin-associated LIM protein; paxillin; and zyxin (PF00412).

Table 1. Protein domains considered for fusion with GFP. Domain abbreviations: ADF, Actin Depolymerizing Factor; APC, Adenomatous Polyposis Coli; CH, Calponin Homology; CTD, C-Terminal Domain; FH, Formin Homology; LIM, Lin-11 Isl-1 Mec-3; TBC, Tubulin Binding Cofactor; VHP, Villin Head Piece; WAS, Wiskott-Aldrich Syndrome; WASP, WAS Protein; WH, WASP Homology. Partner abbreviations: a, actin; fa, F-actin; fa(barbed), barbed end of microfilament; fa(end), the end of microfilament; ga, G-actin; mt+, microtubule plus end; t, tubulin; zn, zinc.

Domain	Partner	Residues	Notes
TBCA	t	99	Binds to tubulin in conjunction with TBCD
TBCC	t	117	Assists in the release of tubulin from TBCD
EB1	mt+	49	At the C-terminus; involved in APC protein recruitment.
APC basic	mt+	327	Involved in EB1-APC polymerization mechanism.
Tau	mt	31	Has a role in microtubule stabilization and AD.
CH(x2)	fa	125(x2)	Two in tandem required for binding; involved in crosslinking.
FH2	fa(barbed)	400	Involved in microfilament assembly.
VHP	fa	76	At the C-terminus; not all VHP's bind F-actin.
ADF	fa, ga	130-170	Involved in depolymerization, sequestration.
Profilin	ga	125-140	At the N-terminus(?); binding domain not yet established.
I/LWEQ	fa	N/A	Involved in integrin-microfilament coupling. Promising possibility as GFP fusion partner to study the protein talin.
CTD	fa(end)	N/A	At the C-terminus. Involved in plasma membrane integrity. Promising opportunity with GFP for an in vivo study of RBC mechanics and the capillary system.
WH2	a	18	Involved in WAS; ideal from chimera perspective.
LIM	zn	25 + (20-34)	Binds 2 Zn ²⁺ ; 25 conserved and 20-34 spacer residues presents possibility for intra-domain engineering.

To summarize, a query under Pubmed, GO, and InterPro resulted in a number of possible fusion partners for GFP. The most promising fusion domain for cell motility studies appears to be the I/LWEQ domain, which as part of the talin protein is involved in linking integrin and microfilament components together. If one can manipulate talin's

I/LWEQ domain as well as the integrin-binding module, it may be possible to replace talin with a GFP-containing chimera protein. Another promising prospect is presented by the CTD, which plays a role in plasma membrane integrity by linking the cytoskeletal proteins actin and spectrin to plasma membrane components. If GFP can be linked to the CTD as well as the N-terminal FERM domain, there is a possibility to see how erythrocytes are mechanically affected by capillary blood flow. Because GFP has been successfully expressed in the rabbit, that animal may be the first animal model to attempt to implement a GFP sensor. The LIM domain is of interest because while its direct binding partners are two zinc ions, the domain is contained in zyxin, which seems to have a mechanical role (Yoshigi et al., 2005).

In comparison to the mechanically involved domains above, the rest of the modules seem unremarkable because it is unclear whether they can withstand enough mechanical load for a sensor application. Nevertheless, they are important to describe here as second tier candidates that may, with more elucidative research, turn out to be worthy force-bearing domains.

Summary

Tissue-level, macroscopic forces are distributed across extracellular structures, which inform cells of the external mechanical conditions via specific transmembrane anchors. As tensegrity theory suggests, these transmembrane anchors connect the cytoskeleton, whose biochemical properties are affected sufficiently by mechanical effects that cell-wide changes can occur. The responses of numerous cells are then understood at the macroscopic level as the tissue response to force.

To study these effects, a number of instruments have been used, but they are all too large to fit inside a cell without perturbing the intracellular environment. Therefore, an intracellular sensor would be useful in measuring forces and assessing intracellular, mechanical models. The green fluorescent protein is a candidate with desirable properties.

To use GFP as a mechanosensor, a number of issues must be solved. First, there must be a means to calibrate different configurations of GFP by means of an optical tweezer or atomic force microscopy setup. Parameters of configuration must be specified. Intracellular linkages must be determined.

The possible candidates for fusion with GFP were explored. Two promising candidate fusion partners are the I/LWEQ domain and the CTD domain.

Chapter 2. Dynamic Stability, Force and Energy

The effort to understand molecular biomechanics has resulted in the extension of established frameworks from chemistry and physics. However, the adaptation of a framework for one context to that of molecular biomechanics requires careful consideration of the similarities and differences. For example, classical mechanics must take into account the previously negligible thermal fluctuations that make molecular mechanics into stochastic processes. On the other hand, adapting to stochastic processes will still allow one to import concepts, such as “friction,” which is used to describe resistant forces in bond rupture. However, such characterizations must be applied without forgetting that phenomenological similarity doesn’t necessitate mechanistic similarity; underlying the perspective constructed from familiar terms is a world of molecules moving about endlessly with thermal energy.

Thermal energy and force adjusted kinetics

Thermal fluctuations have grown in importance with improvements in hardware resolution and the shift of focus of scientific inquiry beyond the ensemble-averaged world. Thermal energy’s effects could be observed in covalent bond-rupturing phenomena, where sub-threshold forces would - with the aid of a fluctuation – eventually result in rupture. The bond-breaking process therefore presented a relationship between applied load and lifetime. This relationship had been addressed to some extent in materials science (Zhurkov, 1965), and Bell proposed that a similar treatment might be useful in biology as well – that an increase in applied force would increase the rapidity

(or decrease the “lifetime) with which bond breaking occurred (Bell, 1978). Bell’s contribution was this subtle recognition of the roles of force and chance in rupture processes. The “lifetime” of a noncovalent bond can be thought of as the inverse of the kinetic off-rate constant:

$$\tau_{life} = 1/k_{off}$$

1) Reaction rate constant and characteristic time constant.

Then assuming an Arrhenius dependency of the off-rate constant, one can arrive at:

$$\tau_{life} = \tau_{oscillation} \exp\left(\frac{E_{barrier}}{k_B T}\right)$$

2) Arrhenius model for characteristic time constant.

where $(1/\tau_{oscillation})$ is the natural oscillation frequency ($\sim 1E-13$ sec) (Bell, 1978). The energy of activation for dissociation can then be lowered with a constant force f :

$$\tau_{life}(f) = \tau_{oscillation} \exp\left(\frac{E_{barrier} - fx}{k_B T}\right)$$

3) Time constant as a function of force.

where x is the distance along the reaction coordinate defined by the force vector. The effect of force on a potential energy function is depicted in Figure 14. —

Recasting the above equation and assuming first-order kinetics $r = kC$:

$$k(f) = \exp\left(\frac{fx - E_{barrier}}{k_B T}\right) = k_0 \exp\left(\frac{fx}{k_B T}\right)$$

4) Force-modified reaction rate constant.

Usually, a “machine” term k_m compensates for instrumental effects. Then, one can arrive at the following expression:

$$k(f) = k_m k_0 \exp\left(\frac{fX^\ddagger}{k_B T}\right)$$

5) Reaction rate constant modified with force and experimental setup conditions.

where k_0 is the rate constant without the effects of force and experimental machinery, X^\ddagger is the distance to the transition state, k_B is Boltzmann's constant, and T is temperature. The above equation formulates the assumption underlying the two-state Markovian model, that the rate of unbinding (or unfolding) was exponentially dependent on the applied tensile load.

Reliability theory

The stochastic aspects of bond rupture was made more explicit with Evans' introduction of reliability theory from the engineering discipline (Ben-Haim, 1952). From this starting point Evans' demonstrated that the agglutinin bond lifetime depended on the magnitude and duration of the force (Evans et al., 1991).

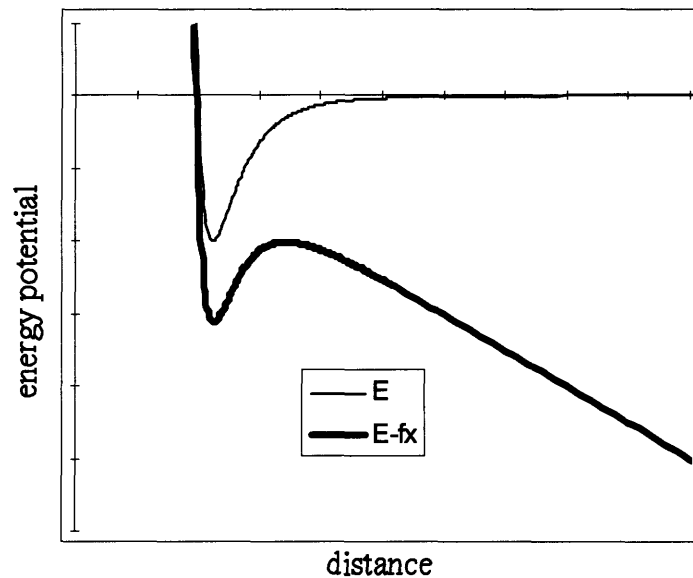


Figure 14. Lennard-Jones potential function under applied load. The original, force-free potential (thin line) and the force-adjusted potential (thick line) become further and further apart. Incidentally, this implies that when a binding potential has multiple energy minima (as in a noncovalent, protein-protein bond), outer energy pockets are affected greater than inner energy pockets.

Reliability $R(t)$ is the probability that a failure will occur after time t . Relating time and reliability requires one to start with the instantaneous failure rate $\lambda(t)$, which is the rate of failure for a group of intact bonds. In other words, $P(\text{reaction within } \Delta t_i \mid \text{no reaction up to } t_i) = \lambda(t_i)\Delta t$. The above three are related by Bayes' theorem $P(B)P(E|B) = P(E \cap B)$. Let $(E \cap B)$ equal "stability until $t + \Delta t$," let $(E|B)$ equal "stability within $\Delta t \mid$ stability until t ," and let (B) equal "stability until t ." Then

$$R(t + \Delta t) = [1 - \lambda(t)\Delta t]R(t).$$

6) Bayes' theorem in terms of reliability.

Taking the limit as $\Delta t \rightarrow 0$,

$$R(t) = \exp\left[-\int \lambda(t)dt\right].$$

7) General formula for reliability.

If $\lambda(t)$ is constant, then

$$R(t) = \exp(-\lambda t).$$

8) Reliability in constant failure rate.

Reliability is then an exponential function. Since λ has units of number of reactions per unit time per bond, the rate of reaction is given by $\lambda \times (\text{bond concentration})$. This implies first order kinetics. Therefore, first order kinetics is associated with an exponential distribution for probability of survival.

From a complementary perspective, $1 - R(t)$ is the cumulative distribution for random variable T , the time to reaction. Then the average time to reaction is given by

$1/\lambda$. In other words, given two protein states (folded and unfolded), one can use the duration times for a given state to arrive at its reaction rate constants:

$$k_{\text{folding}} = k_{\text{unfolded} \rightarrow \text{folded}} = k_{u \rightarrow f} = \frac{1}{\langle t_{\text{unfolded}} \rangle} \text{ and}$$

9) Folding rate constant and average time of unfolded state.

$$k_{\text{unfolding}} = k_{\text{folded} \rightarrow \text{unfolded}} = k_{f \rightarrow u} = \frac{1}{\langle t_{\text{folded}} \rangle}.$$

10) Unfolding rate constant and average time of folded state.

Bell and Evans hypothesized that other biological phenomena could also be modeled as stochastic processes, and confirmation eventually followed for both unzipping RNA hairpins (Liphardt et al., 2001) as well as unfolding proteins (Schlierf et al., 2004). Combining these results from noncovalently stabilized structures with experiments on covalent bonds showed that all of those phenomena could be comprehended within the same stochastic framework.

Thus, the framework incorporated Arrhenius' observations, the Eyring chemical reaction rate theory, Kramers Brownian diffusion rate theory, and reliability theory. The common framework, however, did not dictate a clear approach to study or characterize the conformational variability of unfolding proteins. Consequently, a number of methods have been attempted. protein unfolding studies have resulted in a number of methods, whose data are not always comparable. One approach to studying mechanical protein stability was to characterize chemical denaturation and draw an analogy to mechanical unfolding (Carrion-Vazquez et al., 1999). However, this approach has been open to controversy (Brockwell et al., 2005; Brockwell et al., 2003; Fowler et al., 2002; West et al., 2006). While chemical denaturation is achieved by altering thermodynamic stability (or the free energy difference between the denatured and folded states), it is thought that

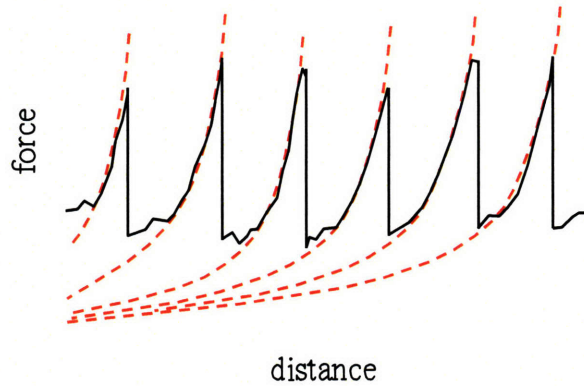
unfolding forces are affected primarily by the activation energy (the free energy difference between the transition and folded states)(insert ref. Li2000). Moreover, in chemical denaturation aspects of protein stability could only be studied in an average manner, whereas in single molecule methods even the trajectory of unfolding could be specified.

Velocity-clamp method

Instead of studying ensemble average protein stabilities, one can employ atomic force microscopy (AFM) to examine the mechanical response of a single molecule that is connected to both the AFM cantilever tip and the stage surface. With the sample in position, one can “clamp” the velocity, or move the cantilever holder at constant velocity with respect to the surface. However, the AFM tip will alter its speed in response to the tensile reactive force, which can be measured (in terms of cantilever tip deflection) as a function of relative position changes. By varying the velocity and accounting for hydrodynamic forces when the velocity is above a few $\mu\text{m/s}$, one can gain insight into the potential energy barriers along an unfolding trajectory.

The typical stretching experiment stretches an engineered polyprotein composed of tandem repeats of the same domain. This repetition precludes the problem of attributing segments of data to each module. In addition, the length of the protein enables one to ignore any AFM-substrate interactions. This tandem repeat strategy has been successfully used for the alpha-helical domain of spectrin (Rief et al., 1999) as well as the beta-sandwich domains such as fibronectin type III (Oberhauser et al., 1998) and immunoglobulin (Rief et al., 1997). The result of the polyprotein approach on a velocity-clamp experiment results in data that resemble a sawtooth profile as shown in Figure 15.

Figure 15. Typical “sawtooth” profile from a velocity-clamp mechanical unfolding experiment. Each peak can be considered to correspond to an unfolding of a single domain. However, the upward movement of the force is due to the resistance of the entire chain. Hence the Worm-Like Chain model can be used to interpolate the behavior of the protein up to the rupture force, at which point the model breaks down for a set of parameters.



How do sawteeth reflect the physics? The gradual increase in the force is consistent with an interpolation based on the Worm-Like Chain model (Bustamante et al., 1994):

$$F = \left(\frac{k_B T}{P} \right) \left[\frac{1}{4(1-x/L)^2} - \frac{1}{4} + \frac{x}{L} \right]$$

11) F(x), WLC model.

The variable F is force, P is the persistence length (Li et al., 2006) , x is the extension length, and L is the molecular contour length. This equation was derived by drawing an analogy to the quantum-mechanical ground state energy of a dipolar rotator.

The theoretical approach for the velocity-clamp method assumes a constant Hookian spring constant for the cantilever. When constant velocity pulling of the cantilever holder v is combined with the spring constant k of the cantilever itself, the result is a composite term kv , which is a term with units of pN/s. Hence, the constant-velocity AFM approach can be thought of as a force-ramping effect on the specimen.

Evans observed that for a given unfolding configuration and a given force “ramping rate,” the system exhibited a distribution of rupture forces, the most frequent one being termed the “peak” force (as in peak in the probability distribution space, not in

magnitude of force). Hence, one could chart a correlation between peak force and ramping rate as shown in Figure 17 and Figure 18.

Figure 16. Schematic of velocity-clamp experiment data: occurrence vs. force. For a given ramping rate, the rupture force measurements result in a distribution (Li et al., 2006). The fraction of molecules folded is determined by integrating over force. The average rupture force is the corresponding force for the folded fraction. Repeating this over a number of ramping rates would give a plot with which one can solve for $X_{f \rightarrow u}^*$ and $A_{f \rightarrow u}$. (Li et al., 2006)

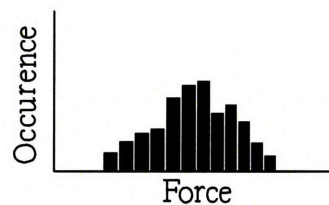


Figure 17. The dynamic strength of mostly covalent and ionic bonds: peak rupture force [pN] vs. ramping rate [pN/s]. From the top, C-O; C-N(green) and C-C(black); Si-O; Si-N; Si-C; Si-Si; S-Au(one data point); DOPA; His₆ Ni-NTA pH 7.2 (inside the box). The box represents approximate area covered in the noncovalent bond strength figure. Lines were derived from data of the following references: His₆ Ni-NTA pH 7.2, (Kienberger et al., 2000); Si-C, S-Au, (Grandbois et al., 1999); C-C, C-N, C-O, Si-C, Si-N, Si-O, Si-Si (DFT), (Beyer, 2000); 3,4-dihydroxy-L-phenylalanine (dopa) (Lee et al., 2006).

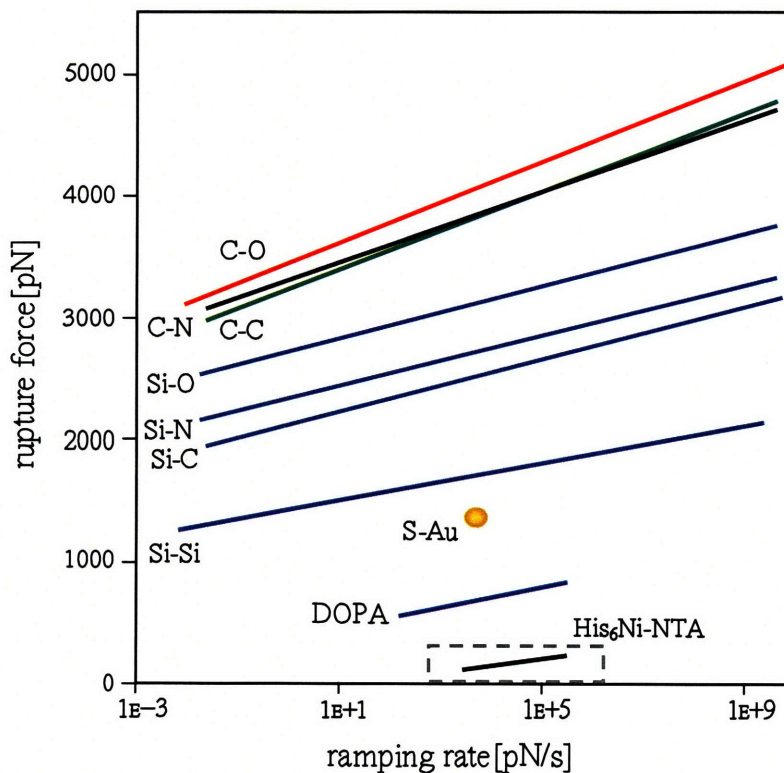
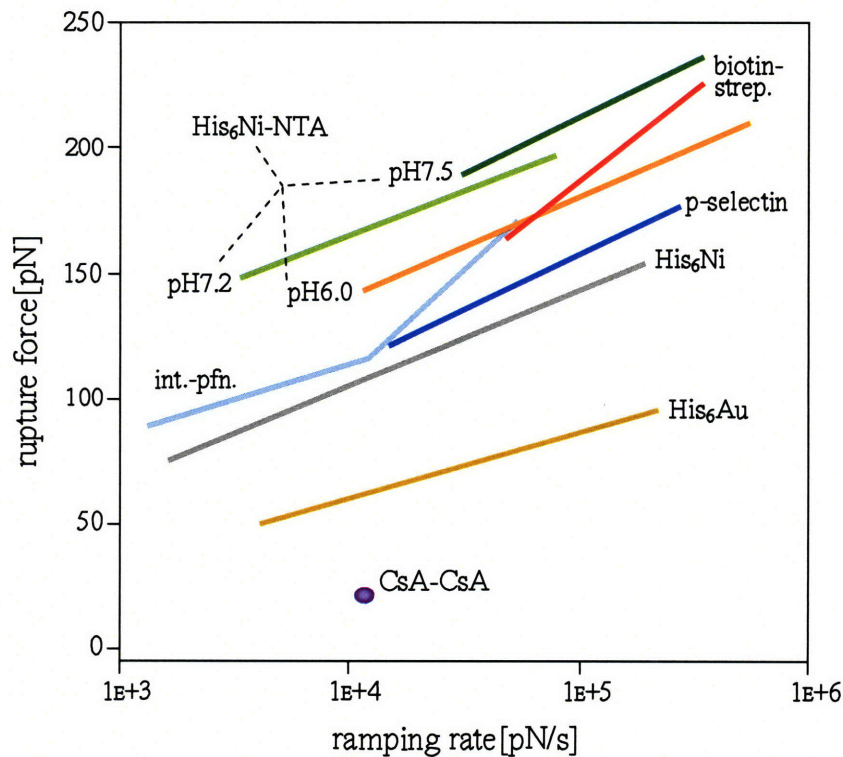


Figure 18. The dynamic strength of noncovalent bonds: peak rupture force [pN] vs. ramping rate [pN/s]. At a ramping rate of 10000 pN/s, histidine tags complexed with Ni-NTA prove to be strongest. Green, green-yellow, and orange represent the His tags at different pH values. In order of decreasing strength at 5E4 pN/s, they are: His₆ Ni-NTA pH 7.5 (green), His₆ Ni-NTA pH 7.2 (green-yellow), and His₆ Ni-NTA pH 6.0 (orange). Red line indicates biotin-streptavidin (pH 7.2), activated $\alpha_5\beta_1$ integrin with plasma fibronectin is indicated by the kinked light blue line. The dark blue represents P-selectin. Non-NTA His tag bonds were weaker than those with NTA.



The grey represents His₆ Ni pH 7.5, and lowest line (gold) represents His₆ Au pH 7.5. The purple dot represents CsA-CsA, a dimerization of the bacterial glycoprotein, contact site A. The noncovalent bonds are located within the previous figure within the area estimated by a box. Lines were derived from data of the following references: His₆ Au pH 7.5, His₆ Ni pH 7.5, His₆ Ni-NTA pH 6.0, His₆ Ni-NTA pH 7.5, (Schmidt et al., 2002); His₆ Ni-NTA pH 7.2, (Kienberger et al., 2000); biotin-streptavidin pH 7.2, (Merkel et al., 1999); activated $\alpha_5\beta_1$ integrin with plasma fibronectin (Li et al., 2003); CsA-CsA (Benoit et al., 2000); P-selectin (Fritz et al., 1998).

Given a two-state system with no discernible intermediate folding steps, and a reaction rate constant with an exponential dependence on the force, one can arrive at (Li et al., 2006; Liphardt et al., 2001) . . . :

$$\ln \left[r \ln \left[\frac{1}{N(F, r)} \right] \right] = \ln \left[\frac{A_{f \rightarrow u}}{(X_{f \rightarrow u}^\ddagger / k_B T)} \right] + (X_{f \rightarrow u}^\ddagger / k_B T) F$$

12) Two-state Markov model for unfolding.

The variable $N(F, r)$ is the fraction of molecules folded given a loading rate r and rupture force F , $X_{f \rightarrow u}^\ddagger$ is the distance from the folded to the transition state, $A_{f \rightarrow u} = k(0)k_m$, $k(0)$ is the rate of unfolding at zero force, k_m accounts for instrumental factors. By plotting the

left side of the equation against rupture force F , one can estimate the distance to the transition state ($X_{f \rightarrow u}^\ddagger$) and the factor $A_{f \rightarrow u}$. These parameters can be used in the equation for $k(f)$, derived above and now reiterated here:

$$k(f) = k_m k_0 \exp\left(\frac{fX^\ddagger}{k_B T}\right)$$

13) Reaction rate constant.

The folding process can also be subject to a similar analysis with the following equation (Li et al., 2006) .:

$$\ln\left[-r \ln\left[\frac{1}{U(F, r)}\right]\right] = \ln\left[\frac{A_{u \rightarrow f}}{(X_{u \rightarrow f}^\ddagger / k_B T)}\right] - (X_{u \rightarrow f}^\ddagger / k_B T)F$$

14) Two-state Markov model for folding.

Again, one can derive the reaction rate constant for the folding process. The folding and unfolding reaction rate constants can then be combined to calculate K_{eq} and ΔG . In this manner, the velocity-clamp data can result in kinetic and thermodynamic data.

Force-clamp method

Although the velocity-clamp method was able to uncover insights into protein dynamics, the stretching force was deemed by some to be too unpredictable to infer the validity of the two-state Markovian folding model in protein folding phenomena. The two-state Markovian folding model is important because it is the assumed model in most spectroscopic determinations of the folding rate constants (Samori et al., 2005) . Verification necessitated a force-clamp approach, which is currently done with optical tweezers (Nambiar et al., 2004) and force-feedback AFM (Oberhauser et al., 2001). By means of a force-clamp AFM with a standard deviation of 2.5pN, the protein ubiquitin was demonstrated to fold and unfold in accord with the commonly presumed Markovian

process (Schlierf et al., 2004). This force-clamp experiment produced the typical extension-time curve depicted in Figure 19. By averaging a sufficient number of these step functions at a given applied load, one can arrive at an exponential function whose time constant corresponds to a particular applied force value.

From previous expressions for $k(f)$ and $k=1/\langle t \rangle$, one can arrive at

$$\ln\left(\frac{1}{\langle t \rangle}\right) = \ln A + F\left(\frac{X^\ddagger}{k_B T}\right)$$

15) First-order reaction model with constant force.

The variable $A=k_m k_0$. Plotting $-\ln\langle t \rangle$ against F , one can use linear regression to arrive at values for A and X^\ddagger .

In addition, the preceding theoretical discussions also imply that

$$K_{eq}(f) = K_{eq}(0)\exp\left(\frac{f\Delta X}{k_B T}\right)$$

16) Equilibrium under force.

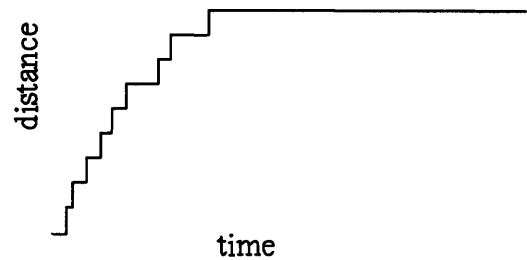
where:

$$\Delta X = X_{u \rightarrow f}^\ddagger + X_{f \rightarrow u}^\ddagger.$$

17) Reaction path length.

These equations can then be used to again arrive at reaction rate constants for folding and unfolding.

Figure 19. Extension-time curve from a force-clamp experiment. Full extension is usually on the order of hundreds of nanometers and ~1 sec.



Therefore, velocity-clamp and force-clamp methods can be used to derive traditional thermodynamic and kinetic property values by means of single molecule experiments.

Details of GFP that affect mechanical and optical response

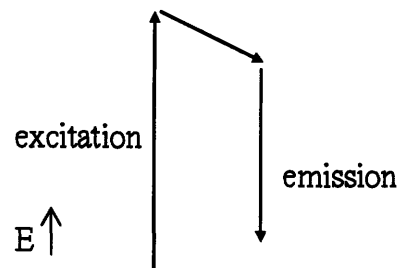
Velocity-clamp and force-clamp approaches are able to characterize a single protein's overall mechanical behavior, but the mechanical response of a protein is linkage-dependent (Carrion-Vazquez et al., 2003). In other words, depending on the trajectory of tension, the anisotropy of a GFP's structure will dictate a different resistance response. Linkage control will allow the tuning of the force sensor. What linkages are available for GFP? Topell et al have conducted permutations of the GFP sequence to determine the viability of moving the N- and C-termini (Topell et al., 1999). These experiments have revealed that 1, 157, 173, and 230 are prospective candidate points for introducing a natural protein binding domain.

Linkage dependency, however, also presents a complication. Each experiment can (usually) only deal with one trajectory at a time, and each additional linkage construct implies additional time and resource requirements. It is desirable to have an efficient means of screening prospective linkages.

These structural effects must be related to fluorescence eventually. Fluorescence, shown schematically in Figure 20, is basically the absorption of photons at one wavelength and the emission of photons at a longer wavelength. In GFP the fluorescence mechanism is but one mode of energy relaxation; nonradiative quenching mechanisms compete with fluorescent light emission. In addition, photobleaching can preclude the possibility of fluorescent emission altogether. Moreover, all fluorescent bodies are

affected by solvent viscosity, ionic concentration, pH, and hydrophobicity. In short, fluorescence has many factors that affect its emission.

Figure 20. Simplified Jablonski diagram. Fluorescence is an excitation of a cold body by one photon, followed by an emission of another photon but at a longer wavelength. It is characterized by extinction coefficient, quantum yield, and fluorescence lifetime.



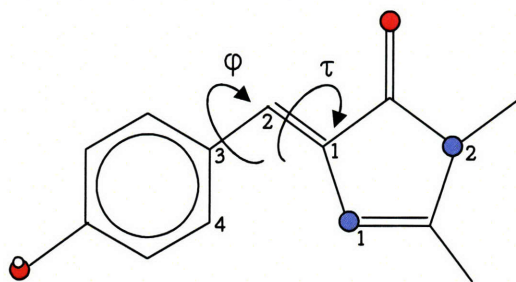
The fluorescent emissions of GFP come from the radiative relaxation of the fluorophore, whose structure can be gleaned from Figure 21. Surrounding this fluorophore is a secondary structure which is necessary for fluorophore performance, as demonstrated by circular dichroism measurements and denaturation studies (Ward and Bokman, 1982) . The model fluorophore in free solution is nonfluorescent (Kummer et al., 2002). This lack of emission activity can be attributed to mechanisms of nonradiative relaxation. First, the surrounding medium can interact and induce solvent quenching, by which the energy of the excited state is transferred away, for example, to a water molecule. Second, the exposed fluorophore could undergo oxygen quenching, which seems to be normally blocked by the secondary structure (Nageswara et al., 1980) ... Third, the fluorophore's internal bonds allow the fluorophore to funnel its excitation energies into generating torque, as shown in Figure 21. One can demonstrate this bond-rotation relaxation mechanism; increasing viscosity by solvent selection and/or temperature decrease results in fluorescence activity (Kummer et al., 2002). In short, the local environment of the fluorophore is affected by proximal amino acids of GFP.

There are a number of examples of subtle alterations of GFP structure that have measurable effects on the fluorescent properties of the GFP fluorophore. Two examples are the variants T203Y and T203H, which have excitation and emission maxima that are

“red-shifted” with respect to the wild-type GFP (Ormö et al., 1996). In a chemical denaturation experiment, prior to loss of fluorescence, GFP has been known to exhibit optically oscillatory behavior (Baldini et al., 2005). In the case of photoactivation, the thr203 residue is thought to alter one hydrogen bond location and glu222 undergoes decarboxylation, removing two oxygens out of a potential hydrogen bonding network (Patterson and Lippincott-Schwartz, 2002). Such electronic structure changes are probably simple enough to occur by means of mechanical tension. While these alterations appear structurally unremarkable, they nevertheless have significant impacts on the energy relationships between different conformations (Creemers et al., 2000b), each having different fluorescence properties. Because the consequent alterations in the relative populations of GFP conformations affect the overall fluorescence response, subtle structural changes should bring about measurable changes in fluorescence.

Figure 21. GFP fluorophore model compound p-hydroxy benzilidene 1,2 dimethyl imidazolinone (HBDI).

In GFP, most of the covalent structure would be from tyr66. The bottom left hydroxy group would form a hydrogen bond bridge to his148 via a single water molecule inside the beta-can. Indicated are the dihedral angles τ ($N_1-C_1-C_2-C_3$) and ϕ ($C_1-C_2-C_3-C_4$). Rotations about the τ and ϕ angles result in four different nonradiative relaxation paths: τ one-bond-flip; ϕ one-bond-flip; positively correlated hula-twist (+HT), where both angles rotate as shown above in the “same” direction; and negatively correlated hula-twist (–HT) where there is simultaneous rotations in opposing directions. Adapted from (Maddalo and Zimmer, 2005).



While the two-state Markovian model has been a useful theoretical framework in the comparison of various stochastic processes, further theoretical development would be needed to comprehend and exploit protein folding phenomena of even greater detail. For example, some protein folding processes can be characterized as a three-step process. The intermediate state has been observed by optical tweezers in ribonuclease H (Cecconi

et al., 2005), inferred from NMR studies in the villin headpiece domain (Grey et al., 2006; Tang et al., 2006), and stabilized by mutagenesis in c-type cytochromes (Borgia et al., 2006). The folding intermediate has also been established in the disease-relevant prion proteins (Apetri et al., 2006; Apetri and Surewicz, 2002). These experimental developments also require theory.

What theories are applicable? The first division of intra-protein motion can be conceptualized as domain motions, where largely cohesive constituents of a single protein move with respect to one another. Gerstein et al categorized these motions as either “hinge” motions in alpha helices, beta strands and beta sheets that are sufficiently free of constraining interactions; or as relatively limited “shear” motions between closely packed polypeptides (Gerstein et al., 1994) . While GFP itself can be considered a single domain, any first-generation fusion chimera would almost certainly involve a loop that can be considered a hinge. In addition, GFP itself will undergo a hinge-like motion in at least one unfolding trajectory (Dietz and Rief, 2004b).

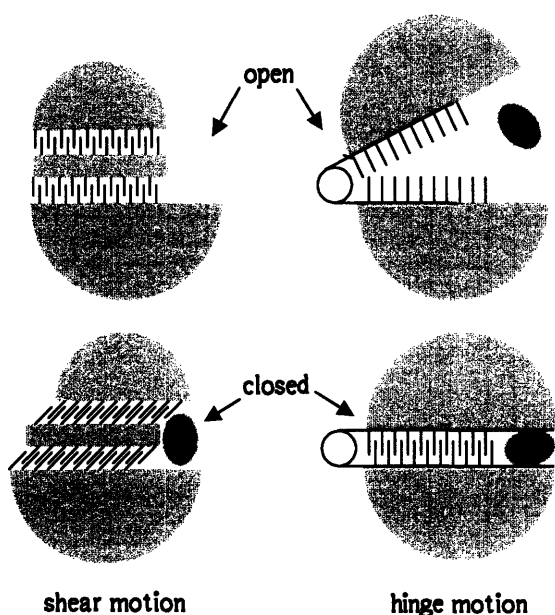


Figure 22. Hinge and shear motions in protein mechanics. Adapted from (Gerstein et al., 1994).

From a much more fundamental perspective, the foundation of protein mechanics is the mechanics of molecules and atoms that have been elucidated through chemistry research. How can one

put together the details of atom-atom interactions to form a larger picture that allows insight into protein mechanics? One approach has been computational chemistry.

Computational chemistry

Computational chemistry comes in two major groups. The more rigorous and accurate simulations depend on quantum mechanics (QM) to provide a solid starting point. However, even with approximations of electron density, this approach is too computationally costly for a great number of molecular inquiries. At least some of these research questions probably do not need the extra precision and accuracy that quantum chemistry can provide over classical mechanics, which provides the foundation for simulations grouped under the term molecular mechanics (MM).

Classical mechanics is a good approximation of quantum mechanics when the quantized energy levels have negligible gaps in between. The gaps are most noticeable at low temperatures where molecules can occupy a much fewer number of discrete states than at room temperature. For example, the harmonic oscillator, which is used to approximate energy potential wells in empirical force fields, exhibits low-temperature discrete energy levels by its ability to accept or emit quantum differences between the energy states. However, these changes in energy state become less distinguishable when the thermal fluctuation energy $k_B T$ is much larger than the quantum transition energy $h\nu$, which is Planck's constant multiplied by frequency.

All molecular mechanics programs have a set of energy functions that are used to calculate the force fields that affect the atoms. In the software "Chemistry at Harvard Molecular Mechanics," (CHARMM), the total energy function is divided into bonded and

non-bonded groups. The bonded energy contribution can be further partitioned into the following:

$$E_{\text{bond}} = \sum k_b (r - r_0)^2$$

18) Bond stretch potential.

$$E_{\theta} = \sum k_{\theta} (\theta - \theta_0)^2$$

19) Angle-bending potential.

$$E_{UB} = \sum K_{UB} (S - S_0)^2$$

20) Urey-Bradley term.

$$E_{\phi} = \sum K_{\phi} [1 + \cos(n\phi - \delta)]$$

21) Dihedral angle potential.

$$E_{\omega} = \sum k_{\omega} (\omega - \omega_0)^2$$

22) Improper dihedral angle potential.

The non-bonded energy functions can also be further classified:

$$E_{elec} = \sum_{i>j} \frac{q_i q_j}{\epsilon r_{ij}}$$

23) Electrostatic energy.

$$E_{vdw} = \sum \epsilon \left[\left(\frac{R_{\text{min},ij}}{r_{ij}} \right)^{12} - \left(\frac{R_{\text{min},ij}}{r_{ij}} \right)^6 \right]$$

24) van der Waals energy.

The way energy contributions are partitioned depends on the software. The variations extend beyond the equations to the data files that contain information on atomic, structural, and interaction data. The Residue Topology File (RTF/TOP) contains atomic information as well as information on the higher-order units called “residues.”

The Parameter file (PRM/PAR) contains interaction data. The Protein Structure File (PSF) is a combination of atomic coordinates files, e.g. a PDB file, with the RTF and PRM files. The basic proposition is that, by extracting interaction data from parts of other molecules, one can use that data to piece together the behavior of a larger system. While these parameter values may differ somewhat depending on the software, the overall simulation behavior is thought to be similar.

The first advantage of MM software over QM software is the allowance to implement a system more amenable to intuition. The capacity for a partitioning style is a subtle advantage over quantum mechanics software, in that one can arrive at an energy contribution structure that can be understood intuitively and implemented in a computationally convenient manner. The second advantage is cost. With these design considerations and approximations, force field methods are able to run faster simulations of a larger set of atoms at a cheaper cost than quantum mechanical simulation systems.

However, quantum mechanical approaches also have their uses in computational chemistry. Whereas molecular mechanics conceives of indivisible atoms and immutable covalent molecular structures, quantum mechanical simulations model molecules that can donate protons and electrons that can absorb photon energies. The ability to model electron transitions is a requirement for computationally studying fluorescent phenomena of the GFP chromophore. Classical CHARMM is not a sufficient description of the photophysics, which requires a quantum mechanical treatment. This dilemma – the necessity to resort to quantum mechanics to model light absorption, and the simultaneous need to operate within the available computational capacity – has led to a composite approach called quantum mechanics/molecular mechanics (QM/MM).

Because quantum chemistry simulations require significantly greater computational power than classical mechanics simulations, groups such as Sinicropi et al have opted for a hybrid quantum mechanics/molecular (classical) mechanics (QM/MM) approach model (Sinicropi et al., 2005). While much of the surrounding beta-can behavior is computed via classical mechanics, the chromophore and nearby atoms are described by quantum mechanics. Such an approach allowed the authors to estimate the photophysics properties of a complete GFP with at most 20 nm of error. This error can be attributed to a number of factors. First, the empirical force field might not be recreating the actual forces in the optical tweezer experiments. Second, the approximation of a hybrid system might not effectively model the interactions between the two regions. Nevertheless, the hybrid model appears to be a promising approach to analyzing the optical tweezer experiment and developing guidelines for using GFP as a force sensor.

Critics of computational methods may state that the approach explores dynamic stability at a regime that does not overlap with AFM and OT. Nevertheless, these simulations have applicability in situations where biological materials undergo high impulse transfers. Where does biology sustain high force? Some possible phenomena may be: the flight of bees and hummingbirds; the entanglement of prey in a spider's web; the woodpecker's habit of noisy tapping on wood; the contraction of *Vorticella*; the acceleration of a cheetah as it begins to chase prey; and the impact of passengers in a car accident. Therefore, exploration of "fast" regimes of unfolding are still relevant in biology. Moreover, protein behavior as a function of linkage and unfolding kinetics can still be examined.

Figure 23. Schematic of force sensor. Mutagenesis and applied load trajectory affect the local hydrogen bond network of the fluorophore. Subtle changes in this noncovalent network alters absorption and emission properties. Nonradiative relaxation can involve solvent quenching and “hula twist” mechanisms.

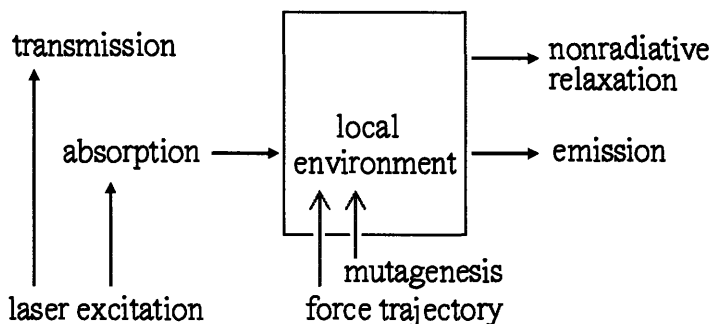


Figure 23 summarizes the context of developing a force sensor. Based on the above considerations, one can ask a number of questions. How does force trajectory configuration affect the response in terms of structure, which affects fluorescence? How would established experimental protocols affect protein internal structure, which affects fluorescence? How are internal structures deemed important for fluorescence affected by overall structural stress?

The first series of simulations examined the effects of pulling trajectory of a system under constant force internal structural changes.

The second series of simulations examined the effect of the ramping rate of force on the GFP internal structure, which was characterized in terms of solvent accessible surface area (SASA). At the C-terminus, residue 230 was constrained, and the N-terminal residue 1 was pulled by a dummy atom at constant velocity. Because of the finite spring constant governing the relationship between the dummy atom and residue 1, the overall effect was expected to be a constant increase in applied load with respect to time. The internal structure characterization was accomplished by the calculation of solvent-accessible surface area for each of the amino acids as well as the fluorophore. In addition, hydrogen bond rupture order was noted for comparison among different

ramping rates. The local environment effect of the beta-can interior was characterized in terms of atom-atom distances.

Parameter	Value
integration timestep	0.001 ps
constrained residue	230
constraint method	harmonic weighting
pulled residue	1
velocity	0.1, 1, and 10 Å/ps
pre-spring constant value	0.01987 kcal/(mol Å ² K)
T (for spring constant calculation only)	310
kmin, kmax	0.01987x310 kcal/(mol Å ²)
rmin, rmax	5Å
fmax	3000pN

The surroundings of the fluorophore present possible hydrogen-bonding partners with which the fluorescence properties of the protein can be improved. How well the surrounding hydrogen bond network can withstand strain is not known. Hydrogen bonding is expected to occur as indicated in Table 2. The indicated atoms are represented by red triangles in Figure 25, to put the hydrogen bond network in context of the GFP structure.

Table 2. Hydrogen bonding partner-candidates for the fluorophore.

Candidate	Fluorophore partner	Selection text for candidate
his148's unprotonated N	tyr66	resid 148
146's oxygen	tyr66	resid 146
ser205's oxygen	tyr66	resid 205
glu222's O	ser66 alpha carbon	resid 222
arg96's amine	tyr66's carbonyl oxygen	resid 96
asn94's N	tyr66's carbonyl oxygen	resid 94
ser205's O	tyr66's O	resid 205

Note: some of these interactions may require an water molecule "bridge."

Many of the amino acid pairs in Table 2 connect with each other through a water bridge. To determine the water bridge's existence at a given time point in a simulation requires water molecules, which were not included for most of the simulations. Therefore, the

beginning of a near-equilibrium simulation (0.001Å/ps) which had water molecules was observed for possible surrogate measurements. On the side of the fluorophore with Y66 hydroxy group, estimations at cutoff values of 3Å and 35° revealed a hydrogen bond network of one water molecule and four non-hydrogen protein atoms. The Y66 hydroxy group bonded with a water residue which connected with H148 backbone amine, N146 carbonyl oxygen, and S205 hydroxy oxygen. Occasionally the hydroxy oxygens of Y66 and S205 bonded without a water intermediate. On the timescale of the simulation these hydrogen bonds were intermittent, usually having one to two bonds and up to three bonds total. These hydrogen bonds were intermittent on the timescale of the simulation. Measurement of the distances over 400 frames resulted in characteristic distances between the relevant protein atoms, as shown in Table 3. These distances were used as surrogate measures of hydrogen bonding.

Table 3. Characteristic distances within a fluorophore hydrogen bond network.

	Atom 1	Atom 2	Average±SD[Å]
a	Y66 hydroxy oxygen	N146 carbonyl oxygen	5.06±0.21
b	Y66 hydroxy oxygen	H148 backbone amine	5.27±0.17
c	Y66 hydroxy oxygen	S205 hydroxy oxygen	2.92±0.18

A graphical perspective is provided in Figure 24.

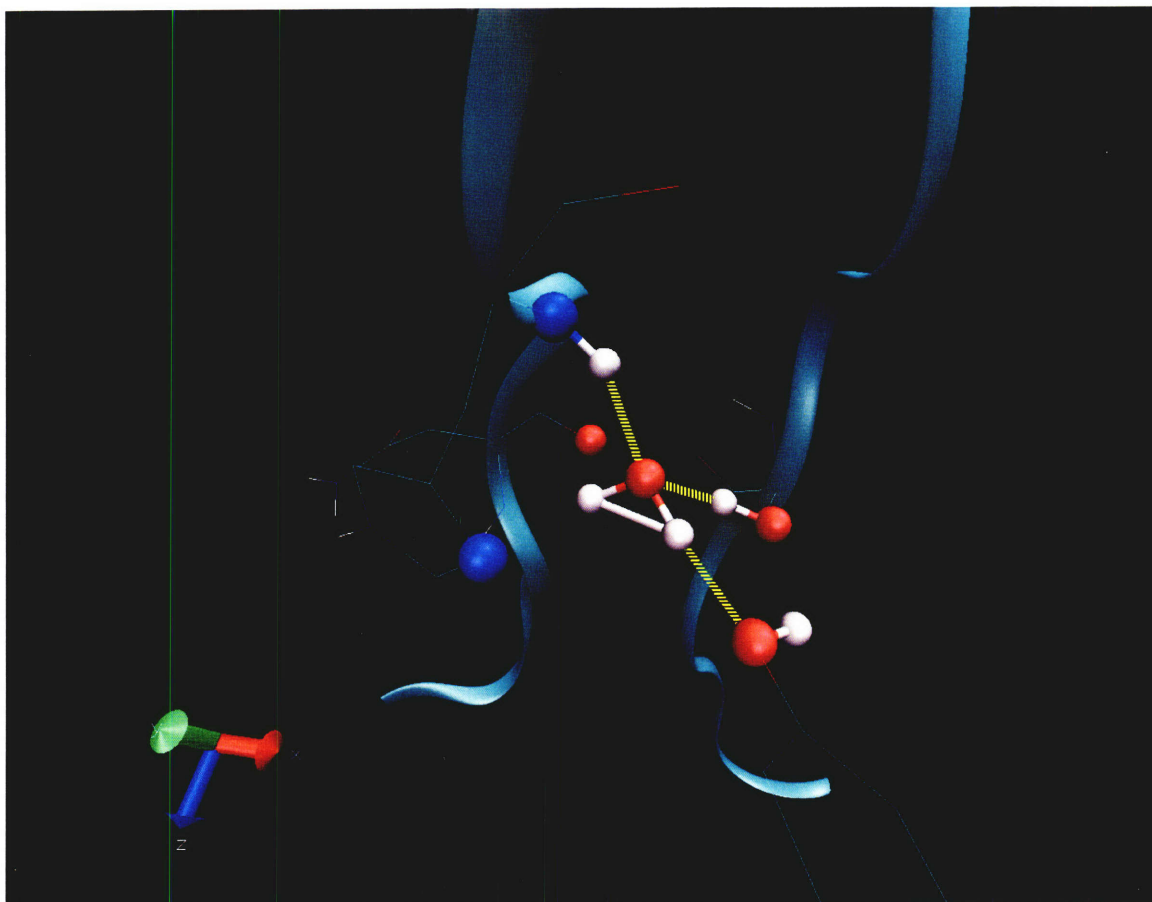


Figure 24. GFP hydrogen bond network schematic near Y66 and H148. This snapshot indicates the arrangement of three hydrogen bonds (yellow), which occur as a result of a bridging water molecule. Such networks are believed to stabilize the fluorophore against the non-radiative, “hula-twist” relaxation that decreases the quantum yield. The cylinder at the side indicates the orientation of the molecule.

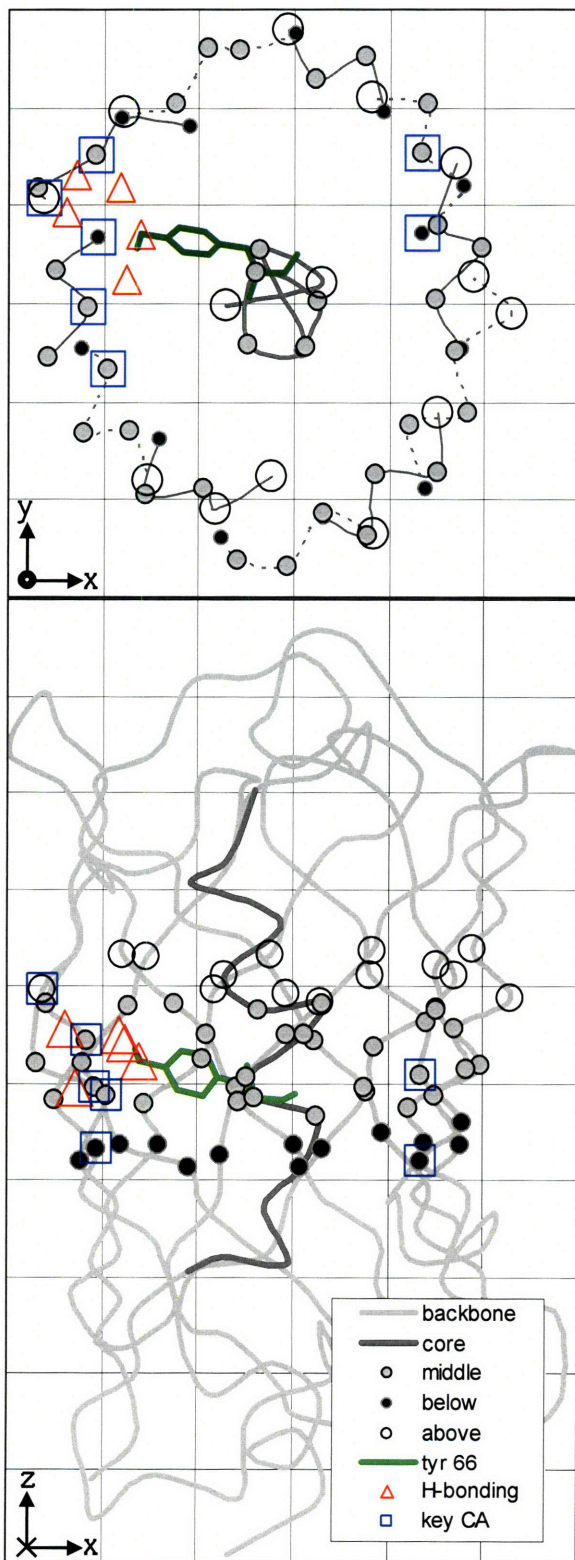


Figure 25. GFP structure schematic. An equilibrated conformation was positioned according to the major axes of the molecule. The xy-schematic (a) shows a view with the z-axis point out from the page. The xz-schematic shows a view with the y-axis pointing into the page. Gridlines were preserved at 5Å intervals, since there is no concern for data interpretation bias.

Markers. "Middle" points represent all alpha carbons whose elevation (z) was, in relation to atom 588 (Y66 hydroxy oxygen), within 3Å (the cutoff value for hydrogen bond estimation). All alpha carbons 3 to 6Å above atom 588 were labeled with open circles, and all alpha carbons 3 to 6Å below atom 588 were labeled with solid black circles. Blue squares represent alpha carbons of key residues in the fluorophore hydrogen bond network. Red triangles represent hydrogen donors or acceptors on the Y66 side of the fluorophore.

Lines. In (a), lines connect alpha carbons within the same beta strand, or the "core" backbone. In (b), "core" and "backbone" represent approximate backbone pathway for core and non-core residues, respectively. In both (a) and (b), green outline represents Y66 position.

Results and Discussion

The Results and Discussion sections were integrated in this chapter, because computer simulation and subsequent analysis do not have a clear line of demarcation.

Force-clamp studies

GFP was modeled in CHARMM with segment A from 1GFL.pdb. One residue was constrained in position, and another residue was pulled at constant force along a vector from the former to the latter. The constant force was 100pN, and each simulation was run for 50ps.

Constrained Residue	Pulled Residue	Exposure of Fluorophore
001	157	Exposure at 6ps
001	173	Little if any
001	230	Exposure is transient
157	230	Little if any
173	230	Exposure at 25ps
157	173	not tested

157-173 was not tested because there is only one beta strand connecting them, so it would be difficult to determine if the fluorophore had any solvent accessible surface area.

Depending on the linkage, the fluorophore's exposure time and duration changed. In other words, the choices made in the placement of load-bearing attachment moieties will present an opportunity to tune the protein's mechanical response to one's preferences. While these results presented a qualitative manner of understanding GFP unfolding, more detailed analyses are needed to employ the full power of simulation data. Approaches were explored in velocity-clamp studies presented next.

Velocity-Clamp studies

The C-terminal residue T230 was constrained and A001 was pulled on a trajectory pointing away from T230 at the end of the equilibration steps. The three velocity-clamp simulations, at 10, 1, and 0.1 Å/ps, produced dynamic coordinate data. Data was captured every 0.1 ps for 700 Å, but only 700 frames were used for each velocity because the additional level of detail was not necessary for subsequent analyses. The solvent accessible surface area (SASA) was calculated with the software VMD for the fluorophore and each amino acid (Humphrey et al., 1996). SASA data for the fluorophore was plotted against extension distance between the alpha carbons of A001 and T230.

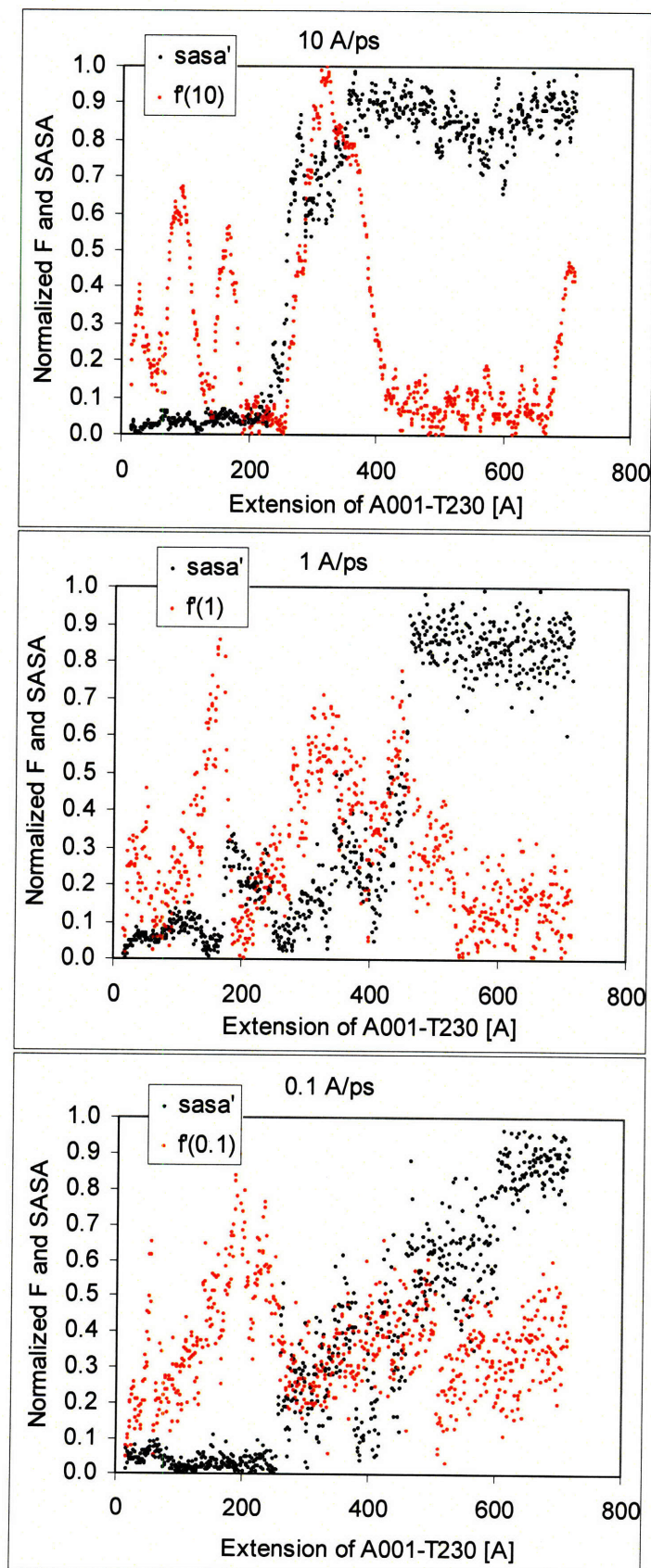


Figure 26. Comparison of force and solvent-accessible surface area for velocity-clamp simulations. Force and SASA were normalized against their respective maximum values within each simulation. (a) 10Å/ps; (b) 1Å/ps; (c) 0.1Å/ps.

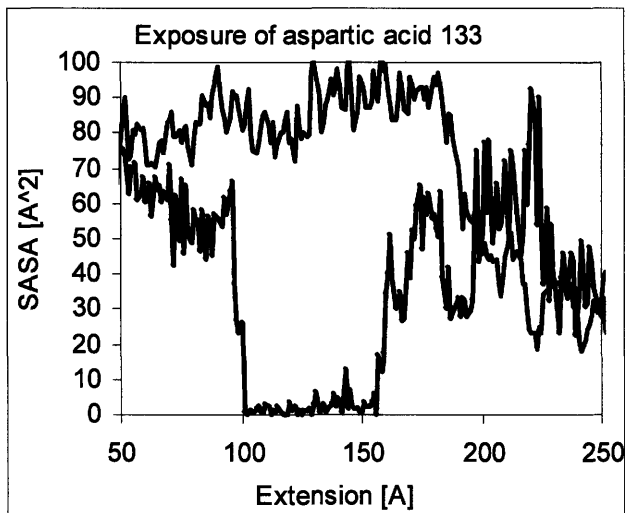
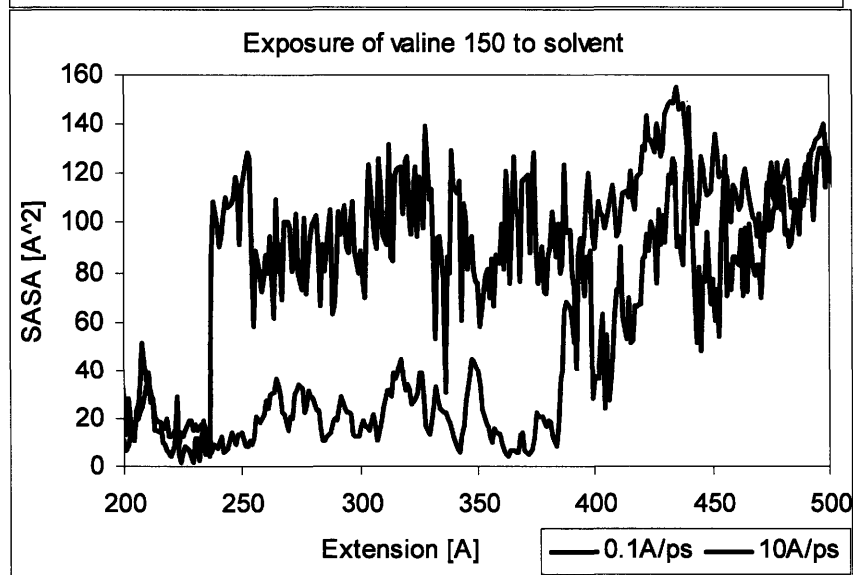
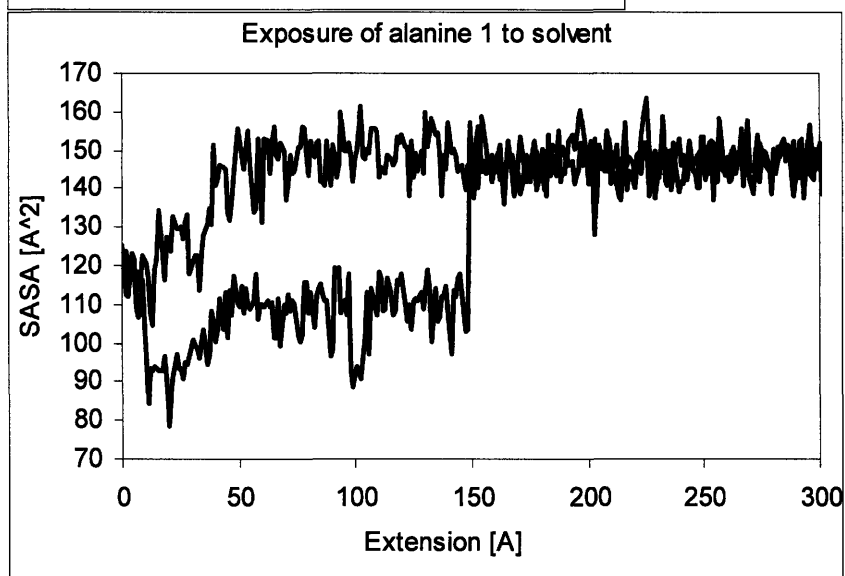


Figure 27 Abrupt SASA changes for individual amino acids, SASA[\AA^2] vs. extension [0.1 \AA]. The dummy atom was moved at a constant velocity of 10 $\text{\AA}/\text{ps}$ (50% gray) or 0.1 $\text{\AA}/\text{ps}$ (black): (a) asp133 is part of a flexible, 15-residue loop; (b) ala1, whose alpha carbon was connected to the constant-velocity pulling dummy “atom” in a harmonic potential, lost a hydrogen bond at about 15 \AA of extension in the slow unfolding case; (c) val150, part of the beta-sheet structure, abruptly acquired solvation $\sim 24\text{\AA}$ of extension.



The fluorophore SASA data are compared against force data in Figure 26. Both figures 2(a) and 2(b) show that an SASA increase is associated with a rise in force. In contrast, figure 2(c) has an SASA increase that is more gradual. This suggests that at lower velocities, the fluorophore's hydrophobic property contributes to a lesser degree in resisting the applied load. The clear rises in force seen at various points in all three F sufficiently stable to mount a reactive force against the overall unfolding. The differences in the locations of the peaks of force suggest that the pulling velocity is sufficiently fast to prevent relaxation mechanisms that would have dispersed the strain in particular parts of the structure. The gradual increase in the fluorophore SASA in 2(c) suggests that relaxation disperses energy to make gradual changes in an upward direction. However, an examination of individual amino acid SASA profiles shows that decreasing velocity does not necessarily result in smoother changes. As shown in Figure 27(b), it is the high-velocity unfolding that results in a relatively smoother SASA increase profile. The abrupt SASA changes appeared to be at least as common in the low velocity simulation in comparison to the high velocity system. This seems to reflect the fact that at low velocities, smooth overall changes occur because of the opportunity for constituents to exchange greater amounts of energy than in the high velocity case. Moreover, the variance of SASA for a given amino acid seemed to be slightly greater for the low velocity case than for the high velocity case; this is also in accord with the expectation that the low velocity case allows an amino acid more time to explore its conformational space.

Complementing the measurement of solvent-accessible surface area is the accounting of hydrogen bonds, especially in the between the strands for the beta sheet.

Whereas solvent-accessible surface area is an indirect measure of the loss of cohesive non-covalent bonds between water molecules (so that they can occupy relatively high energy states of interaction with nonpolar protein parts), the alteration of intra-protein hydrogen bonds is an exchange of “native” bonding partners with uncommon ones, e.g. the surrounding water molecules. An accepted method of counting hydrogen bonds is to consider all donor-acceptor pairs that are less than 3.5 Å apart with a hydrogen-nitrogen-oxygen angle of 35° or less (Paramore et al., 2005). The beta strands of the beta-can were defined according to Table 4.

Table 4. Beta strand details.

Name	Strand	Neighbors
A	011VVPILVELDGDVN023	F*A>B
B	026KFSVSGEGEGDAT038	A>B>C
C	040GKLTCLKFIC048	B>C_K
D	090EGYVQERTIFFK101	I_D>E
E	103DGNYKTRAEVKF114	D>E>F
F	118TLVNRIELKGI128	E>F*A
G	143YNYNSHNVYIMA154	J_G>H
H	160GIKVNFLIRHNI171	G>H>I
I	175SVNLADHYQQNTPII188	H>I_D
J	197DNHYLSTQSALSKD210	G_J>K
K	215RDHMLLEFVTAAG228	J>K C

Notes: *, the only parallel strand-strand orientation; >, left strand connects to right strand with a loop, and left strand is toward N terminus and right strand is toward C terminus; _, left and right strands are not connected on either end of the beta-can; numbering of amino acids starts from 1 and ends on 230. In contrast, VMD numbering by “resid” starts on 0.

The figure shows that hydrogen bond loss does not correlate with pulling velocity. For example, the 10Å/ps, high velocity simulation that seems to undergo longer extensions (than the 0.1Å/ps, low velocity simulation) before the potential for a single-

water bridge disappears. In contrast to the high and low velocity simulations, the 1Å/ps, medium velocity indicates decrease of distances between Y66-N146 and Y-66-H148. This similarity in pattern between the two distances isn't surprising in light of the proximity of H148 and N146 to each other on the backbone. What is interesting is that molecular dynamics demonstrates a geometric basis for potential nonlinear behavior with respect to pulling velocity.

The other observation relates to the question of the relationship between applied load and fluorescence response. The fluorescence of GFP should go down noticeably in quantum yield even at applied loads of 30 to 40 pN, which covers the range of forces measured for the low velocity simulation in the first 200Å of extension. The unfolding of GFP that is equivalent to 200Å of extension should eliminate the hydrogen bonding network at a critical part of the fluorophore. Consequently, the destabilized fluorophore's increase in degrees of freedom would allow it to undergo the nonradiative "hula-twist" relaxation with greater ease. With the relative decrease in propensity for radiative energy release, the quantum yield of the protein should decrease.

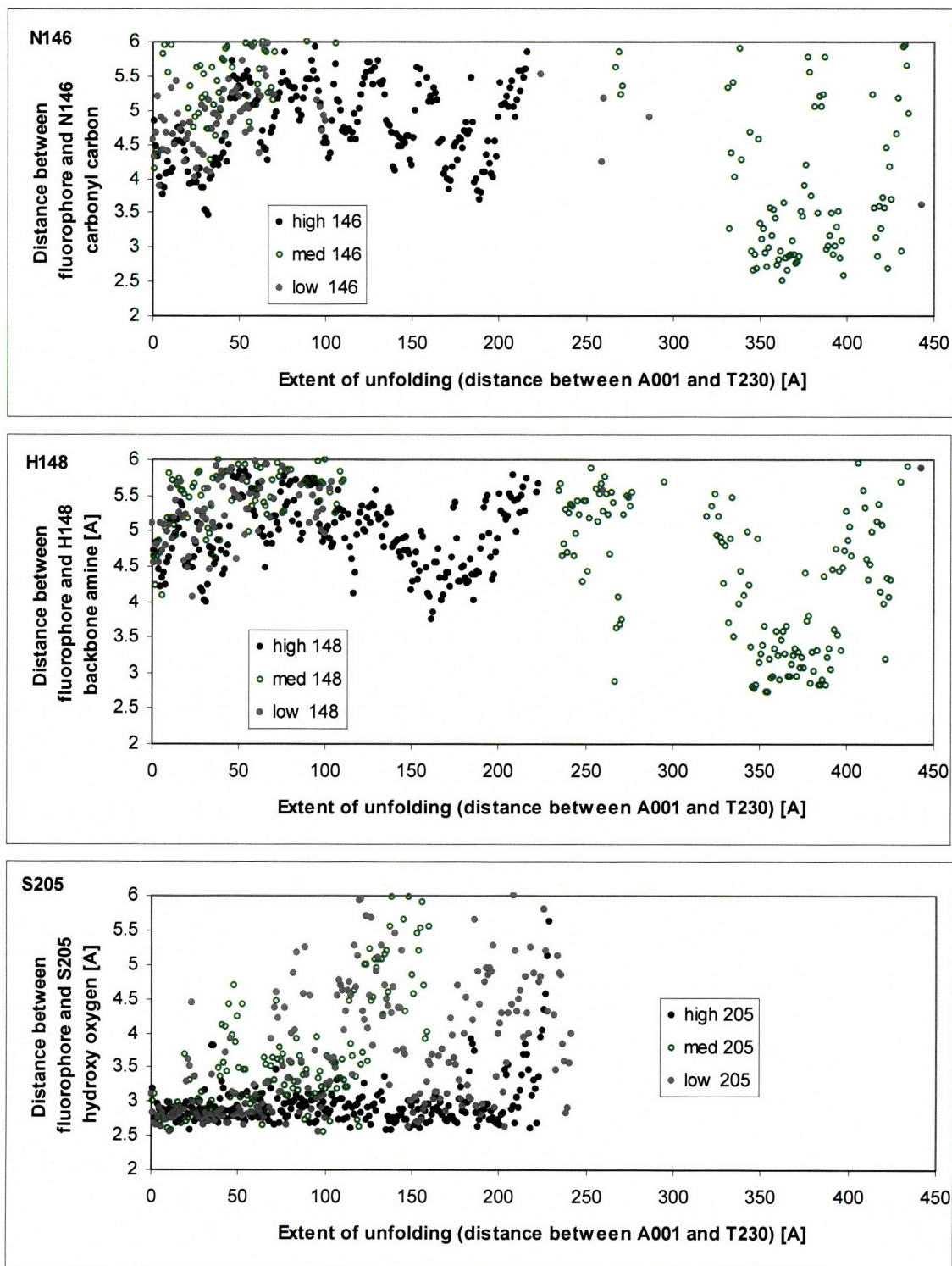


Figure 28. Hydrogen bond network dimensions as a function of unfolding extension. Unfolding extension was the distance between A001 and T230 [Å]. All distances were measured from the Y66 hydroxy oxygen. (N146) Distance to N146 carbonyl carbon. (H148) Distance to H148 backbone amine. (S205) Distance to S205 hydroxy oxygen.

While fluorophore stabilization is presumed to require water molecule bridges, secondary structures such as beta sheets and alpha helices can be analyzed without resorting to indirect measurements. The total number of hydrogen bonds for the GFP molecule was calculated at a 3Å, 35° cutoff. A comparison of three different unfolding velocities in Figure 29 indicates that, the total number of hydrogen bonds is independent of the pulling velocity.

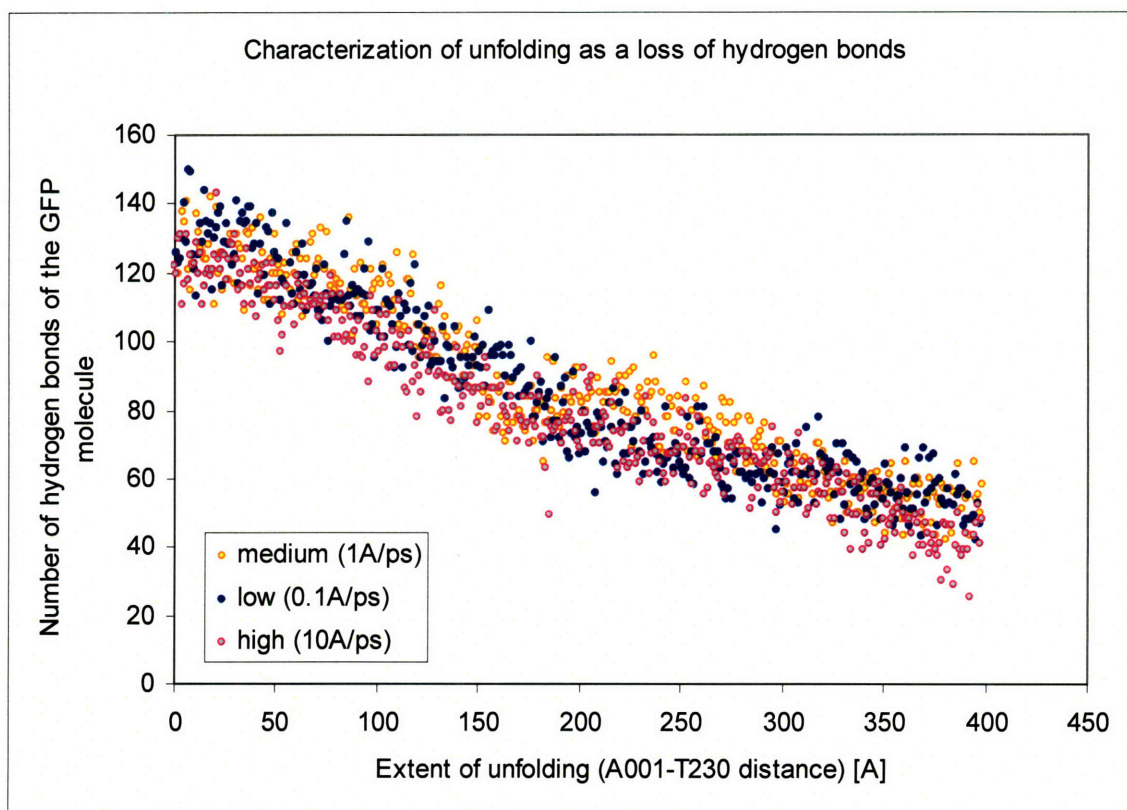


Figure 29. Total number of hydrogen bonds vs. A001-T230 extension length [Å]. The overall hydrogen bond loss profile looks quite similar even when unfolding velocity is altered by two orders of magnitude.

However, the composition of the hydrogen bond relationships are changing, as shown in Figure 30. With extension, the fraction of total hydrogen bonds that occur between former inter-strand beta sheet spaces decrease. In other words, underneath the appearance of gradual change there are multiple relaxation mechanisms whose participation depends on the timescale dictated by the overall unfolding mechanism. To

analyze the details that change as a result of a change in unfolding velocity, separate pairs of beta strands were examined. However, the energy changes afforded by just several hydrogen bonds were too low and susceptible to the degradation of data as a result of thermal fluctuations (data not shown). Qualitatively however, it was possible to see that a decrease in velocity made hydrogen bond loss a more homogeneous decay process; in other words, exchanges of hydrogen bond energies between parts of the beta sheet was taking place at the timescale comparable to the unfolding simulation.

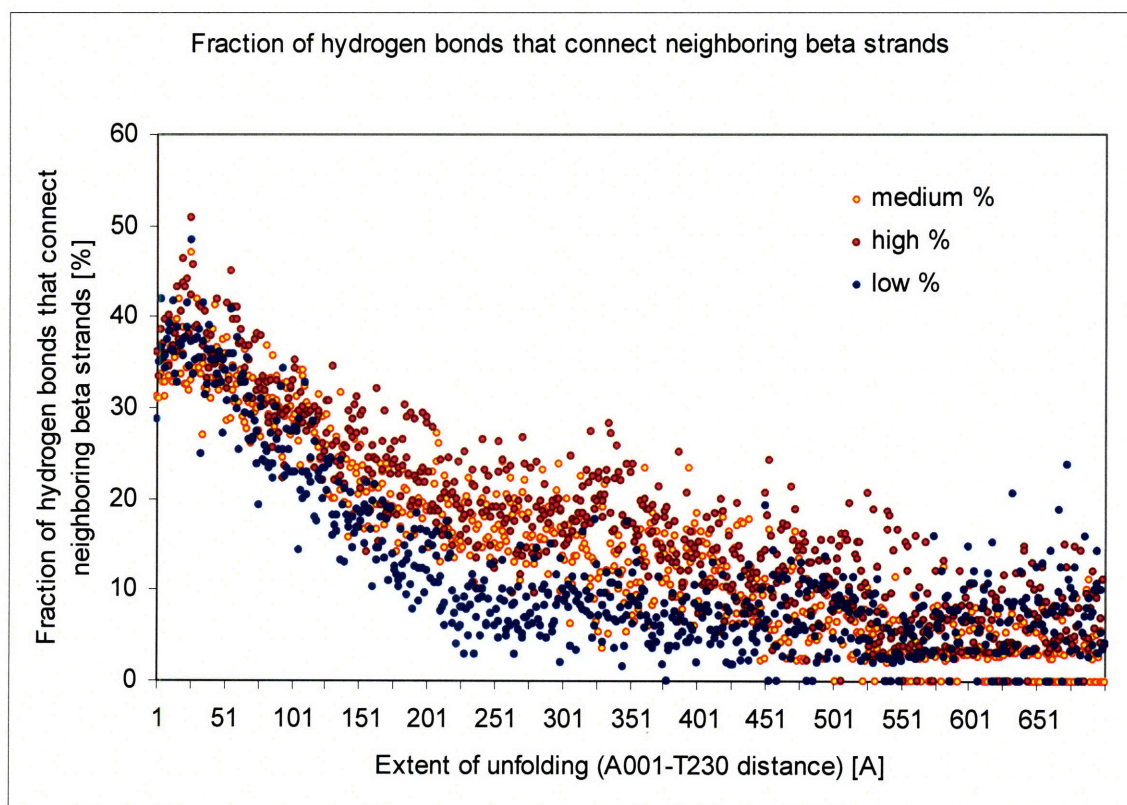


Figure 30. Percentage of preserved inter-beta strand hydrogen bond relationships vs. A001-T230 extension length [Å]. Even though overall hydrogen bond loss profiles change in negligible amounts under different unfolding rates, the composition of hydrogen bonds are different when unfolding rate is altered.

The above simulations allows one to see an emerging theme. When relaxation processes are suppressed by faster unfolding processes, the overall system undergoes sudden changes in properties such as resistance, while constituents undergo more gradual

changes at states relatively dissimilar to neighbors. When relaxation is allowed to occur, constituent systems can undergo greater changes in energy. But properties such as SASA are allowed to increase in a more gradual manner.

The above analyses can be used in subsequent inquiries. For example, molecular dynamics approaches are thought to approximate only “fast” web lab experiments. However, data above clearly show that there are instances where the intraprotein properties indicate a similar behavior between two velocities. This implies that certain segments will behave quite similarly within a velocity range spanning over a magnitude. Exploring the details of why two different velocities result in similar behavior might allow one to make structure-based predictions on which behaviors would be the same regardless of velocity (within a range) and hence approximate that segment of unfolding by a very fast, less costly simulation.

Summary

The theories covering two-state unfolding models and their connection to experimental methods were explored. Noting the need for structural characterization for fluorescence and the lack of resolution in present techniques in AFM and OT, concepts and background for computational methods were presented. The first set of computational methods demonstrated that linkage dependency was clearly seen in the unfolding of green fluorescent protein. The second set of computational methods explored the structural details of green fluorescent protein’s unfolding process. Molecular dynamics offers a way to study the differences between different fluorescent responses that are too subtle in structural differences to be analyzed by single molecule experiments alone. It was found

that the force required for fluorescence may be much lower than the force needed for unfolding according to the two-state Markovian model.

Methods

The starting point of the GFP simulations was downloaded from the RCSB Protein Data Bank. Segment A of the pdb file 1GFL was extracted(Ormö et al., 1996). The usual practice of minimization, heating, and equilibration was done in the CHARMM 19 implicit solvent environment. The segment was converted into a psf format by CHARMM. Then the minimization algorithm was run for 1000 cycles of Newton-Raphson minimization. Heating was done via the Leapfrog Verlet time integration at 1 fs for 1000 steps. Final target temperature was set at 310 K (with ± 10 K allowance), with a temperature increment of 5K every 20 steps. Equilibration occurred under Leapfrog Verlet integration at 1fs.

Chapter 3. The application of shear forces on GFP

Background

Applying and measuring forces

Questions concerning cell and molecular mechanics have been addressed by a variety of approaches (see Table 5). The mechanical behavior of cells can be studied in aggregate on a surface, characterized in terms of individual cells, or measured at different subcellular locations on a single cell (Bao and Suresh, 2003). Atomic Force Microscopy (AFM) methods can measure a cell's stiffness by making force-indentation measurements at a transverse spatial resolution of 1-3 nm and a temporal resolution of 60-100 μ s. The magnetic twisting stimulator (MTS) can produce a specific torque of 0.5 dyn cm² / gauss on beads that could be internalized by cells (Chen et al., 2001). The optical tweezer uses a laser to manipulate a bead (Choquet et al., 1997). Micropipet aspiration had been used to measure viscosity and cortical tension in granulocytes (Evans and Yeung, 1989). Substrate stiffness has been shown to direct stem cell fate (Engler et al., 2006; Even-Ram et al., 2006), correlate with cardiovascular events (Laurent et al., 2005), and stimulate cells according to cell type (Discher et al., 2005). Fluid shear stresses have been used to study vascular endothelial cell behavior (Dewey et al., 1981), and characterize gene expression in blood vessels (Lehoux and Tedgui, 2003).

Table 5. Experimental techniques for studying mechanical interactions with living cells.

<i>Mechanical inputs into cells</i>	<i>Mechanical outputs from cells</i>
atomic force microscopy	ligand-patterned soft membrane
magnetic bead twisting rheometry	vertical cantilevers
micropipette aspiration	thin silicon rubber surfaces
optically-manipulated silicon beads	
flow-induced shear	
substrate stretching	

Cellular response to mechanical inputs have been addressed by the above methods, but what about the characterization of cellular mechanical outputs? An early visualization technique was a thin ($\sim 1\mu\text{m}$), silicon rubber surface was seeded with cells. These cells adhered to and contracted the surrounding substrate. The wrinkles allowed cellular contractile forces to be visualized on silicon rubber (Harris et al., 1980). Using the wrinkles to arrive at intrinsic cell property values proved difficult, however, and quantification required a different approach. One such method was a micromachined set of vertical cantilevers, whose displacement could be used to calculate cell-imposed loads on the environment (Galbraith and Sheetz, 1997). In another example, fluorescent beads were placed in polyacrylamide to measure the forces that the cells were experiencing (Pelham and Wang, 1999).

Just as cells can be described in terms of mechanical properties, the extracellular matrix (ECM) is also amenable to mechanical characterization (Silver and Bradica, 2002; Silver et al., 2003a). ECM tension, which comes about during development, is a normal physiological characteristic that decreases with age. However, lack of use or abuse can result in changes similar to that in the aging process (Edgerton and Roy, 1994;

Fujisawa et al., 1999). The matrix serves to distribute external loads across entire tissues.

The emerging view of cellular and molecular mechanics, is that mechanical transmission of information can go both ways in cells and subcellular structures. To tackle this complex network of communication, it may be possible to adjust the beads-in-polyacrylamide technique so that GFP is the mechanosensor. In this manner, the polyacrylamide system can be used as a testing ground for mechanical sensors before incorporation into a cell line. In that case, how can GFP be incorporated into the gel to bear loads?

Polyacrylamide as a transducer of force to GFP

Force would entail a deformation in polyacrylamide and other hydrogels. When a hydrogel is deformed, alterations in the microstructure occur. Ideally, these microstructural changes would impose a stress on gel-incorporated green fluorescent proteins. The proteins would then respond by a partial denaturation that could be detected by fluorescence microscopy. To achieve a link between mechanical input and fluorescent output, one must characterize and tune each part to play its role.

But why polyacrylamide? Polyacrylamide is relatively inert to protein adsorption (Doherty et al., 2003), and the attachment of proteins is a prerequisite for cellular adhesion. Adhesion-dependent cells placed in an environment without sufficient attachment opportunities would normally undergo apoptosis (Aoshiba et al., 1997; Rozzo et al., 1997; Scott et al., 1997). However, cells are able to survive when they can adhere to cell adhesion factors, which are often micropatterned onto the otherwise inert surface

(Falconnet et al., 2006). In short, the use of polyacrylamide combined with cell-friendly substrates allows a degree of control over how cells will pull on its surroundings.

How does the polymer respond to shear stress? To address questions of shear stress, the traditional approach is to employ two idealizations of materials: the Hookean solid and the Newtonian fluid. The Hookean solid is a perfectly elastic material that whose stress and shear are proportionally related by a constant shear modulus G :

$$\sigma = G\varepsilon$$

25) Shear modulus.

The Newtonian fluid is approximately a material that deforms at a rate proportional to the applied stress. The proportionality constant is viscosity η :

$$\sigma = \eta\gamma = \eta \frac{d\varepsilon}{dt}$$

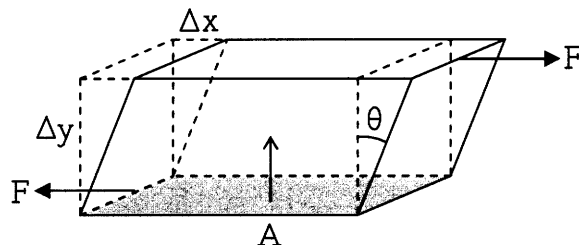
26) Viscosity.

where γ is the shear rate. In comparison, a real material can be regarded as a combination of these idealizations – a viscoelastic mass that has a time-dependent response to an applied shear stress.

Upon the application of shear stress, a viscoelastic material may respond quickly in an elastic manner, but the viscous flow might appear over a relatively long time. When one can describe the behavior with an equation that requires a characteristic time constant, that value can be thought of as the relaxation time. The relaxation time gives an approximate duration that separates the elastic, solid behavior from the viscous, liquid behavior. When the applied stress is longer than the relaxation time, a viscoelastic material will respond in a fluid manner. On the other hand, for stress durations less than

the relaxation time, the object can be better modeled as an elastic solid than a liquid (Jones, RA Soft Condensed Materials pp10-13; very good explanations).

Figure 31. Shear stress ($\sigma=F/A$) and shear strain ($\epsilon=\Delta x/\Delta y$). The block is deformed by force F , for every area A . The shear stress is $\sigma=F/A$. The shear strain is $\epsilon=\Delta x/\Delta y$.



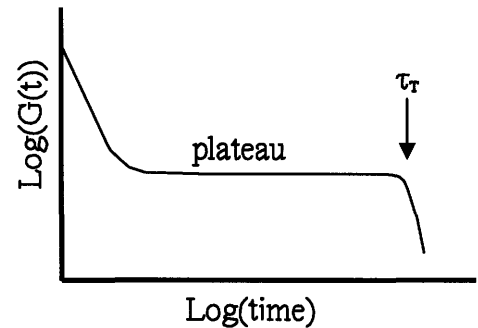
A polymer's structure, however, is rather different from non-polymeric viscoelastic materials. Unlike other viscoelastic materials, polymers have a distribution of molecules of different lengths, and each molecule is usually much longer than any molecule of a nonpolymeric mass. In order to deal with this additional complexity, a number of models have been developed.

A qualitative description of polymer deformation classifies the response to a mechanical load into three major groups – macroscopic cleavage, mechanocracking, and mechanoactivation. Mechanoactivation includes noncovalent bond rearrangements and deformation. Mechanocracking is the production of new surface area as a result of covalent bond rupture. Macroscopic cleavage is the accumulation of mechanocracking.

When stress is imposed, the polymeric material undergoes strain as it accumulates energy. This energy drives relaxation processes, such as the disentanglement of chains, and the rupture of covalent bonds to form radicals. A broken bond at a given site implies a greater share of the applied load for neighboring bonds, and this will increase the likelihood that bonds near the rupture site will break themselves. With the accumulation of scission, a new surface develops the site into a crack, which may grow to the size of a macroscopic cleavage (Vasiliu, 2001).

Macroscopic cleavage development at the level of chain resolution defies a cognitively compact, numerical characterization. However, characterization of viscoelastic behavior of polymers can be achieved at a macroscopic level. For example, the creep compliance, $J(t)$, is dynamic strain normalized by the constant stress applied as a step function at $t=0$, i.e. $\epsilon(t)=\sigma_0 J(t)$. Similarly, the stress relaxation modulus $G(t)$ is the dynamic stress normalized by the constant strain applied as a step function at $t=0$, i.e. $\sigma(t)=\epsilon_0 G(t)$. When $G(t)$ is measured for fairly monodisperse polymers, the resulting profile resembles that of Figure 32.

Figure 32. Schematic of $G(t)$ for a monodisperse linear polymer melt. The stress relaxation modulus $G(t)$ reaches a plateau modulus, which is independent of degree of polymerization. However, chain length *does* influence the termination time: $\tau_T \sim N^{3.4}$.



Another important characterization process is oscillatory deformation, included here for completeness. The input is usually an oscillatory strain $e(t) = e_0 \cos(\omega t)$. The resulting stress data are fit to the formula $\sigma(t) = e_0 [G'(\omega) \cos(\omega t) - G''(\omega) \sin(\omega t)]$, where the complex modulus is $G^*(\omega)=G'(\omega)+iG''(\omega)$. The elastic nature of the material is estimated by the storage modulus $G'(\omega)$, the real component. The viscous aspects are described by the loss modulus $G''(\omega)$, the imaginary part. The phase angle of the response δ is defined by $\tan \delta = G''/G'$. Whether or not these parameters have captured any significant physics might be gleaned from the fact that the complex and stress relaxation moduli are related by:

$$G^*(\omega) = i\omega \int_0^{\infty} \exp(-i\omega t) G(t) dt$$

27) Complex and stress relaxation moduli.

When experiments are conducted under linear viscoelastic conditions, the combination of the above parameters, the Boltzmann superposition principle and time-temperature superposition approach can describe the behavior of polymer shearing. However, it is very easy to exceed the regime of linearity. This departure from straightforward characterization is not surprising, since the above discussion does not explicitly account for key aspects of polymer structure, such as entanglements.

The problem of characterization in the presence of entanglements has been addressed somewhat by the tube model of reptating chains (Doi and Edwards). When the polymer chain is entangled sufficiently by its peers, it cannot move “sideways” because crossing another polymer chain is forbidden. However, it can undergo a linear type of motion along the tortuous tube-like space that it occupies; this is called reptation.

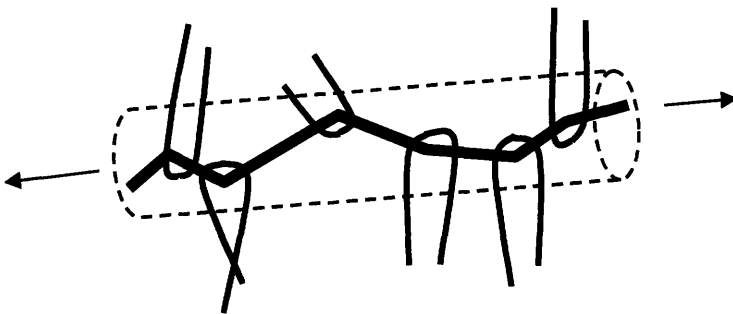


Figure 33. Reptation of a polymer chain. Entanglements along a chain restricts its motion along a virtual tube.

If one approximates the resistance experienced by each segment as a viscous drag, then one can define a drag coefficient ξ_{segment} for each segment. If N segments make up one chain, then $\xi_{\text{chain}} = N \xi_{\text{segment}}$. One can employ this drag coefficient if one assumes that the chain moves along the tube in a diffusive manner, so that the Einstein formula ($D =$

$k_B T / \xi$) can be adapted: $D_{\text{chain}} = k_B T / \xi_{\text{chain}} = k_B T / N \xi_{\text{segment}}$. To make use of diffusivity D , one can assume a one-dimensional random walk for the chain; this implies a relationship $Dt \sim L^2$. The time taken by the chain to escape the tube is approximately the terminal time τ_T , the time needed for the stress relaxation modulus $G(t)$ to drop off of the plateau. The length L can be approximated as aN , the length of each segment times the degree of polymerization. Then, $D_{\text{chain}} \tau_T \sim a^2 N^2$. This expression, combined with the adapted Einstein formula above, implies $\tau_T \sim N^3$. This is very close to the empirical relationship mentioned earlier: $\tau_T \sim N^{3.4}$. In short, the reptation model has made a connection between the hypothetical mechanism of entanglement and the experimentally determined termination time. In other words, the terminal time τ_T is indicative of the duration of time that entanglements will apply stress on the chain.

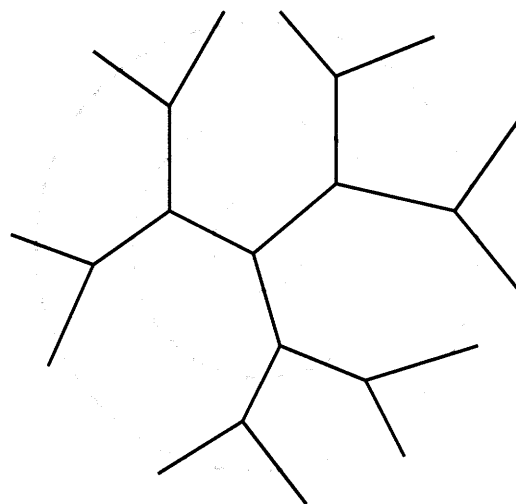
How will this affect a GFP with a few chains covalently attached? The fact that GFP is much wider than a polyacrylamide “tube” means that GFP will remain stationary while its chains undergo entanglement stress. There is a chance that, before the termination time, entanglement stress will impose a force productive to GFP unraveling. However, any fluid dynamics beyond the termination time will not allow the attached chains to apply a force on GFP. Therefore, given a polymer melt, the best strategy seems to be a maximization of degree of polymerization.

Gelation and participation in the infinite cluster

To distribute the applied load across entanglements covalently linked to GFP, it might also be helpful to consider the conditions under which polymers undergo gelation, and what fraction of that macroscopic gel is actually mechanically linked together. To model gelation, the classical Flory-Stockmayer theory starts with a Cayley tree, which is

characterized by the functionality number z (Stockmayer, 1944). The functionality refers to the number of possible connections a node will have with other nodes. If f is the fraction of potential bonds that have formed, and b_i is the number of nodes (or branches if $f=1$) in the i th generation, then $b_n = b_1 [f(z-1)]^{n-1}$. As the number of generations becomes very large, the ability of the cluster to propagate will depend on whether or not f is greater than the percolation threshold $f_c = 1/(z-1)$. When $f < f_c$ corresponds to the sol state, and $f > f_c$ corresponds to the gel state.

Figure 34. Cayley tree of $z=3$. If the innermost circle's node is considered the first generation, then the second generation is the set of nodes between the smallest and medium circles. Adjunct mathematical details may be helpful. Each node (except the first generation node) can give rise to $z-1$ branches. If b_n is the number of branches (or nodes) in the n th generation, then b_{n+1} will have $b_n(z-1)$ branches. In other words, $b_1(z-1)^{n-1} = b_n$. The total number of nodes to the n th generation is $S_n = b_1 \sum_1^n (z-1)^{i-1}$. If f is the fraction of reacted bonds (each bond formation being independent of the others), then the total number of branches up to the n th generation is $B_n = b_1 \sum_1^n [f(z-1)]^{i-1}$. If $f(z-1) \geq 1$, this geometric series will diverge, i.e. create an "infinite" cluster.



Not all members within the polymer volume are part of the "infinite" cluster. To determine the gel fraction, or the fraction of the macrogel that is part of the "infinite" cluster, one can arrive at a recursive relationship by taking advantage of the fact that every node in a mathematically infinite cluster can be treated the same way.

Let P be the probability that a node is connected to the infinite cluster. Let Q be the probability that a node is *not* connected to the infinite cluster, by one specified branch. This means that, given a "first" node, the probability that one of its branches will not connect to the infinite cluster is Q . Given a "second" node adjacent to the first node, the second node can make $z-1$ branches to nodes other than the first node. The

probability that none of the $z-1$ branches will connect to the infinite cluster is Q^{z-1} . The variable f from the previous discussion can be interpreted as the probability that “first” and “second” will be connected. Then, fQ^{z-1} is the probability that there is a “one-two” connection *and* that this connection doesn’t lead to the infinite cluster. The probability that there is no “one-two” connection (and therefore this potential path doesn’t lead to the infinite cluster for the “first” node) is $1-f$. After reasoning out the probabilities for the conditions under which “one-two” doesn’t lead to the infinite cluster, one can sum these probabilities and recursively equate the expression to Q , which by definition is the total probability that “one-two” doesn’t lead to the infinite cluster: $Q=(1-f) + fQ^{z-1}$, with $f>f_c$.

With Q related to f , if P and Q can be related, then P can be expressed transitively in terms of f . Since f is the fraction of reacted bonds, and P is the fraction of reacted bonds that lead to the infinite cluster, $f-P$ is the fraction of active branches that don’t lead to the infinite cluster. The expression Q^z is the probability that a node doesn’t connect with the infinite cluster. Then fQ^z is the probability that a node’s reacted bonds do not lead to the infinite cluster. Therefore, $f-P=fQ^z$, which rearranges to $P/f=1-Q^z$ with $f>f_c$.

The two results above can be solved for the gel fraction P/f , or the fraction of reacted bonds that belong to the infinite cluster. When $z=3$, the Taylor expansion of P/f gives:

$$\frac{P}{f} = 3(f - f_c) + O(f - f_c)^2$$

28) Gel fraction.

In other words, the distribution of macroscopically applied force can be expected to apply to $\sim 3f(f-f_c)$ when $z=3$. Gel fraction is plotted as a function of reactivity f and functionality z in Figure 35. The line $z=4$ corresponds to bis-acrylamide. The line $z=6$

corresponds to GFP with 3 vinyl groups. The line $z=50$ corresponds to the microgels that form prior to macrogel appearance in the polymerization of bis/acrylamide.

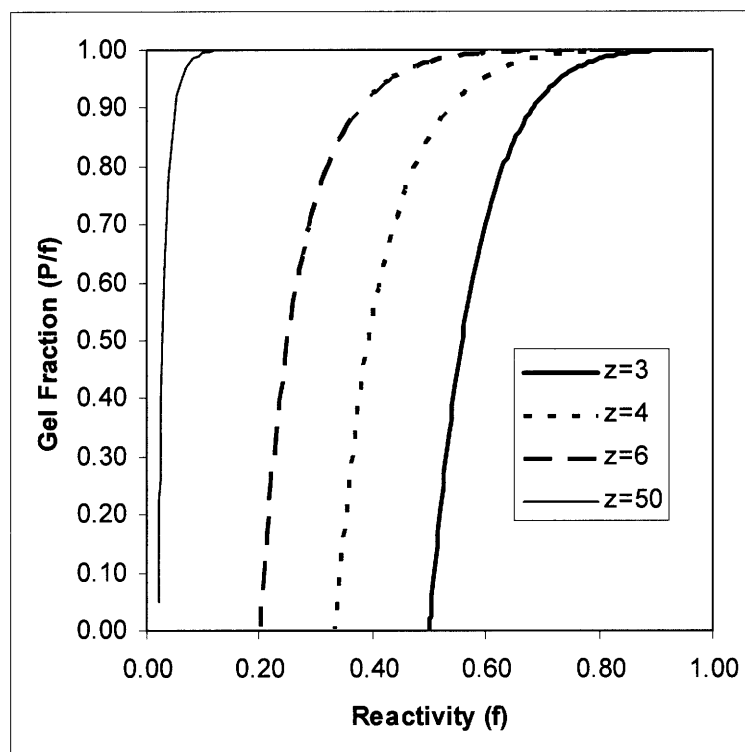


Figure 35. Gel fraction as a function of reactivity and functionality. The functionality numbers $z = 3, 4, 6,$ and 50 are the potential number of bonds a node could make. The gel fraction P/f is the fraction of bonds that are connected to the infinite network. The line $z=4$ corresponds to bis-acrylamide. The line $z=6$ corresponds to GFP with 3 vinyl groups. The line $z=50$ corresponds to the microgels that form prior to macrogel appearance in the polymerization of bis/acrylamide. This chart shows that even though GFP may have a lower diffusivity (and hence lower reactivity) than acrylamide, increasing the functionality with as few as three vinyl groups will significantly improve the probability for GFP to participate mechanically in a polymer gel.

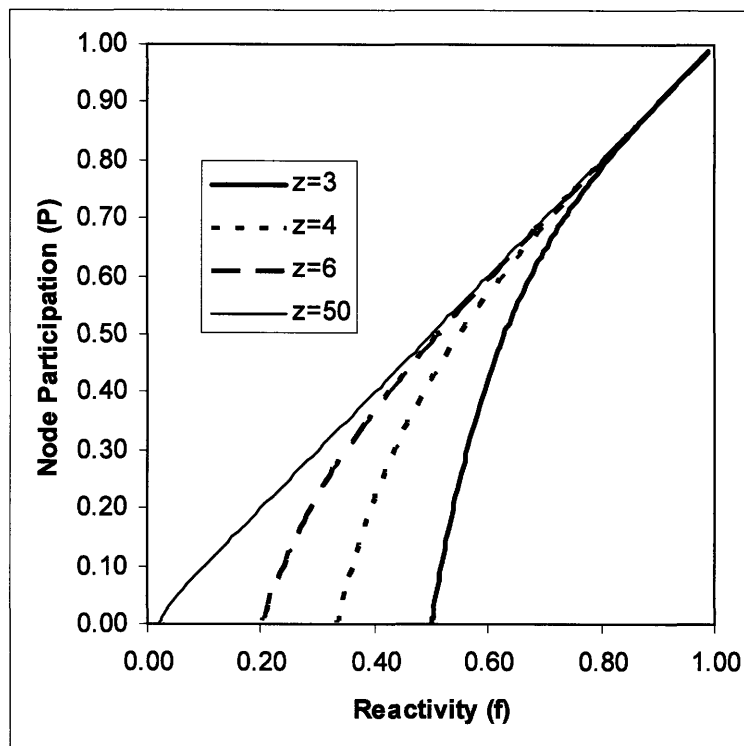


Figure 36. Node participation as a function of reactivity and functionality. The functionality numbers $z = 3, 4, 6,$ and 50 are the potential number of bonds a node could make. The fraction P is the probability that a given particle is part of the infinite network. The line $z=4$ corresponds to bis-acrylamide. The line $z=6$ corresponds to GFP with 3 vinyl groups. The line $z=50$ corresponds to the microgels that form prior to macrogel appearance in the polymerization of bis/acrylamide. This chart shows that while the effects of low reactivity *can* be off-set by high functionality, reactivity seems to pose a fundamental limit to the ability to participate in the macrogel.

Figure 35 suggests that every vinyl attachment to GFP makes a significant increase in the possibility that a given bond will participate in the distribution of force across a network where the fluorescent protein will support some of the load.

In comparison, Figure 36 addresses the question of what fraction of the nodes will participate in energy relaxation processes upon shearing. While the effects of low reactivity *can* be off-set by high functionality, reactivity seems to pose a fundamental limit to the ability to participate in the macrogel. This perspective seems at odds with the positive impression that Figure 35 had projected about the ability of functionality to

compensate for low reactivity. Why does Figure 35 have a much more positive outlook than Figure 36? This seeming clash of viewpoints can be resolved if one considers what is being counted. In Figure 36, all nodes, regardless of their ability to make bonds or not, are counted in the calculation for the fraction of participation. In contrast, Figure 35 only considers the bonds that have already been made, and by discounting nodes of low participation the figure can depict a seemingly better tradeoff between reactivity and functionality. Therefore, the picture is a bit complicated: it's difficult to bond with others, but once you do the game is about how many connections you can make with your neighbors.

What bearing does gel fraction have on the current scenario? The ability to pull on GFP in a polymer depends on its mechanical connectivity with the macrogel, through which macroscopic forces will be applied. This means that for GFP to unfold and lose its optimal fluorescence conformation, it must be a participant in the infinite cluster. The integrity of the macrogel therefore has a direct effect on signal-to-noise issues. Given an effective reactivity $f=0.5$, at most about 40% of the covalently linked GFP in a bis/acrylamide polymer would have the potential to respond by altering optical properties.

Signal-to-noise ratio

In addition to the infinite cluster fraction value of the gel, other aspects make an impact on the ability to detect the signal against the background noise. What factors contribute to the background noise? Noise amplitude estimation can be done within the framework of signal transfer from the specimen to the data file in the computer of the

microscope. The microscope is an instrument that applies light onto a specimen with a certain amount of power, or energy per unit time. This energy rate can be converted into a photon rate if one considers the following. First, each photon has an amount of energy that depends on its wavelength: $E=hc/\lambda$. Second, the light source can be filtered to a narrow range of wavelengths, so that λ can be estimated. Therefore, power can be converted into photons per unit time.

These photons are spread across a portion of the stage with a measureable area, but only a small portion of these photons will excite the GFP fluorophores. The fluorophore's ability to capture a photon depends on the amount of cross-section that is oriented towards the source. Given the GFP concentration, gel thickness, isotropic distribution of GFP orientation, and an assumption that no fluorophore will block another fluorophore, the total amount of fluorophore effective cross-sectional area can be determined. This area, divided by the excitation photon coverage area, is the fraction of photons per unit time that will be absorbed by the fluorophore.

The fluorophore, however, does not emit a photon for each photon absorbed. The quantum yield, or the number of photons emitted divided by the number of photons absorbed, is less than unity because there are multiple paths for the excited GFP fluorophore to relax back to a less energetic state. For example, the fluorophore could undergo a "hula twist" relaxation, or simultaneous twisting of two adjacent bonds. The local environment of the protein, however, impedes nonradiative relaxation processes and increases the portion of radiative relaxation that releases photons.

The emitted light must now be collected by the microscope lens, and this ability to capture the photons depends on the ability of the lens to cover an angular range, whose

coordinate system origin is placed at the specimen. This coverage capacity of an objective is reflected in the value of its numerical aperture. The numerical aperture allows one to calculate the fraction of emitted photons that will pass through to the detector. The detector's sensitivity will depend on the area of the detector's sensor, and the area of detection at each pixel of the sensor.

In the timescale of seconds, the sensor's signal-to-noise ratio will depend on increasing the number of opportunities to gather photons, and this itself will depend on two factors. First, given more time per measurement, or integration time, the noise will tend to cancel itself while the signal will remain. Second, if one increases the light intensity, then more photons per unit time will hit each pixel on the sensor. Root-mean-square of noise amplitude is related to the number of photons in the following manner:

$$\sqrt{\langle A^2 \rangle} \sim \frac{1}{\sqrt{n}}.$$

29) Noise amplitude and photon count.

In the timescale of minutes, however, signal deterioration occurs because the fluorophores themselves are usually subject to bleaching, which destroys the photon-emitting capacity on the molecule. Therefore, the bleaching rate is another important factor to consider.

Because of the many factors mentioned above, a pragmatic approach would be to place on the microscope stage a uniform distribution of a solution containing the GFP fluorophore. By measuring the fluorescence at typical microscope operation parameters, one can estimate the effective noise that will confront any experiment.

Estimation of the signal-to-noise ratio

Using a chambered coverslide, solutions of GFP were excited with a standard inverted fluorescence microscope. The binning was kept at 2, but the exposure time varied from 1 to 500ms.

Characterization of viscoelasticity

To achieve a controlled mechanical input to the GFP-gel material would be akin to making controlled deformations in rheometry. In other words, both the current experimental needs and rheological instrumentation require one to have control over the deformation, for the purpose of measuring fluorescence in the former, and rheological properties in the latter. How are viscosity and elasticity measured? Flow properties are measured by viscometers, but those instruments do not measure elasticity, which is a “solid” property. Therefore, a rheometer, which is a viscometer that also measures elasticity, is used to measure both properties of a material. The common types are the rotational, capillary, extensional, and mixer rheometers. Rotational rheometers apply torque to maintain constant rotation rate on an object immersed in the sample fluid (Hoppmann II and Miller, 1963). Viscosity calculations employ the fact that torque is proportional to viscosity (Huang, 1971a; Huang, 1971b). However, one must correct for variations in shear rate for non-Newtonian fluids (Smith, 1984). In capillary rheometry, a fixed volume at a given temperature is sent through a small opening, and the flow rate is measured (Poiseuille, 1840). Both kinematic and dynamic viscosity is inversely proportional to the flow rate. The density of the fluid is needed to derive the dynamic viscosity. Wall slip can be an issue (Yeow et al., 2003). Extensional rheometers depend on the elongational properties, or the stretching flow of the material (Münstedt, 1979).

Finally, mixer torque rheometers measure the torque associated with the shear stress on colloids within a mixing bowl. The above rheometer designs, however, do not necessarily account for the limits set by sample availability.

Sample limitations have been addressed with microrheometers, such as the sliding plate microrheometer, microcapillary break-up extensional rheometer, and the normal-force-controlled triborheometer (Clasen et al., 2004) . The sliding plate microrheometer, also called the Flexure-based Microgap Rheometer (FMR) makes viscoelastic property measurements from plane couette shearing flows imposed on ~ 10 μL samples between two plates space 1-200 μm apart (Clasen et al., 2006). The miniaturized capillary break-up rheometer (μ -Caber) is an extensional rheometer. Requiring a $1\mu\text{L}$ fluid sample, this instrument elongates the sample into a fluid thread, and the transient extensional behavior is measured to produce data (McKinley and Tripathi, 2000). Finally, the normal-force-controlled triborheometer was developed to address issues that arise on the FMR when the sample thickness is less than $1\mu\text{m}$.

When the gap is less than $1\mu\text{m}$, the problem of sliding plate rheometry becomes ill-defined, due to the scale-dependent interactions of factors such as wall roughness, fluid microstructure, and colloidal impurities. These problems can be overcome at submicron thicknesses, if one recasts the sample characterization in terms of tribometry. In this perspective, a commercial torsional rheometer is modified for the new regime. However, at submicron thicknesses of the fluid sample, the interaction with the wall roughness (which has a lengthscale similar to the sample thickness) becomes significant enough that the obtained data will reflect properties of the fluid-solid pair, not just the

fluid (Kavehpour and McKinley, 2004) .. The obtained data would be usually represented as a classical Stribeck curve (Luengo et al., 1996; Luengo et al., 1997) .

The next generation of rheological instruments adapt technologies such as ultrasonic pulse Doppler mapping and nuclear magnetic resonance imaging (Hou and Kassim, 2005). These technologies allow one to extract additional velocity profile data that addresses long data acquisition times in a laminar flow in a tube. The fact that these new technologies are usually incremental innovations of old approaches emphasizes the basic deformation approaches one can take, such as laminar flow in a tube, parallel plate couette flow, elongation, and transient capillary breakup.

Conjugation details

The approaches available to deform a GFP-gel system have been laid out, as well as guidelines on GFP-hydrogel linkage, but how can one link GFP to the polymer network? That question can be addressed by protein coupling chemistry, whose operating boundaries are determined by the need to preserve native structure and activity. For these reasons, most protein conjugation agents operate in a predominantly aqueous system, within a pH range of 3-11, at a temperature below 318K. However, each protein has its own set of requirements. In the case of GFP, the protein has a viable pH range of 5-11, and its denaturation temperature is at ~338K (Ward and Bokman, 1982). Moreover, commonly used anti-microbial reagents such as NaN_3 can interfere with the desired conjugation (via $\text{S}_{\text{N}}2$) because of its highly nucleophilic characteristic. Other factors that affect the decision of conjugation reactions are: the molecular reagents to be used; the choice of conjugation chemistry; linker group characteristics (e.g. length,

flexibility and polarity); and the stability of coupling in subsequent steps. To choose a coupling reaction, some general factors to consider are: reagent stoichiometry, pH, reaction time, temperature requirement, organic co-solvent choice, and the organic co-solvent concentration. Beyond the basic framework, one can also protect certain functional groups or expose new sites.

After choosing the parameters, measuring the efficacy of the conjugation experiments would be useful. How can one measure the addition of a molecular conjugate to a macromolecule? One method is a combination of enzyme digestion and mass spectrometry (MS). While MS machines are generally accurate to fractions of a percent, the 27 kDa GFP molecule would be so massive that it would mask the presence of any conjugations on the order of ~100 Da. Therefore, enzymes known to cleave peptide bonds at a set of specific sequences is necessary to fragment the protein into pieces sufficiently small. When partial digestion results in peptides of ~10 amino acids, the MS can discern differences that an extra acrylate group would make in terms of mass.

Table 6. Proteolytic enzymes for mass spectrometry. These enzymes are used in digests of proteins, to make pieces that the MS machine can handle with sufficient resolution.

enzyme	cuts N-terminal to	cuts C-terminal to
trypsin		arg, lys
asp-N		glu, asp
chymotrypsin		tyr, trp, leu, phe

Acrylamide and radical polymerization

To link GFP to acrylamide, one requires an understanding of the radical polymerization that links acrylamide monomers into polyacrylamide (Figure 37). The common polyacrylamide crosslinker *N,N'*-(1,2-Dihydroxyethylene)*bis*-acrylamide also

has double bonds that can conjugate with a radical molecule. The alternative is to use the “amine” portion of the amide group, which might act as a nucleophilic reactant.

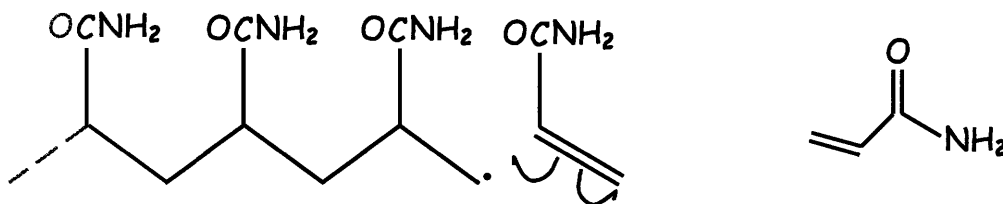


Figure 37. Radical polymerization of acrylamide, chain reaction. The lone electron (•) on the chain combines with an electron from the monomer to form a single bond between the two entities.

Compared to the acrylamide, GFP is a much more complex molecule. Its analysis was conducted from the perspective of major crosslinker chemistry groups. The major groups of crosslinker chemistry are the amine-reactive, sulfhydryl-reactive, carbonyl/glyco-reactive, carboxyl-reactive, arginine-specific, and nonspecific chemistries. Each crosslinker chemistry group was considered in the context of solvent accessibility. Solvent accessible nitrogens that were primary amines were found on 20 lysine residues and the N-terminus. Amide groups were not considered in this situation (to be discussed later). Solvent accessible surface area of the sulfurs seemed insignificant except for methionine 218. Because there was not a significant number of carbonyl bonds after accounting for peptide bonds, carboxylic groups and the lack of sugars, they were not considered. The carboxylic group was a composite of the C-terminus, the aspartates, and the glutamates. Solvent accessible surface area for the oxygens of the functional group varied from approximately 1-83 Å², with a mean of ~41 Å² (C-terminus was deemed negligible). From graphics depictions, at least ten were considered to be accessible, and that ten would be sufficient for conjugation purposes. Of the seven

arginines, six seemed have access to incoming coupling molecule. Because some degree of specificity was desired, nonspecific chemistries were not considered.

Table 7. Solvent accessibility of potential conjugation sites.

Functional group	Population on molecule	Potential candidates
amine (primary)	lys(19)	All 19 accessible
sulfhydryl	cys(2), met(4)	met153(?)
carboxylic	C-ter, glu(15), asp(17)	10+ accessible
arginine	arg(7)	6 accessible

Crosslinkers revisited.

Next, heterofunctional crosslinkers were chosen over homofunctional crosslinkers. Homofunctional crosslinkers have the risk of self-conjugation between molecules of the same structure. Moreover, heterofunctional crosslinkers allows for partners that have differences in accessibilities of the relevant functional groups.

These above factors led to two choices – N-Hydroxysuccinimide-esters (NHS-esters) and 1-ethyl-3-[3-dimethylaminopropyl]carbodiimide hydrochloride (EDC). Figure 38 shows the general EDC plan, where the ball represents GFP and R-NH₂ represents acrylamide. EDC is a bifunctional, zero-length conjugation reagent that connects a primary amine and a carboxylic group (Sheehan et al., 1961; Sheehan et al., 1965). The result of a successful conjugation is an amide bond formation (Williams and Ibrahim, 1981). EDC's tendency to hydrolyze in an aqueous environment must be carefully controlled (Gilles et al., 1990). In addition, EDC may react with sulfhydryl groups (Carraway and Triplett, 1970) and/or tyrosine residues (Carraway and

Koshland, 1968). AEDC, a variation of EDC was also considered, for its ability to break the crosslink that had been formed.

The other option, depicted in Figure 39, is the NHS-ester plan, where the ball again represents GFP but this time the imidoester will be replaced by acrylic acid NHS ester. *N*-hydroxysuccinimide (NHS) esters are used to acylate a primary amine (Bragg and Hou, 1975; Lomant and Fairbanks, 1976). While NHS compounds can acylate the nitrogen of the imidazole ring on a histidine residue, the subsequent hydrolysis is favored over a stable conjugated structure (Cuatrecasas and Parikh, 1972). Efficient conjugation requires a careful control of the pH and temperature. At 25°C, the half-life is ~1hour (Staros et al., 1986). However, at cooler temperatures pH sensitivity can be dramatic. At pH 8.6 and 4°C, the half-life was measured to be only 10 minutes (Cuatrecasas and Parikh, 1972), whereas at pH7 and 0°C, the half-life was approximately 4-5 hours (Lomant and Fairbanks, 1976).

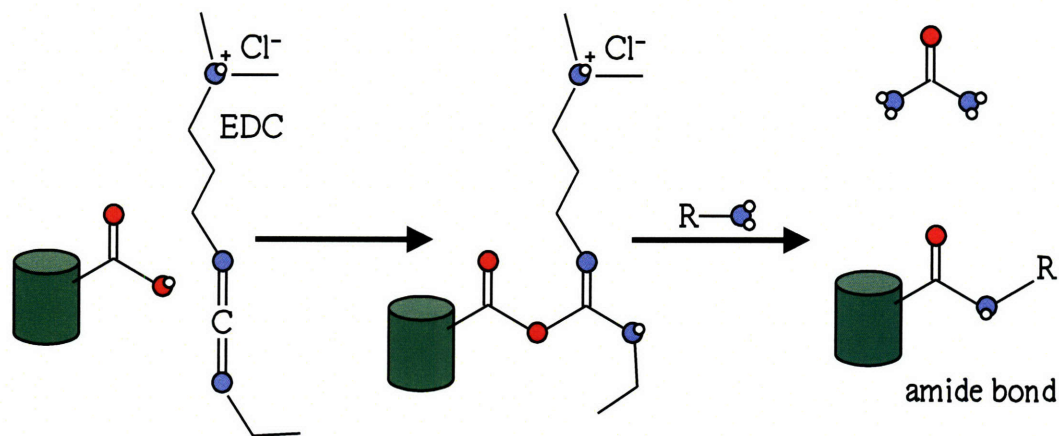


Figure 38. EDC conjugation steps. A carboxylate-containing molecule (e.g. GFP) reacts with EDC to form an *o*-acylisourea reactive ester, which in turn reacts with a primary amine to form an amide bond.

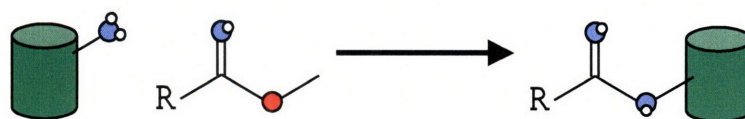


Figure 39. NHS-ester conjugation mechanism. The primary amines of lysines in GFP reacts with the imidoester to produce an amidine linkage.

Once GFP gains vinyl groups so that it can act as a cross-linker, the polymerization of acrylamide must be considered in terms of the scale of production. In \sim mL amounts, the protocol for polyacrylamide production for gel electrophoresis is well-established. However, in \sim μ L quantities, additional factors need to be taken into account. For example, the standard TEMED volume of 10 μ L in a 300 μ L reaction volume could have significant consequences on the pH without the necessary buffering capacity. In addition, buffering capacity increases must occur while maintaining the ionic strength at a standard 150mM. Another important factor is the introduction of ammonium persulfate (APS). A standard introduction of 0.67wt% would result in less than 1 μ L, so the *ex tempera* solution must be made at a higher dilution. Adding too much ammonium persulfate would also cause pH changes that may precipitate GFP. Once the reagents have been mixed together, oxygen poisoning must be addressed by butanol, vacuum, or pure nitrogen gas supply. A stream of pure nitrogen or vacuum may dehydrate the reaction volume. On the other hand, organic layer of butanol may be favored by one or more of the reagents – a factor that was previously less significant because of the depth of the reaction volume.

There are published data on that predict polymer properties, given total monomer concentration and crosslinker fraction. However, multiple factors, such as oxygen

poisoning, affect the process. Therefore, it was decided to establish some knowledge of polymer properties to verify that the polymerization was reproducible.

In summary, polyacrylamide was justified as a relevant hydrogel, and a choice of conjugation mechanisms were made. The question of whether a GFP-gel composite can detect cell motility forces was divided into aspects of the problem.

Experiment Objectives

Estimate the signal-to-noise sensitivity requirements in a typical fluorescence microscope setting.

Verify linking to the polyacrylamide hydrogel by serial washes.

Conjugate vinyl groups to GFP and verify.

Use shear stress to affect the fluorescence activity of GFP.

Results

Signal-to-Noise

The chambered slide was filled with varying concentration of GFP, and pictures were taken at the parameter values specified in Table 8. The images themselves were uniform shades of gray (not shown).

Table 8. Signal data on an inverted fluorescence microscope. A chambered slide was filled with GFP-containing solutions at varying concentrations, and pictures were taken with the inverted microscope. The signal strengths collected for all pixels in a given picture were averaged, and the standard deviation was taken.

Well	No.	Exposure time [ms]	Bin ratio	Mean	Std Dev	Median	Pixels
A	2	1000	2	16.49	0.57	16	326400
C	1	10	2	9.76	0.43	10	326400
C	1	500	2	12.93	0.43	13	326400
H	2	500	2	13.25	0.49	13	326400
F	2	500	2	13.41	0.51	13	326400
E	2	500	2	20.50	2.41	20	326400
D	2	500	2	60.23	2.66	60	326400
C	2	500	2	255.00	0.00	255	326400
C	2	100	2	73.30	3.05	73	326400
B	2	100	2	255.00	0.00	255	326400
B	2	10	2	59.97	2.55	60	326400
B	2	50	2	253.54	3.60	255	326400
B	2	30	2	163.91	7.25	164	326400
B	2	30	2	151.60	6.54	152	326400
B	2	20	2	112.17	4.90	112	326400
B	2	20	2	104.09	4.38	104	326400
A	2	1	2	37.94	1.53	38	326400
A	2	5	2	147.80	6.50	148	326400
A	2	7	2	201.70	8.87	202	326400
A	2	8	2	233.10	10.42	234	326400
B	2	35	2	179.42	7.74	180	326400
B	2	40	2	201.67	8.71	202	326400
B	2	45	2	225.54	9.73	226	326400
B	2	50	2	245.19	9.05	247	326400
A	2	1	2	37.72	1.57	38	326400
A	2	2	2	64.58	2.80	65	326400
A	2	3	2	92.38	4.13	93	326400
A	2	4	2	119.83	5.41	120	326400
A	2	5	2	148.88	6.72	149	326400
A	2	6	2	174.54	7.93	175	326400
A	2	7	2	209.39	9.46	210	326400
A	2	8	2	234.67	10.69	235	326400
A	2	9	2	253.05	4.43	255	326400
A	2	10	2	54.32	2.25	54	326400
A	2	20	2	99.16	4.26	99	326400
A	2	30	2	146.19	6.30	146	326400
A	2	40	2	195.26	8.35	195	326400
A	2	50	2	237.14	10.19	237	326400

AA-GFP conjugation

Table 9. Asp-N digest product candidates for AA-GFP. Mass spectrometer measurements of molecular weight (MH+) and expected digest mechanisms for Asp-N protease catalysis provided the following list of possible sequences. The sequence provides the peptide fragment location (PFL), the percent of macromolecular mass(%Mass), and the percent of GFP amino acid sequence (%GAA).

Sequence	MH+	%Mass	PFL	%GAA
PILVELDGDV	1069.58	3.98	13-22	4.20
VSGEGEGDATY	1084.44	4.04	29-39	4.62
DDFKSAMPEGYVQER	1803.84	6.72	82-96	6.30
SAMPEGYVQER	1266.58	4.72	86-96	4.62
MPEGY	596.24	2.22	88-92	2.10
IELKGIDFKEDGNILGHKMEYN	2563.29	9.54	123-144	9.24
NILGHKMEY	1104.55	4.11	135-143	3.78
VYIMADKPKNGI	1348.73	5.02	150-161	5.04
PKNGIKVN	869.52	3.24	157-164	3.36
HNIKDGSVQLAD	1296.65	4.83	169-180	5.04
DHYQQNTPIG	1172.53	4.37	180-189	4.20
DGPVLLPDNHYLSTQSALS	2155.10	8.02	190-209	8.40
DNHYLSTQSALS	1463.71	5.45	197-209	5.46
LSTQSALSKDPNEK	1517.78	5.65	201-214	5.88
KRDHMI	799.42	2.98	214-219	2.52
DELYK	667.33	2.48	234-238	2.10

Table 10. Trypsin cleavage product candidates for AA-GFP. Mass spectrometer measurements of molecular weight (MH+) and expected digest mechanisms for trypsin protease catalysis provided the following list of possible sequences. The sequence provides the peptide fragment location (PFL), the percent of macromolecular mass(%Mass), and the percent of GFP amino acid sequence (%GAA).

Sequence	MH+	%Mas s	PFL	%GA A
FVSVSGEGEGD	983.40	3.66	27-36	4.2
TYGKLT	682.38	2.54	38-43	2.5
YPDHMKQHDFFK	1592.7	5.93	74-85	5.0
DFFKSAMPEGYVQER	1803.8	6.72	82-96	6.3
PEGYVQER	977.47	3.64	89-96	3.3
YVQERTIFFKDDGNYK	2022.9	7.53	92-107	6.7
TIFFKDDGNYK	1347.6	5.02	97-107	4.6
TIFFKDDGNYKTR	1604.8	5.97	97-109	5.4
TRAEVKFEGDTLVNR	1734.9	6.46	108-	6.3
RAEVKFE	878.47	3.27	109-	2.9
AEVKFEGDTLVNR	1477.7	5.50	110-	5.4
AEVKFEGDTLVNRIELK	1961.0	7.30	110-	7.1
FEGDTLV	780.38	2.91	114-	2.9
FEGDTLVNR	1050.5	3.91	114-	3.7
GIDFKEDGNILGHK	1542.7	5.74	127-	5.8
EDGNILGHK	982.50	3.66	132-	3.7
NGIKVNFKIR	1188.7	4.43	159-	4.2
YQQNTPIGD	1035.4	3.85	182-	3.7
DPNEKR	758.38	2.82	210-	2.5
			215	2

Table 11. Chymotrypsin cleavage products for AA-GFP. Mass spectrometer measurements of molecular weight (MH+) and expected digest mechanisms for chymotrypsin protease catalysis provided the following list of possible sequences. The sequence provides the peptide fragment location (PFL), the percent of macromolecular mass(%Mass), and the percent of GFP amino acid sequence (%GAA).

Sequence	MH+	%Mas s	PFL	%GAA
TGVVPI	585.36	2.18	9-14	2.52
SVSGEGEGDATY	1171.4	4.36	28-39	5.04
	7			
SRYPDHM	905.39	3.37	72-78	2.94
SRYPDHMKQHDF	1560.7	5.81	72-83	5.04
	0			
SRYPDHMKQHDF	1707.7	6.36	72-84	5.46
	7			
HMKQHDFFKSA	1375.6	5.12	77-87	4.62
	6			
DFFKSAMPEGY	1291.5	4.81	82-92	4.62
	7			
FFKSAMPEGYVQ	1403.6	5.23	83-94	5.04
	7			
KSAMPEGY	882.40	3.29	85-92	3.36
KSAMPEGYVQER	1394.6	5.19	85-96	5.04
	7			
KSAMPEGYVQERTIF	1755.8	6.54	85-99	6.30
	7			
KSAMPEGYVQERTIFF	1902.9	7.08	85-100	6.72
	4			
VQERTIF	892.49	3.32	93-99	2.94
VQERTIFF	1039.5	3.87	93-100	3.36
	6			
KTRAEVKFEGDTL	1493.8	5.56	107-	5.46
	0		119	
EVKFEGDTLVNRIELKGIDFKE	2579.3	9.60	111-	9.24
	7		132	
ELKGIDFKEDGNILGHKMEYN	2450.2	9.12	124-	8.82
	0		144	
KGIDF	579.31	2.16	126-	2.10
			130	
KGIDFKEDGNIL	1348.7	5.02	126-	5.04
	1		137	
KGIDFKEDGNILGH	1542.7	5.74	126-	5.88
	9		139	
GIDFKEDGNILGHK	1542.7	5.74	127-	5.88
	9		140	
KEDGNILGH	982.50	3.66	131-	3.78
			139	
GHKMEYNYNSHNVY	1755.7	6.54	138-	5.88
	5		151	
PKNGIKVNFKI	1257.7	4.68	157-	4.62
	7		167	

KIRHNIKDGSVQ	1394.7	5.19	166-	5.04
	9		177	
KIRHNIKDGSVQL	1507.8	5.61	166-	5.46
	7		178	
KIRHNIKDGSVQLADHY	1994.0	7.42	166-	7.14
	6		182	
KIRHNIKDGSVQLADHYQ	2122.1	7.90	166-	7.56
	2		183	
IRHNIK	780.48	2.91	167-	2.52
			172	
LADHY	618.29	2.30	178-	2.10
			182	
LADHYQQNTPIGDGPVLLPDNHY	2577.2	9.59	178-	9.66
	4		200	
LADHYQQNTPIGDGPVLLPDNHYL	2690.3	10.0	178-	10.0
	2	2	201	8
LADHYQQNTPIGDGPVLLPDNHYLSTQ	3006.4	11.1	178-	11.3
	6	9	204	4
LADHYQQNTPIGDGPVLLPDNHYLSTQSAL	3277.6	12.2	178-	12.6
	1	0	207	1
ADHYQQNTPIGDGPVLLPDNHY	2464.1	9.17	179-	9.24
	5		200	
ADHYQQNTPIGDGPVLLPDNHYLSTQSAL	3164.5	11.7	179-	12.1
	3	8	207	8
QQNTPIGDGPVLLPDNHY	1977.9	7.36	183-	7.56
	7		200	
QQNTPIGDGPVLLPDNHYL	2091.0	7.78	183-	7.98
	5		201	
QQNTPIGDGPVLLPDNHYLSTQ	2407.1	8.96	183-	9.24
	9		204	
QQNTPIGDGPVLLPDNHYLSTQSAL	2678.3	9.97	183-	10.5
	4		207	0
SKDPNEKRDHM	1356.6	5.05	208-	4.62
	3		218	
RDHMILLEFVTAAGITH	1924.0	7.16	215-	7.14
	1		231	
ITHGMD	673.30	2.51	229-	2.52
			234	
GMDELYK	855.39	3.18	232-	2.94
			238	

AAM-GFP in hydrogel

The following table in RFU units was obtained. The control was a hydrogel with only physical encapsulation of GFP. The experimental was a hydrogel made with AAM-GFP, which had the potential to be physically and/or chemically incorporated into the

hydrogel. Washings of the gels over a period of several weeks were measured for fluorescence activity. The results are shown in Table 12.

Table 12. Fluorescence activity in buffer solution removed from GFP-encapsulated hydrogels. Units are in Reference Fluorescence Units.

Wash	Avg _C	SD _C	CV% _C	Avg _E	SD _E	CV% _E
1	3737.9	88.9	2.4	2243.7	42.0	1.9
2	2932.9	79.1	2.7	1797.6	33.3	1.9
3	63.1	1.0	1.6	4.9	0.3	6.1
4	3.7	0.1	3.5	1.2	0.1	5.0

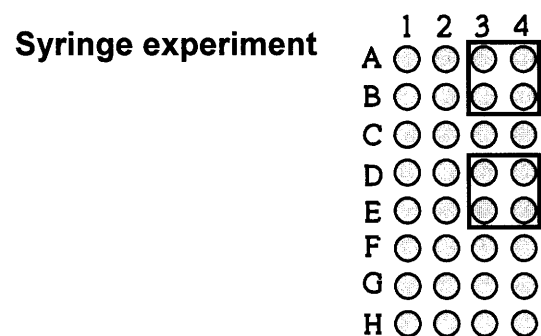


Figure 40. Schematic of the syringe experiment. Columns 1 and 2 were not used. The experiment primarily relied on the wells enclosed by the two squares.

Table 13. Raw RFU values for wells vs. time. Shearing by Hamilton syringe was done after t3 and before t4. TEMED introduction for column 3 (wells A3, B3, D3, E3) happened before shearing or measurement began. TEMED introduction for column 4 (wells A4, B4, D4, E4) occurred between t3 and t4.

	t1	t2	t3	t5	t6	t7	t8	t9	t10
time	16:30	16:34	16:37	16:57	17:07	17:18	17:24	17:48	18:14
A3	10941	10919	12099	11460	9161	7799	7355	6513	6237
A4	11438	11825	11929	6548	6872	6597	6479	6303	6094
B3	12489	12418	11925	11078	8119	6666	6284	5616	5288
B4	12221	12262	10869	10268	10292	10269	10164	9545	8316
C3	0.320	0.396	-0.243	-0.201	-0.051	0.488	0.310	0.177	
C4	0.093	-0.388	0.114	-0.386	0.209	-0.459	-0.311	0.010	
D3	29215	26189	22992	17067	15904	15015	14583	12731	8093
D4	38604	38345	37680	25859	23112	21695	21118	19141	17202
E3	32177	30048	29017	24637	22939	21826	21336	18981	17169
E4	39154	39086	38433	31282	25304	22248	21045	17483	14630
F3	-0.485	0.064	0.175	0.297	-0.274	-0.288	-0.082	-0.250	
F4	0.073	-0.720	-0.046	0.290	0.115	0.258	0.032	0.064	

To put Table 13's values into perspective, a given well's RFU values were normalized against the maximum RFU value for that well (usually t1). The normalized values were then expressed in percentages, and comparisons were made on plots.

Discussion

Signal-to-Noise

The values recorded in the Results indicate that the signal-to-noise ratio varied with the signal strength. However, at all times the minimum signal-to-noise ratio exceeded ~15:1. In other words, the typical setup is sensitive enough to detect a fluorescence change of 20%.

Table 14. Analysis of signal measurements from inverted microscope. Gray parts were included to match this table to its counterpart in the Results section. The CV% was calculated.

Well	No.	Exposure time [ms]	Bin ratio	Pixels	Median	Mean	Std Dev	CV%
A	2	1000	2	326400	16	16.49	0.57	3.5
C	1	10	2	326400	10	9.76	0.43	4.4
C	1	500	2	326400	13	12.93	0.43	3.3
H	2	500	2	326400	13	13.25	0.49	3.7
F	2	500	2	326400	13	13.41	0.51	3.8
E	2	500	2	326400	20	20.5	2.41	11.8
D	2	500	2	326400	60	60.23	2.66	4.4
C	2	500	2	326400	255	255	0	0.0
C	2	100	2	326400	73	73.3	3.05	4.2
B	2	100	2	326400	255	255	0	0.0
B	2	10	2	326400	60	59.97	2.55	4.3
B	2	50	2	326400	255	253.54	3.6	1.4
B	2	30	2	326400	164	163.91	7.25	4.4
B	2	30	2	326400	152	151.6	6.54	4.3
B	2	20	2	326400	112	112.17	4.9	4.4
B	2	20	2	326400	104	104.09	4.38	4.2
A	2	1	2	326400	38	37.94	1.53	4.0
A	2	5	2	326400	148	147.8	6.5	4.4
A	2	7	2	326400	202	201.7	8.87	4.4
A	2	8	2	326400	234	233.1	10.42	4.5
B	2	35	2	326400	180	179.42	7.74	4.3
B	2	40	2	326400	202	201.67	8.71	4.3
B	2	45	2	326400	226	225.54	9.73	4.3
B	2	50	2	326400	247	245.19	9.05	3.7
A	2	1	2	326400	38	37.72	1.57	4.2
A	2	2	2	326400	65	64.58	2.8	4.3
A	2	3	2	326400	93	92.38	4.13	4.5
A	2	4	2	326400	120	119.83	5.41	4.5
A	2	5	2	326400	149	148.88	6.72	4.5
A	2	6	2	326400	175	174.54	7.93	4.5
A	2	7	2	326400	210	209.39	9.46	4.5
A	2	8	2	326400	235	234.67	10.69	4.6
A	2	9	2	326400	255	253.05	4.43	1.8
A	2	10	2	326400	54	54.32	2.25	4.1
A	2	20	2	326400	99	99.16	4.26	4.3
A	2	30	2	326400	146	146.19	6.3	4.3
A	2	40	2	326400	195	195.26	8.35	4.3
A	2	50	2	326400	237	237.14	10.19	4.3

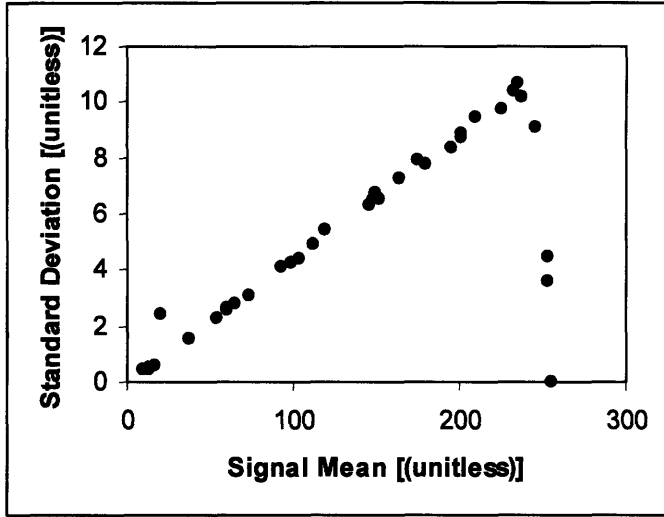
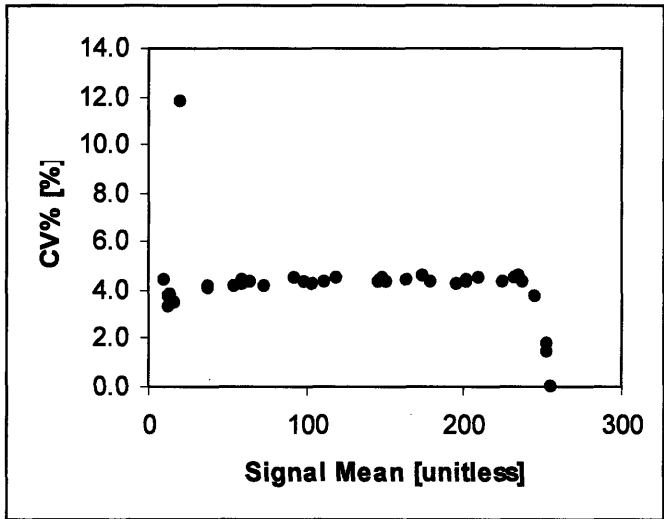


Figure 41. Comparison of noise to signal average on the inverted microscope. Rising signal also increases the standard deviation.



can report a maximum of 255, so any fluorescence intensity beyond the useful sensor range would register as the maximum. When maximum intensity is reached by all the camera pixel sensors, the variance would drop to zero. The saturation effect however, affects the variance of all signals in the top 7% of measured intensities. In other words, above 93% the signal's normal distribution is noticeably distorted. This distortion is important in quantitative analyses, where many statistical tools assume normal distributions of the random variable input data. To avoid these complications, it may be wise to take pictures whose pixels all stay sufficiently away from the saturation limit (7% in this present case).

Conjugation of acrylic acid and GFP

Examination of the data showed some peptides that were heavier than they should have been, if they were unmodified. In trypsin digest/MS data, a significant number of credible peptides had a molecular weight of 1712.81, which most closely resembled TIFFKDDGNYKTR. The normal sequence TIFFKDDGNYKTR has a MW of 1604.7832 Da (N-terminal amine; C-terminal carboxylic acid). The protonated MW (MH⁺) is 1605.791 Da, which indicates a difference of 107.02 Da. If two Acrylic Acids were attached, the expected increase in mass would be 108 Da. This suggests that the peptide was modified by two acrylic acids. The only possible attachments are the primary amine groups of the two lysine residues.

The alternative explanations for a peptide sequence of that molecular weight might be due to an entirely different sequence altogether, or an extra amino acid that may have been attached. The possibility of an entirely different sequence is assumed here to be negligible, because the enzyme digest-MS protocol is a common and well-established

one. The possibility of an extra amino acid is also unlikely. Only serine is within 10 g/mol of the extra weight detected on the peptide. However, the N-terminus of the peptide normally connects to arginine, with a molecular weight of 174.2 g/mol, and the C-terminus normally connects to alanine, with a molecular weight of 89.1 g/mol. Because the molecular weights of the adjacent amino acids are so far from 107 g/mol, this alternative explanation is improbable. The trypsin digest had coverage from residues 97 to 140:

MSKGEELFTG VVPILVELDG DVNGQKFSVS GEGEGDATYG KLTLKFICTT GKLPVPWPTL
 VTTFYGVQC FSRYPDHMKQ HDFFKSAMPE GYVQERTIFF **KDDGNYKTRA** **EVKFEGDTLV**
NRIELKGIDF **KEDGNILGHK** MEYNYNSHNV YIMADKPKNG IKVNFKIRHN IKDGSVQLAD
 HYQQNTPIGD GPVLLPDNHY LSTQSALSKD PNEKRDHMIL LEFVTAAGIT HGMDELYK

The entire wtGFP has 18 lysines, of which 5 are in 97-140. Therefore, 2 out of 5 measurable, potential conjugations occurred in the scope of the trypsin digest

In the chymotrypsin/MS data, met-88 seems to have been modified:

Sequence	MH+
F.KSAM*PEGYVQERTIF.	1771.8
F	7
F.KSAMPEGYVQERTIF.F	1755.8
	7
F.KSAM*PEGY.V	898.40

The first two sequences suggest a 16g/mol object that's attached to the methionine. Methionine oxidation by a double-bond attachment of an oxygen to the sulfur atom would account for this extra mass. In addition, there appears to be a modification on a lysine.

Sequence	MH+	z	P	XC	DeltaC n	Sp	RSp	Ions	Count
F.K#IRHNIKDGSVQLADHYQ. Q	2176.1 2	3	2e+001	2.726	0.258	660.8	1	25/68	

It is lys-166 on the peptide 166-183, which normally has a MH+ weight of 2123.38, so the attached ligand is 52.74 g/mol. Coverage for this digest:

MSKGEELFTG VVPILVELDG DVNGQKFSVS GEGEGDATYG KLTCLKFICTT GKLPVPWPTL
 VTTFSYGVQC FSRYPDHMKQ HDFFKSAMPE GYVQERTIFF KDDGNYKTRA EVKFEGDTLV
 NRIELKGIDF KEDGNILGHK MEYNYNSHNV YIMADKPKNG IKVNFKIRHN IKDGSVQLAD
HYQNTPIGD GPVLLPDNHY LSTQSALSSKD PNEKRDHMIL LEFVTAAGIT HGMDELYK

Six of the lysines are covered.

The asp-N digest/MS data had no signs of modifications. Asp-N covered the following areas:

MSKGEELFTG VVPILVELDG DVNGQKFSVS GEGEGDATYG KLTCLKFICTT GKLPVPWPTL
 VTTFSYGVQC FSRYPDHMKQ HDFFKSAMPE GYVQERTIFF KDDGNYKTRA EVKFEGDTLV
 NRIELKGIDF KEDGNILGHK MEYNYNSHNV YIMADKPKNG IKVNFKIRHN IKDGSVQLAD
HYQNTPIGD GPVLLPDNHY LSTQSALSSKD PNEKRDHMIL LEFVTAAGIT HGMDELYK

Summary of AA-GFP reaction

	10	20	30	40	50
T	MSKGEELFTG	VVPILVELDG	DVNGQKFSVS	GEGEGDATYG	KLTCLKFICTT
Y	MSKGEELFTG	VVPILVELDG	DVNGQKFSVS	<u>GEGEGDATYG</u>	KLTCLKFICTT
N	MSKGEELFTG	VVPILVELDG	DVNGQKFSVS	GEGEGDATYG	KLTCLKFICTT
	60	70	80	90	100
T	GKLPVPWPTL	VTTFSYGVQC	FSRYPDHMKQ	HDFFKSAMPE	<u>GYVQERTIFF</u>
Y	GKLPVPWPTL	VTTFSYGVQC	<u>FSRYPDHMKQ</u>	<u>HDFFKSAMPE</u>	<u>GYVQERTIFF</u>
N	GKLPVPWPTL	VTTFSYGVQC	FSRYPDHMKQ	<u>HDFFKSAMPE</u>	<u>GYVQERTIFF</u>
	110	120	130	140	150
T	<u>KDDGNYKTRA</u>	<u>EVKFEGDTLV</u>	<u>NRIELKGIDF</u>	<u>KEDGNILGHK</u>	MEYNYNSHNV
Y	<u>KDDGNYKTRA</u>	<u>EVKFEGDTLV</u>	<u>NRIELKGIDF</u>	<u>KEDGNILGHK</u>	MEYNYNSHNV
N	<u>KDDGNYKTRA</u>	<u>EVKFEGDTLV</u>	<u>NRIELKGIDF</u>	<u>KEDGNILGHK</u>	MEYNYNSHNV
	#	#			
	160	170	180	190	200
T	YIMADKPKNG	IKVNFKIRHN	IKDGSVQLAD	<u>HYQNTPIGD</u>	<u>GPVLLPDNHY</u>
Y	YIMADKPKNG	IKVNF <u>KIRHN</u>	<u>IKDGSVQLAD</u>	<u>HYQNTPIGD</u>	<u>GPVLLPDNHY</u>
N	YIMADKPKNG	IKVNFKIRHN	IKDGSVQLAD	<u>HYQNTPIGD</u>	<u>GPVLLPDNHY</u>
		#			
	210	220	230	240	250
T	LSTQSALS	PNEKRDHMIL	LEFVTAAGIT	HGMDELYK	
Y	<u>LSTQSALS</u> SKD	PNEKRDHMIL	LEFVTAAGIT	HGMDELYK	
N	<u>LSTQSALS</u> SKD	PNEKRDHMIL	LEFVTAAGIT	HGMDELYK	

Of the 19 total potential conjugation sites (18 lysines and one N-terminus), 11 lysines were covered, three of which were conjugated with acrylic acid; this is a reaction extent of 27%.

On vmd for a minimized pdb of one segment of 1GFL, the modified residues' alpha carbon positions were examined.

resid	x	y	z	dist to 101	dist to 107	dist to 166
101	18.978001	85.992996	-4.162000		14.329	10.030
107	13.922000	80.556000	-16.417999	14.329		14.829
166	10.660000	80.842003	-1.955000	10.030	14.829	

AAM-GFP in hydrogel

The results clearly indicate that the control hydrogel released a significantly higher level of GFP over time than the experimental hydrogel. This supports the hypothesis that the experimental hydrogel will be able to retain its GFP better than the control hydrogel.

Syringe experiment

To put Table 13's values into perspective, a given well's RFU values were normalized against the maximum RFU value for that well (usually t1).

Normalized data are plotted in Figure 43.

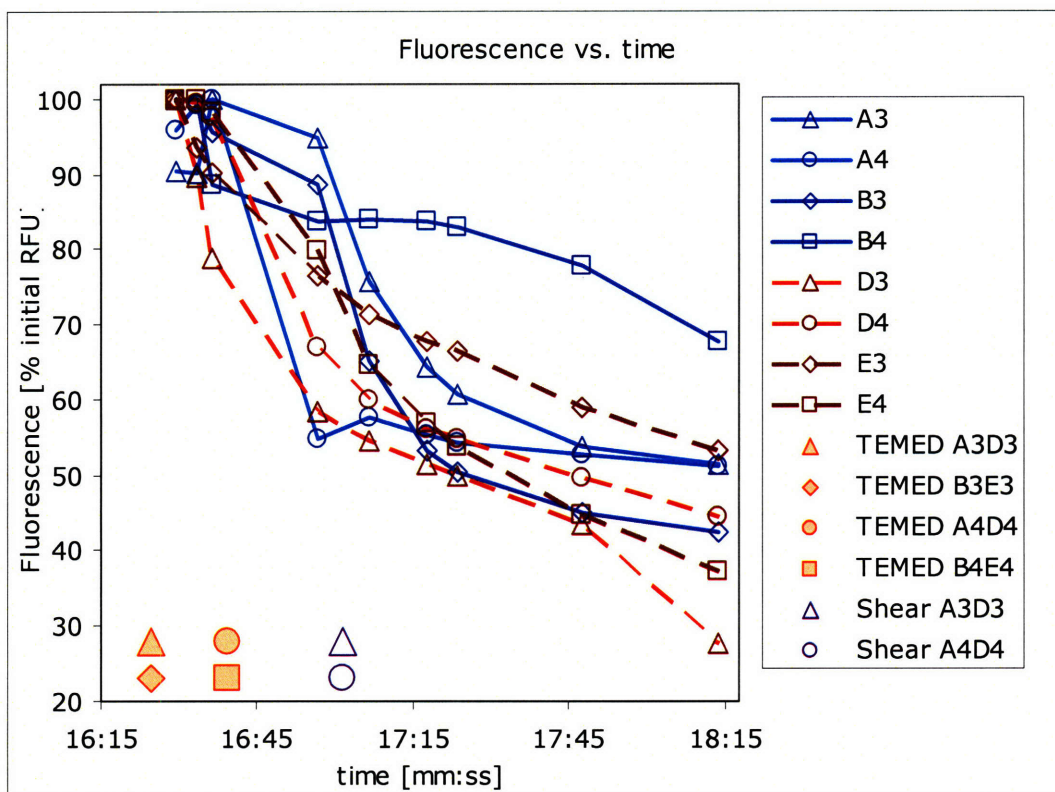


Figure 43. Normalized fluorescence activity over time. Blue marks indicate GFP-acrylate-incorporated hydrogel, where RFU was expected to decrease. Red marks indicate GFP-incorporated hydrogel, where RFU was not expected to decrease. Substantial deterioration however, seems to occur. This data is recast in terms of individual questions below.

What does Figure 43 indicate about the various factors that affect the ability to impose macroscopic force at microscopic dimensions? For example, how does polymerization time affect fluorescence, and what are the ramifications? As shown in Table 15, the eight wells can be arranged to compare see what effect the length of polymerization time had in the context of this experiment.

Table 15. Polymerization time and fluorescence activity. Each pair of wells that are listed have the same conditions, except for the time at which TEMED was added to the well.

	A3 vs. A4	D3 vs. D4	B3 vs. B4	E3 vs. E4
acrylamide	both	both	both	both
GFP	both	both	both	both
AA NHS E	both	neither	both	neither
TEMED	$t_{A3} < t_{A4}$	$t_{D3} < t_{D4}$	$t_{B3} < t_{B4}$	$t_{E3} < t_{E4}$
shearing	$t_{A3} = t_{A4}$	$t_{D3} = t_{D4}$	N/A	N/A

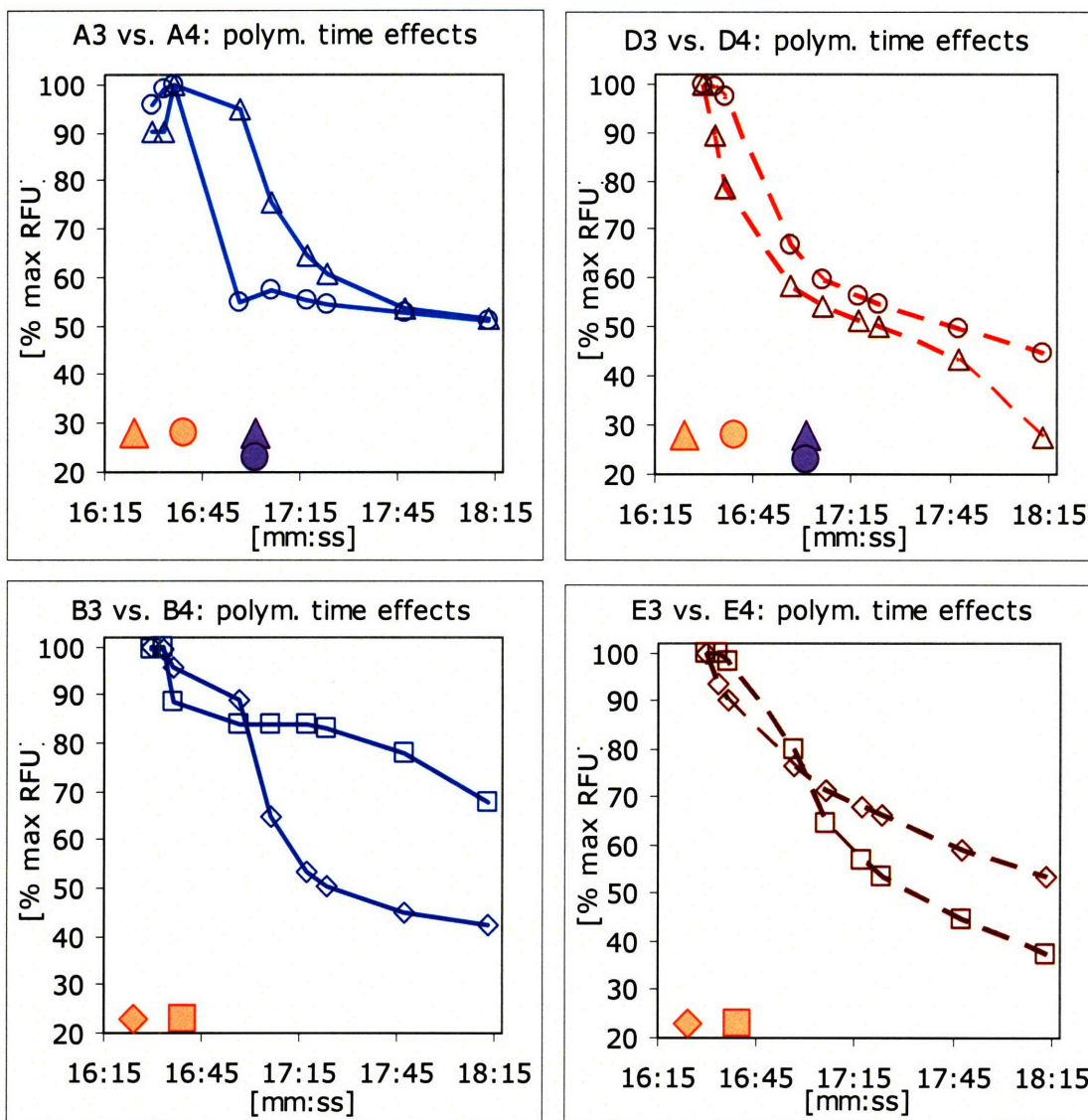


Figure 44. Effects of polymerization time on fluorescence. Vertical orange lines indicate time of TEMED addition. Well sample's marker shape (e.g. triangle) corresponds to the orange marker at which point TEMED was added (e.g. orange triangle).

The A3/A4 comparison in Figure 44 shows a spike in A3 followed by a gradual drop. This is probably due to the sudden pH increase upon addition of TEMED, followed by the detrimental effects of high concentrations of ammonium persulfate. Surprisingly, A4, indicates a sharp drop after the addition of TEMED. This seeming lack of a spike is

probably due to a lack of data points immediately following the addition. The well A4 was expected to behave like A3, except about 30 seconds delayed. The fact that A3 drops in fluorescence faster than A4 indicates possible problems that might be addressed with a larger sample size and/or an apparatus with a more meticulous procedural control. The need for a better setup is again suggested in the comparison of B3 and B4, where the fluorescence behavior appears to take on qualitatively independent processes. The profile of B4 suggests an extra source of basic material that was accidentally added to the well, so that the buffer system was better able to control the drop in pH (that causes the drop in fluorescence).

The comparison between D3 and D4 suggests that the polymerization time on the order of 30 seconds does make a difference. D4's fluorescence activity appears to be delayed by the difference in TEMED addition time. However, E3 and E4 indicate that the situation is not so easily understood. In light of all four comparisons, the contradictory indications suggest that there are other factors that affect the polymerization velocity on the order of 30 seconds.

The wells compared above can be rearranged to see how shearing-by-syringe can affect the fluorescence activity of the gel. In other words, there are four pairs of comparisons that can be made to see how shearing could affect fluorescence. These comparisons are summarized in Table 16.

Table 16. Shearing and fluorescence activity. Each pair of wells have the same conditions, except for the fact that the first of the pair had been subjected to shearing by a Hamilton syringe.

	A3 vs. B3	A4 vs. B4	D3 vs. E3	D4 vs. E4
acrylamide	both	both	both	both
GFP	both	both	both	both
AA NHS E	both	both	neither	neither
TEMED	concurrent	concurrent	concurrent	concurrent
shearing	yes vs. no	yes vs. no	yes vs. no	yes vs. no

Rearranging the dynamic fluorescence profiles results in the four comparison charts that make up Figure 45. In A3 vs. B3, the shearing has occurred at the purple line for A3. However, the drop in fluorescence for the two are comparable. Clearly, control of the pH is an issue that must be dealt with in further experiments. The A4 vs. B4 chart and the D3 vs. E3 chart indicate a large divergence that occurs prior to the key shearing step. This suggests that there are other factors, such as mixing efficiency, that play a role in influencing fluorescence activity. Finally, the D4-E4 comparison shows no sign of shearing effects, but this was expected because none of the GFP's in that comparison have any vinyl groups that can readily undergo radical polymerization with the polyacrylamide chains in the surroundings. The fact that shearing doesn't appear to have any effects on the fluorescence suggests that perhaps there are theoretical reasons why unraveling GFP with shear isn't working here. One possibility is that the polymer solution might be acting as a non-Newtonian fluid that undergoes viscosity changes with shear rate. Shear-thinning materials like polymers can, under sufficient flowrates, develop a plug-flow-like velocity profile. Thus, much of the material is insulated from the effects of the macroscopic forces involved in pushing the polymer solution through the syringe needle. This may mean that another design is needed. For example, a glass

surface with many immobilized GFP's might be forced to experience lubrication layer flow by a sufficiently pressured, thin layer of polymer solution. In effect, the polymer will flow away from the center toward the edges (or other openings) of the apparatus, and while much of the polymer will experience bulk-like flow (due to shear-thinning effects), the macroscopic forces can then be focused at the location where they matter most – at the surface, where most of the GFP are immobilized.

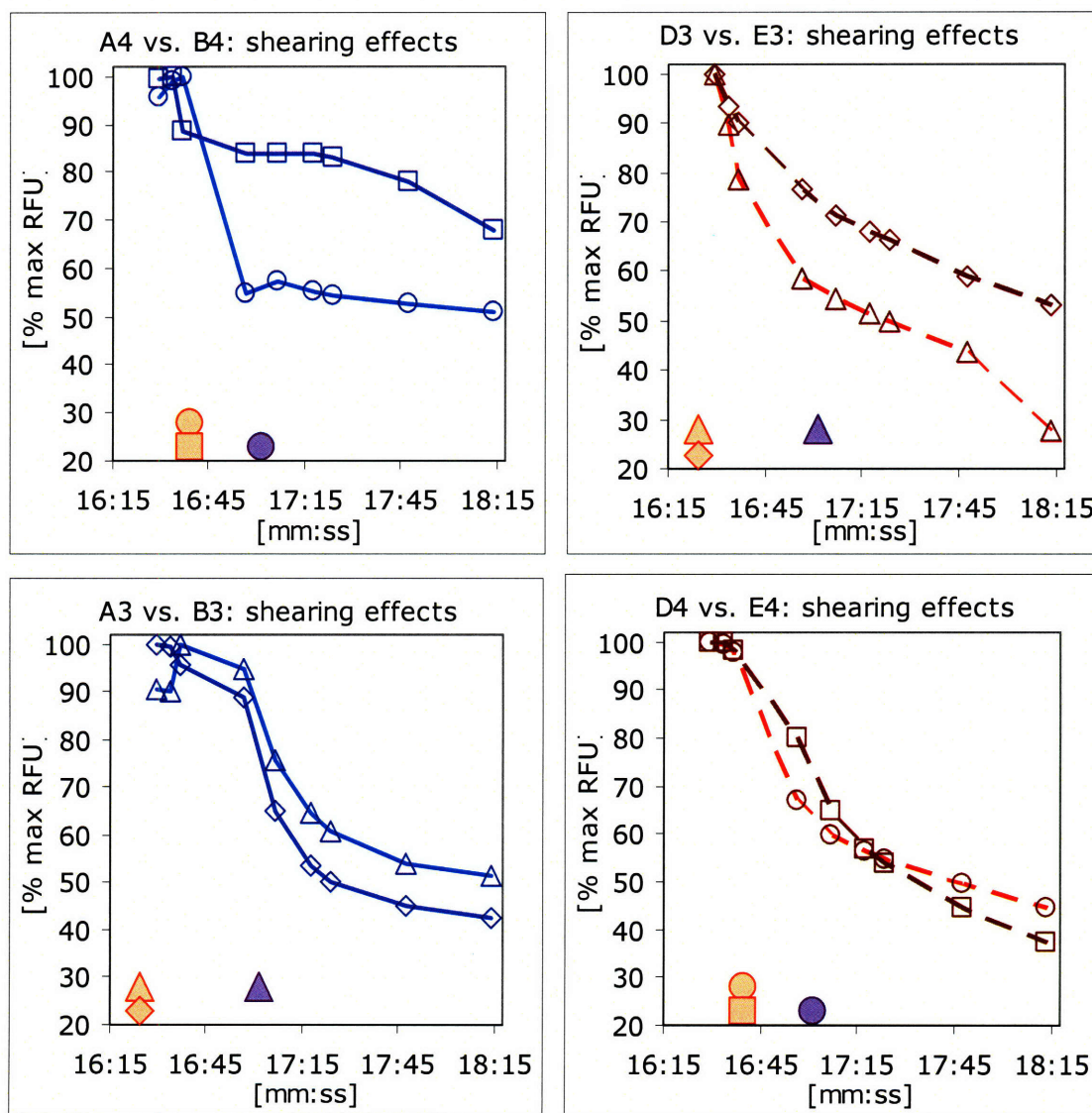


Figure 45. Effects of syringe-shearing on fluorescence.

The final question that was explored with the eight wells was whether acrylic acid NHS ester had any effect on the ability to impose macroscopic forces on the fluorescent proteins. The comparisons made are summarized in Table 17 and depicted in Figure 46.

Table 17. Acrylic acid linkage and fluorescence activity. Each pair of wells share the same conditions, except that only one of the two wells have GFP that were subjected to vinyl group additions by NHS chemistry.

	A3 vs. D3	B3 vs. E3	A4 vs. D4	B4 vs. E4
acrylamide	both	both	both	both
GFP	both	both	both	both
AA NHS E	yes vs. no	yes vs. no	yes vs. no	yes vs. no
TEMED	concurrent	concurrent	concurrent	concurrent
shearing	both	neither	both	neither

Because an addition of a vinyl group would enable GFP to covalently link to the polyacrylamide network, this should have some effect on how much stress GFP can be forced to experience. However, the dynamic fluorescence data in this experiment have variabilities that need to be controlled for before the effects of covalent linking can become apparent. Moreover, the polymer is a complex network of chains; while stoichiometrically-derived estimations of structure may be possible, the depiction of a more refined architecture with a clear, unrestricted placement of fluorescent proteins appears to be difficult to envision and communicate, and perhaps impossible to implement with today's chemical technology. Because of these complexities that are not controllable, even a macroscopically precise experimental system may be insufficient to control the placement of fluorescent proteins for the purpose of constructing a system that can manifest the effects of covalent linkages. The feasibility of studying the effects of covalent links depends critically on simplifying the experimental system; the polymer structure is probably not the best place to begin to figure out how to make green fluorescent proteins respond mechanically.

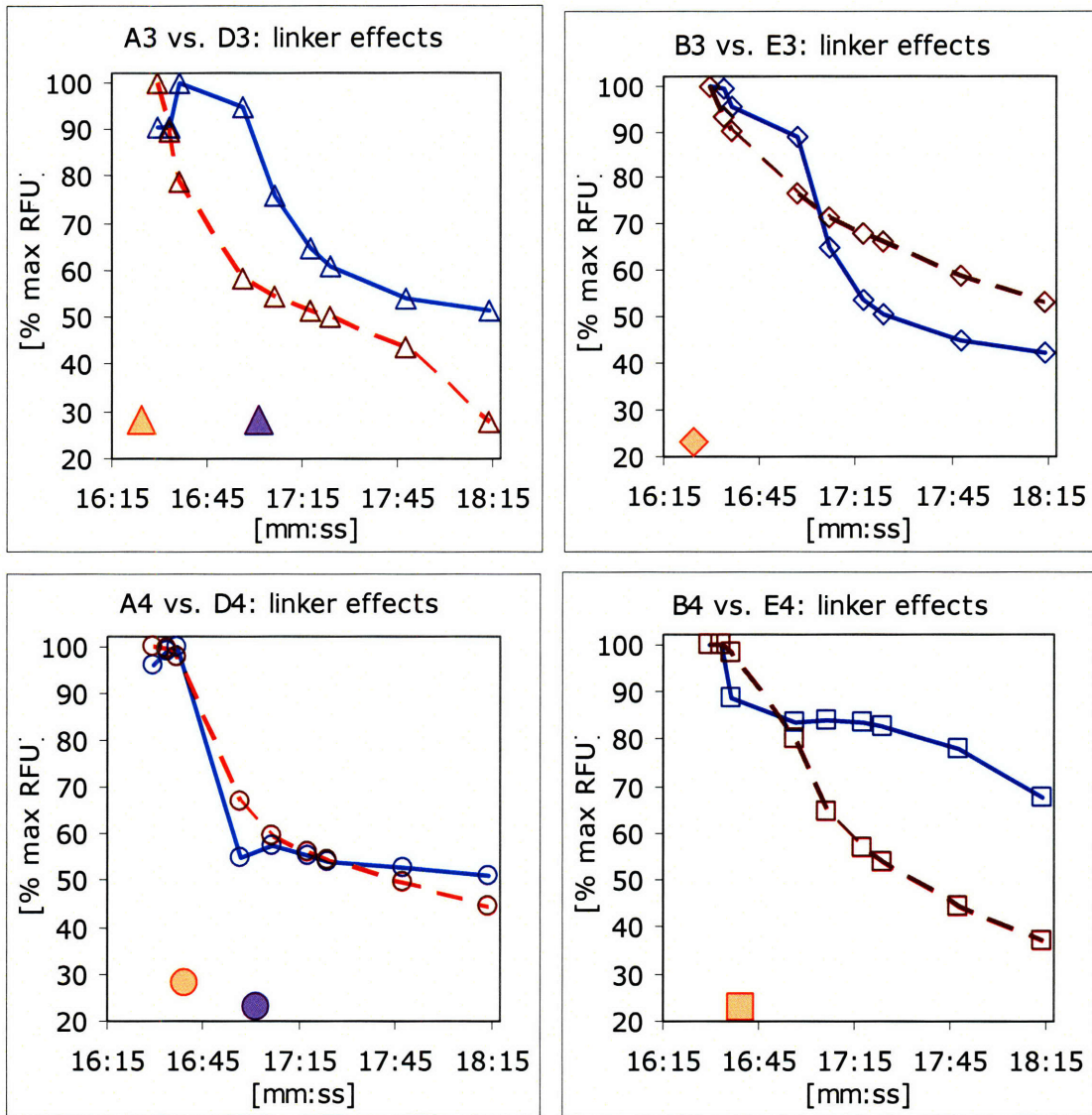


Figure 46. Effects of linker chemistry on fluorescence activity.

Summary

MS data shows that at least three vinyl groups can be attached to GFP without a radical shift in the pH. The green fluorescent protein appears to chemically link with the acrylamide hydrogel, but pH control is an issue. GFP can survive the polymerization

process. Further efforts in using a polymer scaffold for the mechanical study of GFP revealed that pH control was an important factor to maintain GFP fluorescence. A well-characterized, highly controlled system seems to be required to connect the “micro” forces to the “macro” forces.

Methods

Incorporation of EDC-conjugated GFP in polyacrylamide

EDC-enabled conjugation of acrylamide(AAm) to GFP was done with protein-hapten conjugation protocols as guides. **Conjugation Buffer (CB) consisted of.** A 100:1 ratio of AAm:GFP, and a 10:1 ratio of EDC:AAm were targeted. The “protein volume” of 200 μ L CB with 2mg GFP and a “hapten volume” of 500 μ L with 0.125mg AAm were prepared. EDC was prepared at 0.67mg/100 μ L, and 50 μ L were used immediately in the “protein-hapten” mixture. The reaction volume was then kept out of light for 2 hours at room temperature.

A 4% bis/acrylamide gel was used to encase the AAm-GFP in one 10mL beaker, and GFP in the other 10mL beaker. After macrogel formation, 500 μ L CB was added to each and both were stored at 4C for one week.

After one week, 2mL CB was added to each, and supernatant samples were taken. Fluorescence activity was measured at 475nm excitation and 509nm emission. The fluid portion of each beaker was removed and new buffer was added. This process was repeated to measure the amount of leeching off of the gel.

Imparting shearing force on gel with GFP-acrylate

27.6 mg of acrylic acid NHS ester (ANE) was added to 1.3mL 10X PBS. The pH was adjusted back to pH 7.5-8. About 287 μ L ANE solution was added to 9.6 μ L GFP stock solution. Incubation at room temperature was at least 2 hours. The prepared GFP-acrylate was then compared against GFP. Samples from each were included in a polymerization of 7.5% acrylamide. The samples were sheared with Hamilton syringes repeatedly, and periodic RFU measurements were made.

For a table perspective of well compositions, see Table 18.

Table 18. Well compositions for the syring-shearing experiments. Asterisks indicate that pH was subsequently adjusted. For the column titled #17, a GFP solution of 9.6 μ L and an acrylic acid NHS ester solution of 287 μ L were mixed together in a prior preparatory step. #17b is essentially the experimental group. For the column marked #18, a GFP solution of 9.6 μ L was mixed with a 10X PBS solution of 287 μ L in a preparatory step. The acrylic acid NHS ester solution was made at 21 mg/mL in 10X PBS, where the pH was adjusted back to the range of 7.5-8 after solvation. #18b doesn't have acrylic acid NHS ester, and #19b1/2 are just polyacrylamides. #19b1 and #19b2 have almost the same composition. The volumes are "per well" values. Actual batches were about 5 times the listed values.

	#17b	#18b	#19b1	#19b2
GFP/ANE	29.7 uL	0	0	0
GFP	0	29.7 uL	0	0
30% AAm*	60	60	0	60
7.5% AAm*	0	0	240.0	0
10X PBS*	150.0	150.0	0	179.7
APS*	10.0	10.0	10.0	10.0
Notes	Acrylic Acid, GFP, PAM	GFP, PAM	PAM	PAM
Wells filled	A3, A4; B3, B4.	D3, D4; E3, E4.	G3, G4.	H3, H4.

*pH adjusted

Because pH issues were a concern, pH was measured and adjusted prior to the addition of TEMED. In the case of well A3, the pH was at 5.5 and was adjusted to 9.5-10 before the addition of TEMED. Shearing of column 3 (A3, B3, D3, E3) occurred prior to t1. Shearing of column 4 (A4, B4, D4, E4) between t3 and t4.

Table 19. Schematic of wells and design of experiment. Rows A and B contained hydrogel with GFP-acrylate. Rows D and E contained hydrogel with GFP. Prior to the addition of TEMED, the pH was

checked and adjusted for key wells (prior pH / μ L 12M NaOH added / resulting pH). BL=10XPBS only.
 For explanation of times see figure associated with the syringe experiment.

	3	4	type of GFP added to row
A	5.5/1/9.5-10	na/0.5/7	GFP-acrylate
B	na/0.5/7	na/0.5/8	GFP-acrylate
C	na(BL)	na(BL)	
D	8/0/8*	na	GFP(ctrl)
E	na	na	GFP(ctrl)
F	8/0/8*(BL)	8/0/8*(BL)	
TEMED	prior to t1	between t3 and t4	

Chapter 4. Conclusion

All organisms interact mechanically with their environment, but can these interactions have significance on par with the traditionally examined biochemistry of life? In other words, when one studies biological systems at the small length-scales accessible to biochemistry, can mechanical interactions make non-negligible contributions to the diagnosis of state and the prognosis of future behavior that have been traditionally dominated by chemical analysis? Such questions were addressed in increasing detail, and the limitations encountered clarified the need for an intracellular mechanical sensor. The candidate sensor examined here is the green fluorescent protein (GFP), whose potential as a mechanical sensor depends on a solid theoretical foundation. The discussion of theory began with the early contributions in chemical kinetics by Arrhenius and Eyring. By combining their work with that of numerous others, the two-state Markovian model was developed sufficiently to analyze velocity-clamp and force-clamp data in single-molecule experiments. However, while the underlying theory is able to describe a multitude of phenomena, the need to account for subtle conformational changes that may affect fluorescence behavior requires one to go beyond this versatile but simple framework. To this end, molecular dynamics simulations revealed interesting details of the GFP unfolding process, such as the axis-dependent unfolding behavior, and the exchanges of energies between subcomponents of the molecule.

At the same time, the parameters required for a macroscopic scaffold to impose tension on nanoscale structures were examined. Signal-to-noise issues were addressed in terms of Flory-Stockmayer gelation theory, and the measurement of signal variation on

an inverted fluorescence microscope. Polyacrylamide proved to be a difficult substance to attach to GFP, because the description and control of meso-scale architecture in this context requires yet-to-occur developments in basic polymer research. In other words, a polymer-based calibration of intracellular mechanical sensors must await further developments in polymer chemistry, protein mechanics, as well as a solid theoretical foundation in order to satisfactorily address even simple questions such as, “when fluorescence signal changes occur in a biological experiment, what does that mean?” In the meantime, however, one can still examine what information can be presently gleaned from a cellular force-fluorescence experiment.

Fluorescence data can be categorized into static and dynamic data. Dynamic data, as in the force-clamp experiments, can be used to derive kinetic and thermodynamic property values. However, such dynamic data collection requires a precise control of the experimental system that can rarely be achieved outside the context of single molecule experiments and computer simulations. While molecular dynamics simulations were done in anticipation of dealing with dynamic data inside cells in the future, for now the equilibrated system will be considered. As mentioned before, equilibrium is a function of force.

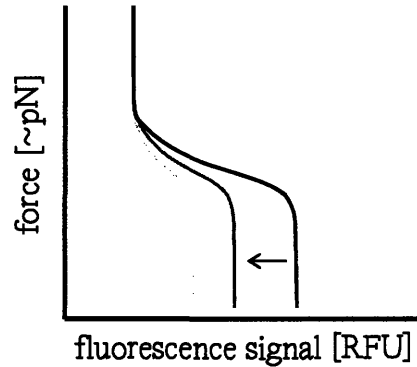
$$K_{eq}(f) = K_{eq}(0) \exp\left(\frac{f\Delta X}{k_B T}\right)$$

16) Equilibrium under force.

This dependence is expected to result in force-fluorescence curves depicted in

Figure 47.

Figure 47. Expected force-fluorescence curve. Black curve indicate initial expected average signal, dependent on the magnitude of constant force application. Gray and light gray curves represent experiments with varying degrees of photobleaching. The sensitivity of equilibrium to force near $K_{eq} = 1$ means that molecular force measurement requires sophistication beyond ideas of simple threshold values.



When a two-state Markovian system experiences a

weak force, under practical duration times, the effect will be negligible compared to other phenomena such as photobleaching. However, as force increases, the equilibrium shifts towards the previously rare conformation. In practice, the change in signal with respect to maximum potential signal change will indicate the relative durations that a molecule is spending in the two conformations. As force increases beyond the “threshold region,” the molecule will spend more and more of its time in the previously rare state. As mentioned earlier, one must take into account the effect of photobleaching, which will probably manifest as a decreasing maximum signal change, as depicted by the gray curves in Figure 47. In the case of a Forster Resonance Energy Transfer experiment, the photobleaching-induced drift may affect both the high and low signal values.

To speculate beyond the equilibrated, two-state Markovian model, one might consider a three-state system, or a more complex, continuously changing input of force. Coming back to the question of the meaning of fluorescence signal change, under the current discussion the signal can be related to force if one records signal durations and averages the intensity across time, and normalizes the raw signal value against the maximum signal change, which is a function of photobleaching.

Once a mechanical sensor can be calibrated and deployed, intracellular mechanics is a topic of study that is ready to take off. Discoveries made in this arena will bring about a more quantified, complex perspective of the cytoplasm. Cellular mechanical understanding will then lead to an improved comprehension of disease processes. In the future, there may be a time when one can make insights in medicine by examining the cytoskeletal architecture of biopsy samples.

References

- Aoshiba, K., Rennard, S. I., and Spurzem, J. R. (1997). Cell-matrix and cell-cell interactions modulate apoptosis of bronchial epithelial cells. *Am J Physiol* 272, L28-37.
- Apetri, A. C., Maki, K., Roder, H., and Surewicz, W. K. (2006). Early Intermediate in Human Prion Protein Folding As Evidenced by Ultrarapid Mixing Experiments. *J Am Chem Soc* 128, 11673-11678.
- Apetri, A. C., and Surewicz, W. K. (2002). Kinetic Intermediate in the Folding of Human Prion Protein
10.1074/jbc.C200507200. *J Biol Chem* 277, 44589-44592.
- Arai, R., Ueda, H., Kitayama, A., Kamiya, N., and Nagamune, T. (2001). Design of the linkers which effectively separate domains of a bifunctional fusion protein. *Protein Eng* 14, 529-532.
- Bai, L., Santangelo, T. J., and Wang, M. D. (2006). Single-molecule analysis of RNA polymerase transcription. *Annu Rev Biophys Biomol Struct* 35, 343-360.
- Baldini, G., Cannone, F., and Chirico, G. (2005). Pre-Unfolding Resonant Oscillations of Single Green Fluorescent Protein Molecules
10.1126/science.1115001. *Science* 309, 1096-1100.
- Bao, G., and Suresh, S. (2003). Cell and molecular mechanics of biological materials. *Nat Mater* 2, 715-725.
- Barondeau, D. P., Kassmann, C. J., Tainer, J. A., and Getzoff, E. D. (2005). Understanding GFP chromophore biosynthesis: controlling backbone cyclization and modifying post-translational chemistry. *Biochemistry* 44, 1960-1970.
- Bell, A. F., Stoner-Ma, D., Wachter, R. M., and Tonge, P. J. (2003). Light-driven decarboxylation of wild-type green fluorescent protein. *Journal of the American Chemical Society* 125, 6919-6926.
- Bell, G. I. (1978). Models for the specific adhesion of cells to cells. *Science* 200, 618-627.
- Ben-Haim, Y. (1952). Robust reliability in the mechanical sciences).
- Benoit, M., Gabriel, D., Gerisch, G., and Gaub, H. E. (2000). Discrete interactions in cell adhesion measured by single-molecule force spectroscopy. 2, 313-317.
- Bernas, T., Zarebski, M., Dobrucki, J. W., and Cook, P. R. (2004). Minimizing photobleaching during confocal microscopy of fluorescent probes bound to chromatin: role of anoxia and photon flux. *J Microsc* 215, 281-296.
- Beyer, M. K. (2000). The mechanical strength of a covalent bond calculated by density functional theory. *The Journal of Chemical Physics* 112, 7307-7312.
- Borgia, A., Bonivento, D., Travaglini-Allocatelli, C., Di Matteo, A., and Brunori, M. (2006). Unveiling a Hidden Folding Intermediate in c-Type Cytochromes by Protein Engineering
10.1074/jbc.M512127200. *J Biol Chem* 281, 9331-9336.
- Bragg, P. D., and Hou, C. (1975). Subunit composition, function, and spatial arrangement in the Ca²⁺- and Mg²⁺-activated adenosine triphosphatases of *Escherichia coli*

- and *Salmonella typhimurium*. *Archives of Biochemistry and Biophysics* *167*, 311-321.
- Brejč, K., Sixma, T. K., Kitts, P. A., Kain, S. R., Tsien, R. Y., Ormo, M., and Remington, S. J. (1997). Structural basis for dual excitation and photoisomerization of the *Aequorea victoria* green fluorescent protein. *Proc Natl Acad Sci U S A* *94*, 2306-2311.
- Brockwell, D. J., Beddard, G. S., Paci, E., West, D. K., Olmsted, P. D., Smith, D. A., and Radford, S. E. (2005). Mechanically unfolding the small, topologically simple protein L. *Biophys J* *89*, 506-519.
- Brockwell, D. J., Paci, E., Zinober, R. C., Beddard, G. S., Olmsted, P. D., Smith, D. A., Perham, R. N., and Radford, S. E. (2003). Pulling geometry defines the mechanical resistance of a beta-sheet protein. *Nat Struct Biol* *10*, 731-737.
- Bustamante, C., Marko, J. F., Siggia, E. D., and Smith, S. (1994). Entropic elasticity of lambda-phage DNA. *Science* *265*, 1599-1600.
- Carraway, K. L., and Koshland, D. E., Jr. (1968). Reaction of tyrosine residues in proteins with carbodiimide reagents. *Biochim Biophys Acta* *160*, 272-274.
- Carraway, K. L., and Triplett, R. B. (1970). Reaction of carbodiimides with protein sulfhydryl groups. *Biochim Biophys Acta* *200*, 564-566.
- Carrion-Vazquez, M., Li, H., Lu, H., Marszalek, P. E., Oberhauser, A. F., and Fernandez, J. M. (2003). The mechanical stability of ubiquitin is linkage dependent. *Nat Struct Biol* *10*, 738-743.
- Carrion-Vazquez, M., Oberhauser, A. F., Fowler, S. B., Marszalek, P. E., Broedel, S. E., Clarke, J., and Fernandez, J. M. (1999). Mechanical and chemical unfolding of a single protein: a comparison. *Proc Natl Acad Sci U S A* *96*, 3694-3699.
- Cattaruzza, M., Lattrich, C., and Hecker, M. (2004). Focal adhesion protein zyxin is a mechanosensitive modulator of gene expression in vascular smooth muscle cells. *Hypertension* *43*, 726-730.
- Cecconi, C., Shank, E. A., Bustamante, C., and Marqusee, S. (2005). Direct Observation of the Three-State Folding of a Single Protein Molecule [10.1126/science.1116702](https://doi.org/10.1126/science.1116702). *Science* *309*, 2057-2060.
- Chattoraj, M., King, B. A., Bublitz, G. U., and Boxer, S. G. (1996). Ultra-fast excited state dynamics in green fluorescent protein: multiple states and proton transfer. *Proc Natl Acad Sci U S A* *93*, 8362-8367.
- Chen, J., Fabry, B., Schiffrin, E. L., and Wang, N. (2001). Twisting integrin receptors increases endothelin-1 gene expression in endothelial cells. *Am J Physiol Cell Physiol* *280*, C1475-1484.
- Chicurel, M. E., Chen, C. S., and Ingber, D. E. (1998). Cellular control lies in the balance of forces. *Curr Opin Cell Biol* *10*, 232-239.
- Chirico, G., Diaspro, A., Cannone, F., Collini, M., Bologna, S., Pellegrini, V., and Beltram, F. (2005). Selective fluorescence recovery after bleaching of single E2GFP proteins induced by two-photon excitation. *Chemphyschem* *6*, 328-335.
- Choquet, D., Felsenfeld, D. P., and Sheetz, M. P. (1997). Extracellular matrix rigidity causes strengthening of integrin-cytoskeleton linkages. *Cell* *88*, 39-48.
- Clasen, C., Gearing, B. P., and McKinley, G. H. (2006). The flexure-based microgap rheometer (FMR) [10.1122/1.2357190](https://doi.org/10.1122/1.2357190). *Journal of Rheology* *50*, 883-905.

- Clasen, C., Kojic, N., Kavehpour, H. P., and McKinley, G. H. (2004). Microrheometry: Gap-Dependent Rheology and Tribology of Complex Fluids. Paper presented at: Proc. XIVth Int. Congr. on Rheology (Seoul, Korea, The Korean Society of Rheology).
- Consortium, G. O. (2000). Gene Ontology: tool for the unification of biology (<http://www.geneontology.org/>). *Nature Genetics* 25, 25-29.
- Consortium, G. O. (2006) [geneontology.org](http://www.geneontology.org), Internet site.
- Creemers, T. M., Lock, A. J., Subramaniam, V., Jovin, T. M., and Volker, S. (2000a). Photophysics and optical switching in green fluorescent protein mutants. *Proc Natl Acad Sci U S A* 97, 2974-2978.
- Creemers, T. M. H., Lock, A. J., Subramaniam, V., Jovin, T. M., and Volker, S. (2000b). Photophysics and optical switching in green fluorescent protein mutants 10.1073/pnas.050365997. *PNAS* 97, 2974-2978.
- Critchley, D. R. (2000). Focal adhesions - the cytoskeletal connection. *Curr Opin Cell Biol* 12, 133-139.
- Critchley, D. R. (2004). Cytoskeletal proteins talin and vinculin in integrin-mediated adhesion. *Biochem Soc Trans* 32, 831-836.
- Critchley, D. R. (2005). Genetic, biochemical and structural approaches to talin function. *Biochem Soc Trans* 33, 1308-1312.
- Cuatrecasas, P., and Parikh, I. (1972). Adsorbents for affinity chromatography. Use of N-hydroxysuccinimide esters of agarose. *Biochemistry* 11, 2291-2299.
- Deen, W. M. (1998). *Analysis of transport phenomena* (New York, Oxford University Press).
- Dewey, C. F., Jr., Bussolari, S. R., Gimbrone, M. A., Jr., and Davies, P. F. (1981). The dynamic response of vascular endothelial cells to fluid shear stress. *J Biomech Eng* 103, 177-185.
- Dietz, H., and Rief, M. (2004a). Exploring the energy landscape of GFP by single-molecule mechanical experiments. *Proc Natl Acad Sci U S A* 101, 16192-16197.
- Dietz, H., and Rief, M. (2004b). Exploring the energy landscape of GFP by single-molecule mechanical experiments 10.1073/pnas.0404549101. *PNAS* 101, 16192-16197.
- Discher, D. E., Janmey, P., and Wang, Y.-I. (2005). Tissue Cells Feel and Respond to the Stiffness of Their Substrate 10.1126/science.1116995. *Science* 310, 1139-1143.
- Doherty, E. A. S., Meagher, R. J., Albarghouthi, M. N., and Barron, A. E. (2003). Microchannel wall coatings for protein separations by capillary and chip electrophoresis. *ELECTROPHORESIS* 24, 34-54.
- Edgerton, V. R., and Roy, R. R. (1994). Neuromuscular adaptation to actual and simulated weightlessness. *Adv Space Biol Med* 4, 33-67.
- Engler, A., Bacakova, L., Newman, C., Hategan, A., Griffin, M., and Discher, D. (2004). Substrate compliance versus ligand density in cell on gel responses. *Biophys J* 86, 617-628.
- Engler, A. J., Sen, S., Sweeney, H. L., and Discher, D. E. (2006). Matrix elasticity directs stem cell lineage specification. *Cell* 126, 677-689.
- Evans, E., Berk, D., and Leung, A. (1991). Detachment of agglutinin-bonded red blood cells. I. Forces to rupture molecular-point attachments. *Biophys J* 59, 838-848.

- Evans, E., and Yeung, A. (1989). Apparent viscosity and cortical tension of blood granulocytes determined by micropipet aspiration. *Biophys J* 56, 151-160.
- Even-Ram, S., Artym, V., and Yamada, K. M. (2006). Matrix control of stem cell fate. *Cell* 126, 645-647.
- Falconnet, D., Csucs, G., Michelle Grandin, H., and Textor, M. (2006). Surface engineering approaches to micropattern surfaces for cell-based assays. *Biomaterials* 27, 3044-3063.
- Fowler, S. B., Best, R. B., Toca Herrera, J. L., Rutherford, T. J., Steward, A., Paci, E., Karplus, M., and Clarke, J. (2002). Mechanical unfolding of a titin Ig domain: structure of unfolding intermediate revealed by combining AFM, molecular dynamics simulations, NMR and protein engineering. *J Mol Biol* 322, 841-849.
- Fritz, J., Katopodis, A. G., Kolbinger, F., and Anselmetti, D. (1998). Force-mediated kinetics of single P-selectin/ligand complexes observed by atomic force microscopy
10.1073/pnas.95.21.12283. *PNAS* 95, 12283-12288.
- Fujisawa, T., Hattori, T., Takahashi, K., Kuboki, T., Yamashita, A., and Takigawa, M. (1999). Cyclic Mechanical Stress Induces Extracellular Matrix Degradation in Cultured Chondrocytes via Gene Expression of Matrix Metalloproteinases and Interleukin-1. *J Biochem (Tokyo)* 125, 966-975.
- Galbraith, C. G., and Sheetz, M. P. (1997). A micromachined device provides a new bend on fibroblast traction forces
10.1073/pnas.94.17.9114. *PNAS* 94, 9114-9118.
- Gerstein, M., Lesk, A. M., and Chothia, C. (1994). Structural mechanisms for domain movements in proteins. *Biochemistry* 33, 6739-6749.
- Gilles, M. A., Hudson, A. Q., and Borders, C. L., Jr. (1990). Stability of water-soluble carbodiimides in aqueous solution. *Anal Biochem* 184, 244-248.
- Gillespie, P. G., and Walker, R. G. (2001). Molecular basis of mechanosensory transduction. *413*, 194-202.
- Goldmann, W. H. (2002). Mechanical aspects of cell shape regulation and signaling. *Cell Biol Int* 26, 313-317.
- Grandbois, M., Beyer, M., Rief, M., Clausen-Schaumann, H., and Gaub, H. E. (1999). How Strong Is a Covalent Bond?
10.1126/science.283.5408.1727. *Science* 283, 1727-1730.
- Grater, F., Shen, J., Jiang, H., Gautel, M., and Grubmuller, H. (2004). Mechanically induced titin kinase activation studied by force probe molecular dynamics simulations
10.1529/biophysj.104.052423. *Biophys J*, biophysj.104.052423.
- Grey, M. J., Tang, Y., Alexov, E., McKnight, C. J., Raleigh, D. P., and Palmer, A. G., 3rd (2006). Characterizing a partially folded intermediate of the villin headpiece domain under non-denaturing conditions: contribution of His41 to the pH-dependent stability of the N-terminal subdomain. *J Mol Biol* 355, 1078-1094.
- Guardiani, C., and Bagnoli, F. (2006). A toy model of polymer stretching. *J Chem Phys* 125, 084908.
- Harris, A., Wild, P., and Stopak, D. (1980). Silicone rubber substrata: a new wrinkle in the study of cell locomotion
10.1126/science.6987736. *Science* 208, 177-179.

- Heim, R., Prasher, D. C., and Tsien, R. Y. (1994). Wavelength mutations and posttranslational autoxidation of green fluorescent protein. *Proc Natl Acad Sci U S A* *91*, 12501-12504.
- Higgs, H. N. (2005). Formin proteins: a domain-based approach. *Trends Biochem Sci* *30*, 342-353.
- Hoppmann II, W. H., and Miller, C. E. (1963). Rotational Fluid Flow Generator for Studies in Rheology. *Journal of Rheology* *7*, 181-193.
- Hou, Y. Y., and Kassim, H. O. (2005). Instrument techniques for rheometry. *Review of Scientific Instruments* *76*, 101101-101119.
- Huang, C.-R. (1971a). Determination of the Shear Rates of Non-Newtonian Fluids from Rotational Viscometric Data. I. Concentric Cylinder Viscometer. *Journal of Rheology* *15*, 25-30.
- Huang, C.-R. (1971b). Determination of the Shear Rates of Non-Newtonian Fluids from Rotational Viscometric Data. II. Cone-and-Plate Viscometer. *Journal of Rheology* *15*, 31-37.
- Huang, S., and Ingber, D. E. (2005). Cell tension, matrix mechanics, and cancer development. *Cancer Cell* *8*, 175-176.
- Humphrey, W., Dalke, A., and Schulten, K. (1996). VMD: visual molecular dynamics. *J Mol Graph* *14*, 33-38, 27-38.
- Ingber, D. E. (2003). Tensegrity I. Cell structure and hierarchical systems biology. *J Cell Sci* *116*, 1157-1173.
- Ingber, D. E. (2006). Cellular mechanotransduction: putting all the pieces together again. *Faseb J* *20*, 811-827.
- Jung, G., Wiehler, J., and Zumbusch, A. (2005). The photophysics of green fluorescent protein: influence of the key amino acids at positions 65, 203, and 222. *Biophys J* *88*, 1932-1947.
- Kadmas, J. L., and Beckerle, M. C. (2004). The LIM domain: from the cytoskeleton to the nucleus. *Nat Rev Mol Cell Biol* *5*, 920-931.
- Katsumi, A., Orr, A. W., Tzima, E., and Schwartz, M. A. (2004). Integrins in mechanotransduction. *J Biol Chem* *279*, 12001-12004.
- Kavehpour, H. P., and McKinley, G. H. (2004). Tribo-Rheometry: From Gap-Dependent Rheology to Tribology. *Tribology Letters* *V17*, 327-335.
- Kienberger, F., Kada, G., Gruber, H. J., Pastushenko, V. P., Riener, C., Trieb, M., Knaus, H.-G., Schindler, H., and Hinterdorfer, P. (2000). Recognition Force Spectroscopy Studies of the NTA-His6 Bond. *Single Molecules* *1*, 59-65.
- Kolin, D. L., Costantino, S., and Wiseman, P. W. (2006). Sampling effects, noise, and photobleaching in temporal image correlation spectroscopy. *Biophys J* *90*, 628-639.
- Kummer, A. D., Kompa, C., Lossau, H., Pollinger-Dammer, F., Michel-Beyerle, M. E., Silva, C. M., Bylina, E. J., Coleman, W. J., Yang, M. M., and Youvan, D. C. (1998). Dramatic reduction in fluorescence quantum yield in mutants of Green Fluorescent Protein due to fast internal conversion. *Chemical Physics* *237*, 183-193.
- Kummer, A. D., Kompa, C., Niwa, H., Hirano, T., Kojima, S., and Michel-Beyerle, M. E. (2002). Viscosity-Dependent Fluorescence Decay of the GFP Chromophore in Solution Due to Fast Internal Conversion. *The journal of physical chemistry B*

- Condensed matter materials surfaces interfaces & biophysical. 106, 7554 (7556 pages).*
- Lappalainen, P., Kessels, M. M., Cope, M. J. T. V., and Drubin, D. G. (1998). The ADF Homology (ADF-H) Domain: A Highly Exploited Actin-binding Module. *Mol Biol Cell* *9*, 1951-1959.
- Laurent, S., Boutouyrie, P., and Lacolley, P. (2005). Structural and Genetic Bases of Arterial Stiffness
10.1161/01.HYP.0000164580.39991.3d. *Hypertension* *45*, 1050-1055.
- Lee, H., Scherer, N. F., and Messersmith, P. B. (2006). Single-molecule mechanics of mussel adhesion
10.1073/pnas.0605552103. *PNAS* *103*, 12999-13003.
- Lehoux, S., Castier, Y., and Tedgui, A. (2006). Molecular mechanisms of the vascular responses to haemodynamic forces. *J Intern Med* *259*, 381-392.
- Lehoux, S., and Tedgui, A. (2003). Cellular mechanics and gene expression in blood vessels. *J Biomech* *36*, 631-643.
- Li, F., Redick, S. D., Erickson, H. P., and Moy, V. T. (2003). Force Measurements of the $\alpha_5\beta_1$ Integrin-Fibronectin Interaction. *Biophys J* *84*, 1252-1262.
- Li, P. T., Collin, D., Smith, S. B., Bustamante, C., and Tinoco, I., Jr. (2006). Probing the mechanical folding kinetics of TAR RNA by hopping, force-jump, and force-ramp methods. *Biophys J* *90*, 250-260.
- Liphardt, J., Onoa, B., Smith, S. B., Tinoco, I. J., and Bustamante, C. (2001). Reversible unfolding of single RNA molecules by mechanical force. *Science* *292*, 733-737.
- Lomant, A. J., and Fairbanks, G. (1976). Chemical probes of extended biological structures: Synthesis and properties of the cleavable protein cross-linking reagent [35S]dithiobis(succinimidyl propionate). *Journal of Molecular Biology* *104*, 243-261.
- Luengo, G., Israelachvili, J., and Granick, S. (1996). Generalized effects in confined fluids: New friction map for boundary lubrication. *Wear* *200*, 328-335.
- Luengo, G., Israelachvili, J., and Granick, S. (1997). Erratum. *Wear* *205*, 246.
- Maddalo, S. L., and Zimmer, M. (2005). The Role of the Protein Matrix in GFP Fluorescence. *Photochem Photobiol.*
- Matthews, B. D., Overby, D. R., Alenghat, F. J., Karavitis, J., Numaguchi, Y., Allen, P. G., and Ingber, D. E. (2004). Mechanical properties of individual focal adhesions probed with a magnetic microneedle. *Biochem Biophys Res Commun* *313*, 758-764.
- McKinley, G. H., and Sridhar, T. (2002). FILAMENT-STRETCHING RHEOMETRY OF COMPLEX FLUIDS
doi:10.1146/annurev.fluid.34.083001.125207. *Annual Review of Fluid Mechanics* *34*, 375-415.
- McKinley, G. H., and Tripathi, A. (2000). How to extract the Newtonian viscosity from capillary breakup measurements in a filament rheometer. *Journal of Rheology* *44*, 653-670.
- Merkel, R., Nassoy, P., Leung, A., Ritchie, K., and Evans, E. (1999). Energy landscapes of receptor-ligand bonds explored with dynamic force spectroscopy. *Nature* *397*, 50-53.

- Meyer, C. J., Alenqhat, F. J., Rim, P., Fong, J. H., Fabry, B., and Ingber, D. E. (2000). Mechanical control of cyclic AMP signalling and gene transcription through integrins. *Nat Cell Biol* 2, 666-668.
- Münstedt, H. (1979). New Universal Extensional Rheometer for Polymer Melts. Measurements on a Polystyrene Sample 10.1122/1.549544. *Journal of Rheology* 23, 421-436.
- Nageswara, B. D., Kemple, M. D., and Prendergast, F. G. (1980). Proton nuclear magnetic resonance and fluorescence spectroscopic studies of segmental mobility in aequorin and a green fluorescent protein from *Aequorea forskalea*. *Biophys J* 32, 630-632.
- Nambiar, R., Gajraj, A., and Meiners, J. C. (2004). All-optical constant-force laser tweezers. *Biophys J* 87, 1972-1980.
- NanoScience (2006). AFM Probes and Supplies (NanoScience Instruments).
- Oberhauser, A. F., Hansma, P. K., Carrion-Vazquez, M., and Fernandez, J. M. (2001). Stepwise unfolding of titin under force-clamp atomic force microscopy. *Proc Natl Acad Sci U S A* 98, 468-472.
- Oberhauser, A. F., Marszalek, P. E., Erickson, H. P., and Fernandez, J. M. (1998). The molecular elasticity of the extracellular matrix protein tenascin. *Nature* 393, 181-185.
- Ormö, M., Cubitt, A. B., Kallio, K., Gross, L. A., Tsien, R. Y., and Remington, S. J. (1996). Crystal Structure of the *Aequorea victoria* Green Fluorescent Protein 10.1126/science.273.5280.1392. *Science* 273, 1392-1395.
- Orr, A. W., Helmke, B. P., Blackman, B. R., and Schwartz, M. A. (2006). Mechanisms of mechanotransduction. *Dev Cell* 10, 11-20.
- Paramore, S., Ayton, G. S., and Voth, G. A. (2005). Extending a Spectrin Repeat Unit II. Rupture Behavior 10.1529/biophysj.105.066977. *Biophys J*, biophysj.105.066977.
- Patterson, G. H., and Lippincott-Schwartz, J. (2002). A Photoactivatable GFP for Selective Photolabeling of Proteins and Cells 10.1126/science.1074952. *Science* 297, 1873-1877.
- Pawson, T. (2004). Specificity in signal transduction: from phosphotyrosine-SH2 domain interactions to complex cellular systems. *Cell* 116, 191-203.
- Pelham, R. J., Jr., and Wang, Y.-l. (1999). High Resolution Detection of Mechanical Forces Exerted by Locomoting Fibroblasts on the Substrate. *Mol Biol Cell* 10, 935-945.
- Poiseuille, J. L. M. (1840). (title n/a). *Compt rend* 11, 961.
- Rief, M., Gautel, M., Oesterhelt, F., Fernandez, J. M., and Gaub, H. E. (1997). Reversible unfolding of individual titin immunoglobulin domains by AFM. *Science* 276, 1109-1112.
- Rief, M., Pascual, J., Saraste, M., and Gaub, H. E. (1999). Single molecule force spectroscopy of spectrin repeats: low unfolding forces in helix bundles. *J Mol Biol* 286, 553-561.
- Rosenow, M. A., Huffman, H. A., Phail, M. E., and Wachter, R. M. (2004). The crystal structure of the Y66L variant of green fluorescent protein supports a cyclization-oxidation-dehydration mechanism for chromophore maturation. *Biochemistry* 43, 4464-4472.

- Rozzo, C., Chiesa, V., Caridi, G., Pagnan, G., and Ponzoni, M. (1997). Induction of apoptosis in human neuroblastoma cells by abrogation of integrin-mediated cell adhesion. *Int J Cancer* *70*, 688-698.
- Samori, B., Zuccheri, G., and Baschieri, R. (2005). Protein unfolding and refolding under force: methodologies for nanomechanics. *Chemphyschem* *6*, 29-34.
- Sawada, Y., and Sheetz, M. P. (2002). Force transduction by Triton cytoskeletons. *J Cell Biol* *156*, 609-615.
- Schlierf, M., Li, H., and Fernandez, J. M. (2004). The unfolding kinetics of ubiquitin captured with single-molecule force-clamp techniques. *Proc Natl Acad Sci U S A* *101*, 7299-7304.
- Schmidt, J. J., Jiang, X., and Montemagno, C. D. (2002). Force Tolerances of Hybrid Nanodevices. *Nano Lett* *2*, 1229-1233.
- Scott, C., Phillips, G. W., and Baines, A. J. (2001). Properties of the C-terminal domain of 4.1 proteins. *Eur J Biochem* *268*, 3709-3717.
- Scott, G., Cassidy, L., and Busacco, A. (1997). Fibronectin suppresses apoptosis in normal human melanocytes through an integrin-dependent mechanism. *J Invest Dermatol* *108*, 147-153.
- Sheehan, J., Cruickshank, P., and Boshart, G. (1961). Notes- A Convenient Synthesis of Water-Soluble Carbodiimides. *Journal of Organic Chemistry* *26*, 2525-2528.
- Sheehan, J., Preston, J., and Cruickshank, P. (1965). A Rapid Synthesis of Oligopeptide Derivatives without Isolation of Intermediates. *Journal of the American Chemical Society* *87*, 2492-2493.
- Silver, F. H., and Bradica, G. (2002). Mechanobiology of cartilage: how do internal and external stresses affect mechanochemical transduction and elastic energy storage? *Biomech Model Mechanobiol* *1*, 219-238.
- Silver, F. H., Siperko, L. M., and Seehra, G. P. (2003a). Mechanobiology of force transduction in dermal tissue. *Skin Research and Technology* *9*, 3-23.
- Silver, F. H., Siperko, L. M., and Seehra, G. P. (2003b). Mechanobiology of force transduction in dermal tissue
doi:10.1034/j.1600-0846.2003.00358.x. *Skin Research and Technology* *9*, 3-23.
- Sinicropi, A., Andruniow, T., Ferre, N., Basosi, R., and Olivucci, M. (2005). Properties of the Emitting State of the Green Fluorescent Protein Resolved at the CASPT2//CASSCF/CHARMM Level. *J Am Chem Soc* *127*, 11534-11535.
- Smith, R. E. (1984). Effect of Gap Errors in Rotational Concentric Cylinder Viscometers. *Journal of Rheology* *28*, 155-160.
- Staros, J. V., Wright, R. W., and Swingle, D. M. (1986). Enhancement by N-hydroxysulfosuccinimide of water-soluble carbodiimide-mediated coupling reactions. *Analytical Biochemistry* *156*, 220-222.
- Stockmayer, W. H. (1944). Theory of Molecular Size Distribution and Gel Formation in Branched Polymers II. General Cross Linking doi:10.1063/1.1723922. *The Journal of Chemical Physics* *12*, 125-131.
- Striker, G., Subramaniam, V., Seidel, C. A. M., and Volkmer, A. (1999). Photochromicity and Fluorescence Lifetimes of Green Fluorescent Protein. *Journal of Physical Chemistry B* *103*, 8612-8617.

- Sultan, C., Stamenović, D., and Ingber, D. E. (2004). A Computational Tensegrity Model Predicts Dynamic Rheological Behaviors in Living Cells. *Annals of Biomedical Engineering* 32, 520-530.
- Tamada, M., Sheetz, M. P., and Sawada, Y. (2004). Activation of a signaling cascade by cytoskeleton stretch. *Dev Cell* 7, 709-718.
- Tang, Y., Grey, M. J., McKnight, J., Palmer, A. G., 3rd, and Raleigh, D. P. (2006). Multistate folding of the villin headpiece domain. *J Mol Biol* 355, 1066-1077.
- Topell, S., Hennecke, J., and Glockshuber, R. (1999). Circularly permuted variants of the green fluorescent protein. *FEBS Lett* 457, 283-289.
- Tsien, R. Y. (1998). The green fluorescent protein. *Annu Rev Biochem* 67, 509-544.
- van Mameren, J., Modesti, M., Kanaar, R., Wyman, C., Wuite, G. J., and Peterman, E. J. (2006). Dissecting elastic heterogeneity along DNA molecules coated partly with Rad51 using concurrent fluorescence microscopy and optical tweezers. *Biophys J*.
- Vasiliu, C. (2001). Macromolecular mechanochemistry.
- Vogel, V. (2006). Mechanotransduction involving multimodular proteins: converting force into biochemical signals
doi:10.1146/annurev.biophys.35.040405.102013. *Annual Review of Biophysics and Biomolecular Structure* 35, 459-488.
- Wang, N., Butler, J. P., and Ingber, D. E. (1993). Mechanotransduction across the cell surface and through the cytoskeleton. *Science* 260, 1124-1127.
- Wang, N., Naruse, K., Stamenović, D., Fredberg, J. J., Mijailovich, S. M., Tolic-Norrelykke, I. M., Polte, T., Mannix, R., and Ingber, D. E. (2001a). Mechanical behavior in living cells consistent with the tensegrity model
10.1073/pnas.141199598. *PNAS* 98, 7765-7770.
- Wang, N., Naruse, K., Stamenović, D., Fredberg, J. J., Mijailovich, S. M., Tolic-Norrelykke, I. M., Polte, T., Mannix, R., and Ingber, D. E. (2001b). Mechanical behavior in living cells consistent with the tensegrity model. *Proc Natl Acad Sci U S A* 98, 7765-7770.
- Ward, W. W., and Bokman, S. H. (1982). Reversible denaturation of Aequorea green-fluorescent protein: physical separation and characterization of the renatured protein. *Biochemistry* 21, 4535-4540.
- Ward, W. W., Prentice, H. J., Roth, A. F., Cody, C. W., and Reeves, S. C. (1982). N/A. *Photochem Photobiol* 35, 803-805.
- Weber, W., Helms, V., McCammon, J. A., and Langhoff, P. W. (1999). Shedding light on the dark and weakly fluorescent states of green fluorescent proteins. *Proc Natl Acad Sci U S A* 96, 6177-6182.
- Wernig, F., and Xu, Q. (2002). Mechanical stress-induced apoptosis in the cardiovascular system. *Prog Biophys Mol Biol* 78, 105-137.
- West, D. K., Brockwell, D. J., Olmsted, P. D., Radford, S. E., and Paci, E. (2006). Mechanical resistance of proteins explained using simple molecular models. *Biophys J* 90, 287-297.
- Wiehler, J., Jung, G., Seebacher, C., Zumbusch, A., and Steipe, B. (2003). Mutagenic stabilization of the photocycle intermediate of green fluorescent protein (GFP). *Chembiochem* 4, 1164-1171.
- Williams, A., and Ibrahim, I. T. (1981). A new mechanism involving cyclic tautomers for the reaction with nucleophiles of the water-soluble peptide coupling reagent 1-